Universidad
Carlos III de Madrid

PhD Thesis

ON-CHIP MODE-LOCKED MICROWAVE PHOTONIC INTEGRATED CIRCUITS

Author: Carlos Diego Gordón Gallegos

Director: Dr. Guillermo Carpintero del Barrio

DEPARTMENT OF ELECTRONIC TECHNOLOGY

Leganés, September 2016

Universidad Carlos III de Madrid

TESIS DOCTORAL

ON-CHIP MODE-LOCKED MICROWAVE PHOTONIC INTEGRATED CIRCUITS

Autor: D. Carlos Diego Gordón Gallegos

Director: Dr. Guillermo Carpintero del Barrio

DEPARTAMENTO DE TECNOLOGÍA ELECTRÓNICA

Leganés, Septiembre de 2016

TESIS DOCTORAL

ON-CHIP MODE-LOCKED MICROWAVE PHOTONIC INTEGRATED CIRCUITS

Autor: Carlos Diego Gordón Gallegos

Director: Prof. Dr. D Guillermo Carpintero del Barrio

Firma Del Tribunal Calificador

Presidente: _____

Vocal: _____

Secretario: _____

Calificación:

_____

En Leganés, a ____ de _____ 2016

Dedicatoria

Cuatro años han sido requeridos para llevar a cabo el presente trabajo, y el gran esfuerzo de dejar muy lejos a mis seres queridos para conseguir los sueños planteados.

A mi Amada Esposa Myriam, por su incondicional apoyo en las buenas y en las malas, a mi futuro hijito, la bendición que Dios ha dado a mi familia.

A mis Padres Víctor y Carmen por haberme dado la vida y la oportunidad de disfrutarla.

A mi extraordinario tutor, PhD. Guillermo Carpintero del Barrio por sus enseñanzas, calidad humana y sobre todo su paciencia.

A todos los compañeros del grupo de investigación, que en orden alfabético les nombro, Corral Vinicio, Guzmán Robinson, Lo Mu Chieh y Orbe Luis, por el tiempo compartido durante el desarrollo del trabajo.

Preface

"Imagination is more important than knowledge".

Albert Einstein, (1879-1955)

Mention of "International Doctor"

Academic Visit for the "International Doctor" Distinction in COBRA Research Institute, Eindhoven University of Technology, Den Dolech2, 5612AZ Eindhoven, The Netherlands

Abstract

The generation of increasingly higher frequencies, reaching the Millimeter (MMW, 30 to 300 GHz) and Terahertz-wave (THz, 300 to 3000 GHz) range is one way to address the increasing need for bandwidth in wireless communications using simple modulation techniques. Recent experimental results have reported data rates up to 48 Gbps on a 300 GHz carrier frequency demonstrating that a cost effective solution to cope with the required bandwidths in wireless communications is to increase the carrier wave frequency into the millimeter wave region and beyond. The difficulties to generate, amplify and modulate signals at these frequencies have been overcome by combining the best of two worlds, electronics and photonics, arising a new field commonly referred nowadays as microwave photonics. A microwave photonic system usually involves an optical frequency synthesizer (OFS) and an opto-electronic converter (OEC). The OFS is specifically designed to deliver an optical signal that when is converted to the electrical domain by the OEC generates a high frequency electrical signal.

Currently, most if not all of the reported wireless communication links operating above 100 GHz employ photonic generation of the carrier frequency. Generally, there are two main photonic signal generation techniques commonly used, pulsed sources and heterodyning sources. One of the merits of pulsed sources over heterodyning ones is that for the same optical power achieves a higher electrical emitted power (about 7 dBm above). Thus, pulsed sources are an attractive option to be implemented as a carrier generator with the novel approach of photonic integration.

In the frame of this work, we have developed a new kind of photonic sources based on the pulsed signal generation technique, which can be fabricated within a generic foundry in a photonic integrated circuit. Our solutions are on-chip mode-locked laser structures, designed using generic building blocks from an indium-phosphide photonic integration technology platform. We have designed and characterized novel on-chip mode-locked laser structures using multimode interference reflectors, which enable us to locate the devices anywhere on the chip, making the optical signal available to the rest of the components on the chip, and allowing subsequent photonic signal processing operations within the chip (modulation, optical filtering, repetition rate multiplication and so on). We have reported an on-chip colliding pulse mode-locked laser working at 70 GHz repetition rate and a novel on-chip multiple colliding pulse mode-locked laser operating at 100 GHz repetition rate.

As an added value, the performance characteristics of the novel on-chip mode-locked laser structures allow them to be used as a pulsed source in E-band and F-Band wireless link demonstrations. The on-chip colliding pulse mode-locked laser working at 70 GHz repetition rate has been used to demonstrate E-band wireless link while the on-chip multiple colliding pulse mode-locked laser operating at 100 GHz repetition rate was used to demonstrate the F-Band wireless link.

Resumen

La generación de frecuencias cada vez más elevadas, llegando al rango de ondas Milimétricas (mmW, de 30 a 300 GHz) y ondas de Terahertz (THz, 300-3000 GHz) es una forma de hacer frente a la creciente necesidad de ancho de banda en las comunicaciones inalámbricas que utilizan técnicas de modulación simples. Los resultados experimentales recientes han informado tasas de datos de hasta 48 Gbps en una frecuencia portadora de 300 GHz que demuestra que una solución rentable para hacer frente a los anchos de banda requeridos en las comunicaciones inalámbricas es aumentar la frecuencia de la onda portadora en la región de ondas milimétricas y más allá. Las dificultades para generar, amplificar y modular las señales en estas frecuencias se han superado mediante la combinación de lo mejor de dos mundos, electrónica y fotónica, resultando en un nuevo campo comúnmente referido hoy en día como fotónica de microondas. Un sistema de fotónica de microondas usualmente incluye un sintetizador de frecuencia óptica (OFS) y un convertidor opto-electrónico (OEC). El OFS es especialmente diseñado para entregar una señal óptica que cuando es convertida al dominio eléctrico por el OEC genera una señal eléctrica de alta frecuencia.

Actualmente, la mayoría si no son todos los reportes de enlaces de comunicación inalámbrica que operan por encima de 100 GHz emplean generación fotónica de la frecuencia portadora. Generalmente, hay dos principales técnicas de generación de señal fotónica comúnmente usadas, fuentes pulsadas y fuentes heterodinas. Uno de los méritos de las fuentes pulsadas sobre las heterodinas es que para la misma potencia óptica se alcanza mayor potencia eléctrica emitida (aproximadamente 7 dBm por encima). Por lo tanto, las fuentes pulsadas son una opción atractiva para ser

implementada como un generador de portadora con el nuevo enfoque de la integración fotónica.

En el marco de este trabajo, hemos desarrollado un nuevo tipo de fuentes fotónicas basadas en la técnica de generación de señal pulsada, la cual puede ser fabricada mediante una fundición genérica en un circuito integrado fotónico. Nuestras soluciones son estructuras de láser mode-locked integradas en chip, diseñadas usando bloques de construcción genéricos de una plataforma de tecnología de integración fotónica en indio-fósforo. Nosotros hemos diseñado y caracterizado nuevas estructuras de láser mode-locked integradas en chip usando reflectores de interferencia multimodo, los cuales nos permiten ubicar los dispositivos en cualquier lugar dentro del chip, haciendo la señal óptica disponible para el resto de componentes en el chip, y permitiendo las subsecuentes operaciones de procesamiento de señal fotónica dentro del chip (modulación, filtrado óptico, multiplicación de la tasa de repetición, etc.). Nosotros hemos publicado un láser "colliding pulse mode-locked" integrado en chip trabajando a una tasa de repetición de 70 GHz y un nuevo láser "multiple colliding pulse mode-locked" integrado en chip operando a una tasa de repetición de 100 GHz.

Como valor añadido, las características de rendimiento de las nuevas estructuras de láser mode-locked integradas en chip permiten ser utilizadas como una fuente pulsada en enlaces inalámbricos en banda-E y banda-F. La estructura de láser "colliding pulse mode-locked" integrada en chip trabajando a una taza de repetición de 70 GHz se ha utilizado para demostrar el enlace inalámbrico en banda-E, mientras que la estructura de láser "multiple colliding pulse mode-locked" integrada en chip funcionando a una frecuencia de 100 GHz fue usada para demostrar el enlace inalámbrico en banda-F.

Acronyms

A.U	Arbitrary Units.
AC	Autocorrelator.
ACPM	Asymmetric Colliding Pulse Mode-Locking.
AN	Amplitude Noise.
APE	Applied Physics and Electronics.
AR	Anti-reflection.
AWG	Arrayed Waveguide Grating.
AWGL	Arrayed Waveguide Grating based Laser
BER	Bit Error Rate.
BERT	Bit Error Rate Tester.
bps	Bits per second.
BPSK	Binary Phase Shift Keying.
CPM	Colliding Pulse Mode-Locked Laser.
CS	Cavity Structure.
CW	Continuous Wave.
D2S	Deep2Shallow.
dBc	Decibels relative to the carrier.
dBi	Decibels relative to isotropic.
dBm	Decibel relative to a milliwatt.
DBR	Distributed Bragg Reflector.
DCF	Dispersion Compensating Fiber.
EDFA	Erbium Doped Fiber Amplifier.
EOAM	Electro Optical Amplitude Modulator.
ERM	Electro-Refractive Phase Modulators
ESA	Electrical Spectrum Analyzer.

FF	Fundamental Frequency.
FP	Fabry-Perot.
FWHM	Full-Width at Half-Maximum.
Gbps	Gigabits per second.
GHz	Gigahertz.
GTIP	Generic Technologies for Integrated Photonics.
HF	High Frequency.
HML	Harmonic Mode-Locked.
IL-OPM	In-Line Optical Power Meter.
InGaAsP/InP	Indium Gallium Arsenide Phosphide / Indium Phosphide.
IR	Infrared.
ISO	Isolator.
ITU	International Telecommunication Union.
Kbps	Kilobit per second.
LA	Limiting Amplifier.
L_{cav}	Cavity Length.
LF	Lensed Fiber.
LNA	Low-Noise Amplifier.
LPF	Low-Pass Filter.
MCB	Multiple Colliding Bias.
mCPM	Multiple Colliding Pulse Mode-Locked Laser Diode.
MIR	Multimode Interference Reflector.
ML	Mode-Locking.
MLLD	Mode-Locked Laser Diodes.
MMI	Multimode Interference.
MMIC	Monolithic Microwave Integrated Circuit.
mmW	Millimeter Wave.
MPW	Multi-Project Wafer.

MWP	Microwave Photonics.
MXR	Mixer.
MZM	Mach-Zehnder Modulator.
NIR	Near-Infrared.
NTT	Nippon Telegraph and Telephone Corporation.
OC	Optical Carrier.
oc-CPM	On-chip Colliding Pulse Mode-Locked Laser Diode.
oc-FP	On-chip Fabry–Perot Laser Diode.
oc-mCPM	On-chip Multiple Colliding Pulse Mode-Locked Laser Diode.
oc-sCPM	On-chip Self-Colliding Pulse Mode-Locked Laser Diode.
OEC	Opto-Electronic Converter.
OFCG	Optical Frequency Comb Generator.
OFS	Optical Frequency Synthesizer.
OI	Optical Isolator.
OMD	Optical Modulator Driver.
OOK	On-Off Keying.
OTDM	Optical Time Domain Multiplexing.
PC	Polarization Controller.
PD	Photodiode.
PICs	Photonic Integrated Circuits.
PIN-PD	PIN photodiode.
PM	Power Meter.
PN	Phase Noise.
PPG	Pulse Pattern Generator.
PRBS	Pseudorandom Bit Sequence.
PW	Passive Waveguide.
QAM	Quadrature Amplitude Modulation.
QPSK	Quadrature Phase Shift Keying.

QW	Quantum Well.
QWI	Quantum Well Intermixing.
RBW	Resolution Bandwidth.
RF	Radio Frequency.
S2D	Shallow2Deep.
SA	Saturable Absorber.
SBD	Schottky Barrier Diode.
sCPM	Self-Colliding Pulse Mode-Locked Laser Diode.
SHG	Second Harmonic Generation.
SLR	Sagnac Loop Reflector.
SMSR	Side Mode Suppression Ratio.
SNR	Signal to Noise Ratio.
SOA	Semiconductor Optical Amplifier.
SPM	Self-Phase Modulation.
SSB	Single Side-Band.
STM	Standard Transmission Module.
TBP	Time Bandwidth Product.
TEC	Thermoelectric cooler.
THz	Terahertz.
TL	Type of Laser.
TWM	Travelling Wave Model.
UTC-PD	Uni-Travelling Carrier Photodiode.
VBW	Video Bandwidth.
VOA	Variable Optical Attenuator.
WDM	Wavelength Division Multiplexing.

Index

Chapter 1

Photonic Enabled Millimeter and Terahertz Wave Signal Generation

1.1 Introduction

In recent decades, data rates in both wired and wireless communications systems have been increasing exponentially. Based on current trends, multi-gigabit-per-second wireless communications will be needed in order to cope with future needs [1]. Figure 1.1 shows the expected growth of the data rates in wired (fiber optic) and wireless communication links. Extrapolating the current data rate growth trend, it is expected that wireless data will represent a significant proportion of total backbone traffic and that much faster wireless transmission rates will be required to support more sophisticated, bandwidth-intensive applications [2]. An important aspect to be highlighted from Figure 1.1 is the gap that exists between the data rates among wired and wireless communication systems. Wired technology (which includes fiber optic and coaxial cables) have already achieved a 100 Gbps data rate in 2010, whilst wireless technology follows this trend with a slight delay, having achieved a maximum data rate of 100 Gbps using 16-QAM modulation format in 2013 [3]. It is expected that by 2020, the wireless data rates will reach more than the wired speed.

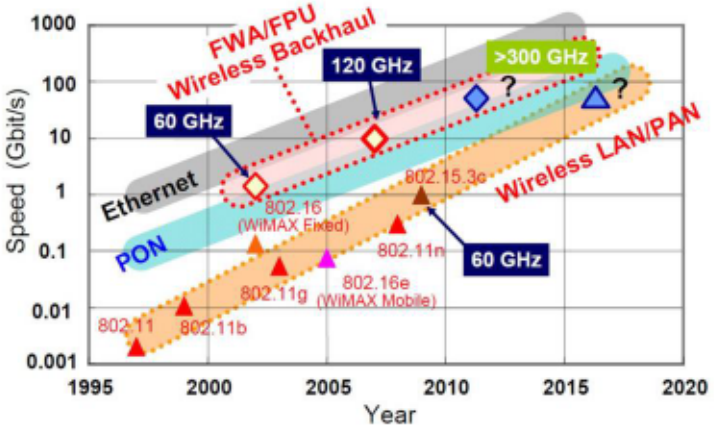

Figure 1.1. Data rate have been increasing exponentially in recent decades [4].

The growth rate shown in Figure 1.1 has been coined as Edholm's law, describing that the demand for bandwidth in wireless short-range communications has doubled every 18 months over the last 25 years [5].Within the current frequency bands allocated for wireless communications, at 2.4 and 5 GHz, the available bandwidths are 40 and 160 MHz, respectively, with data rates up to 600 Mbps which are too narrow for broadband services. It is therefore necessary to consider a suitable solution to overcome the data rate limitation [6]. This has been termed as the bandwidth problem. In a recent interview Martin Cooper (father of the cellular phone), stated that the bandwidth problem will only be solved through the creation of more bandwidth, in new spectrum allocations, suitable for supporting high data rates [7]. To date, different approaches have been considered to increase the data rates of wireless data links, the most promising ones being [6]:

a) **Higher order modulation formats** (Increase the complexity of the modulation formats).
b) **Use free-space optical communications**.
c) **Increase the frequency of carrier waves to the millimeter and terahertz wave range**.

Higher order modulation formats have been shown to require very high spectral efficiency modulation formats to enable 100 Gbps wireless data rates using electronic or/and photonic technology. The 8.6 GHz bandwidth available in the unlicensed (60 GHz) [8] and 10 GHz in the "lite license" (E-band, 71-76 and 81-86 GHz) [9] have shown that these spectrum allocations are enough to transmit multi gigabit of data using 64-QAM [10] or higher order modulation formats. But, there are several drawbacks to this approach. Not only, have the limitation of maximum transmitter output power up to

10 dBm [11]. But also, the necessity of modulation/demodulation systems which increase the cost, the power consumption and introduce processing delays [12].

Free-space optical communications is an alternative approach, using the atmospheric windows at the visible and near-infrared (NIR) regions of the spectrum, offering a competitive solution for point-to-point wireless links. Recent reports have demonstrated 100Gbps speeds [13], employing higher order modulation formats such as quadrature phase shift keying (QPSK), quadrature amplitude modulation (QAM) and polarization multiplexing systems. The main drawbacks of this technology are that some atmospheric conditions, like fog and rain, severely affect the availability of the link [5].

A very competitive approach is to increase the carrier wave frequency into the millimeter and terahertz wave range, where large frequency bands are still unregulated, offering the required bandwidth for broadband communications. As shown in Figure 1.2, these frequencies lie in a region of the electromagnetic radiation spectrum between photonics on the one hand (infrared range) and electronics (millimeter wave range) on the other, having coined the term "THz Gap" for this region.

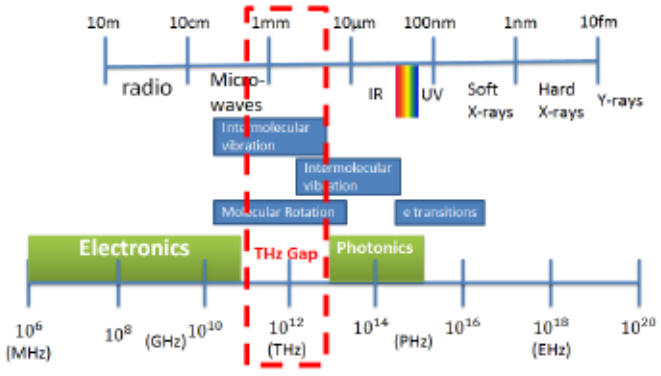

Figure 1.2. The THz Gap in the Spectrum of the Electromagnetic Radiation

The special characteristics of this range, where resonance frequencies of different compounds are located, makes it suitable for a wide range of applications beyond broadband communications [14], metrology [15], bioscience, spectroscopy [16], remote sensing [17] and imaging for security applications [18]. One of the main drawbacks of this approach is that it is hard to make terahertz sources that deliver sufficient power, required as the Terahertz waves in atmosphere experience high losses. This challenge can be addressed through the source as well as through the development of compact receiver modules with a high responsivity and broad bandwidth.

Figure 1.3 represents the propagation losses over the millimeter and terahertz wave frequency range, including the atmospheric attenuation for different weather conditions [19], [20], [21], attenuation peaks due to oxygen and water vapor absorption peaks, which define transmission windows on which future wireless links could be operated Currently, wireless communication research concentrates at millimeter-waves in the unlicensed 60 GHz band between 57-64 GHz and the W-band between 75-110 GHz.

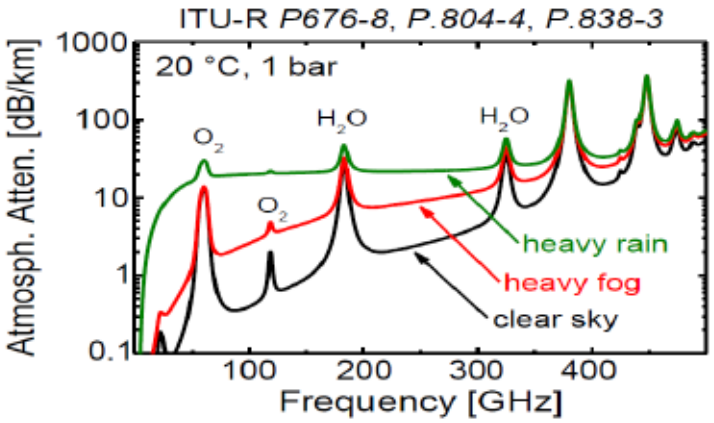

Figure 1.3. Propagation losses over the millimeter and terahertz wave frequency range, including the atmospheric attenuation in the range 0-500 GHz under different weather conditions according to ITU standards [19], [20], [21], attenuation peaks due to oxygen and water vapor absorption peaks.

Above these frequency bands, the spectrum from 275 GHz up to 300 GHz remains unregulated, with several GHz of available bandwidth. This range is very attractive for data rate up to 100 Gbps and beyond. A wide spectrum band allows using simple modulation formats, such as on-off keying (OOK), which avoid coding delays [22]. However, as the free-space path loss is governed by the Friis' equation[1], wireless links at carrier wave frequencies above 100 GHz require high gain antennas that turn the links into highly directional, line-of-sight, point-to-point links. The main problem to use these frequency bands is the lack of suitable signal sources. Two different approaches are commonly used to access the millimeter and terahertz wave ranges.

The first approach is based on electronic up-conversion. This approach adds frequency multipliers to a continuous wave (CW) signal generator to increase the generated signal frequency. It uses the highly integrated monolithic microwave integrated circuit (MMIC) technology. There have been several demonstrations of broadband wireless links, being NTT Microsystem Integration Laboratories the first to report a successful field trial of a wireless link operating at 120 GHz, showing a 10 Gbps data rate using electronic based technology [23]. Similarly, other demonstration at 220 GHz has been reported [24].

The second approach is based on photonic technology. The photonics-based transmitter has proven to be effective to achieve higher data rates of up to 1 Gbps and above. This could be realized thanks to the availability of telecom-based high-frequency components such as lasers, modulators and photodiodes (PDs). The use of optical fiber enables us to carry high-frequency RF signals over long distances making as well the

[1] Friis' equation, derived in 1945 by Bell Labs worker Harald T. Friss. It states that the loss increases with the square of the carrier frequency and the square of the link distance.

size of the transmitter frontends compact and light. There have been several demonstrations reported at 120 GHz with data rate up to 3 Gbps [25]. Recently, 100 Gbps data rate on a wireless sub-THz communication system using photonic generation of the carrier wave at 237.5 GHz has been reported [3].

In the frame of this work, we present a novel approach to implement an integrated photonic signal generator and its application in high capacity wireless link operating in the millimeter-wave range. Photonic integrated solutions allow reducing the size, also reduce the cost (when multi-project wafer runs are used), and increase the functionality on the chip.

There are several photonic techniques used for the generation of signals with frequencies in the mmW and THz wave range. The following section will introduce the techniques suitable for photonic integration.

1.2 Photonic Techniques for mmW and THz Wave Signal Generation

As we have already highlighted, increasing the carrier wave frequency into the millimeter and terahertz wave region is a cost effective solution to obtain broadband wireless links [26]. The difficulty to generate, amplify and modulate signals within these frequency ranges has been addressed combining electronics and photonics, emerging the field of microwave photonics (MWP). This field is a crossroad between photonics and radio-frequency (RF) engineering that combines the best of both worlds to enable key functionalities that are either too complex or not available on the RF domain alone [27].

It is commonly accepted that photonic techniques will play special relevance for frequencies starting about 100 GHz, and into the terahertz range, up to 10 THz. Photonic technologies have pioneered the access to this range, providing unique advantages in terms of quality of the generated signal (low phase noise, wide frequency tuning range) and modulation bandwidth [22], [28], [29]. To date, several wireless communication links that have been reported operating above 100 GHz use different photonic generation techniques for the carrier wave signal [30].

As shown in Figure 1.4, a photonic signal generation system is usually composed of two main building blocks, which are an optical frequency synthesizer (OFS) and an opto-electronic converter (OEC). The OFS is responsible for the generation of a photonic signal, that when directed onto the OEC, converts the optical signal into an electrical signal with the desired frequency.

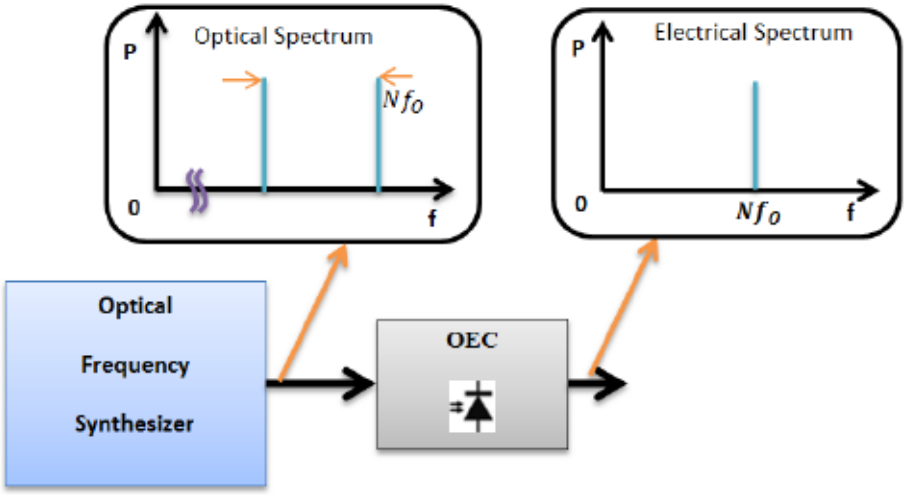

Figure 1.4. Photonic Signals Synthesis Technique

For the optical frequency synthesizer, there are two main photonic signal generation techniques, optical heterodyne and pulsed technique [30]. Figure 1.5 depicts the main photonic signal generation techniques.

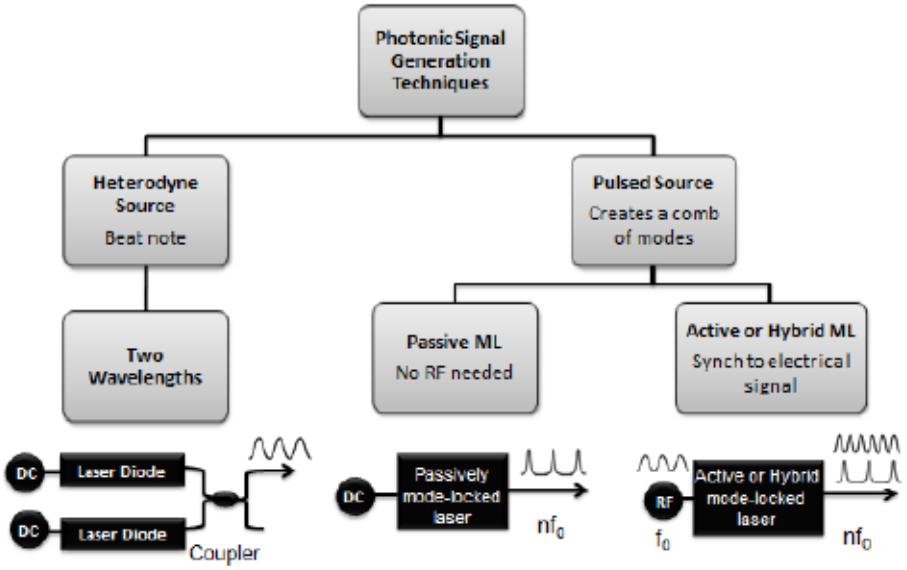

Figure 1.5. Photonic signal generation techniques.

1.2.1 Heterodyne Source Technique

Optical heterodyning is a signal generation technique using a dual wavelength source. It basically consists on applying to a photodiode an optical signal that results from combining two optical frequencies f_1 and f_2. On the photodiode, two new signals are generated with frequency being determined from the sum ($f_1 + f_2$) and the difference ($f_1 - f_2$) of the optical frequencies. Typically, the bandwidth limit of the photodetector allows observing only the difference frequency, also known as beat frequency.

There are different arrangements to implement an optical heterodyne source. An optical heterodyne signal is usually achieved combining the output of two free running continuous wave (CW) laser diodes through a 50/50 optical coupler as shown in Figure 1.6. An electrical beat note signal or radio-frequency signal is then generated at the output of the photo detector with a frequency corresponding to the wavelength spacing

of the two optical waves. This approach provides an excellent frequency tuning range, from a few tenths of MHz to 10 THz [31]. The main problem is that due to the fact that both lasing modes are not correlated, its frequency stability is generally poor. Phase noise of –75 dBc / Hz at an offset frequency of 100 MHz, and the frequency drift more than 10 MHz/hour have been reported [32].

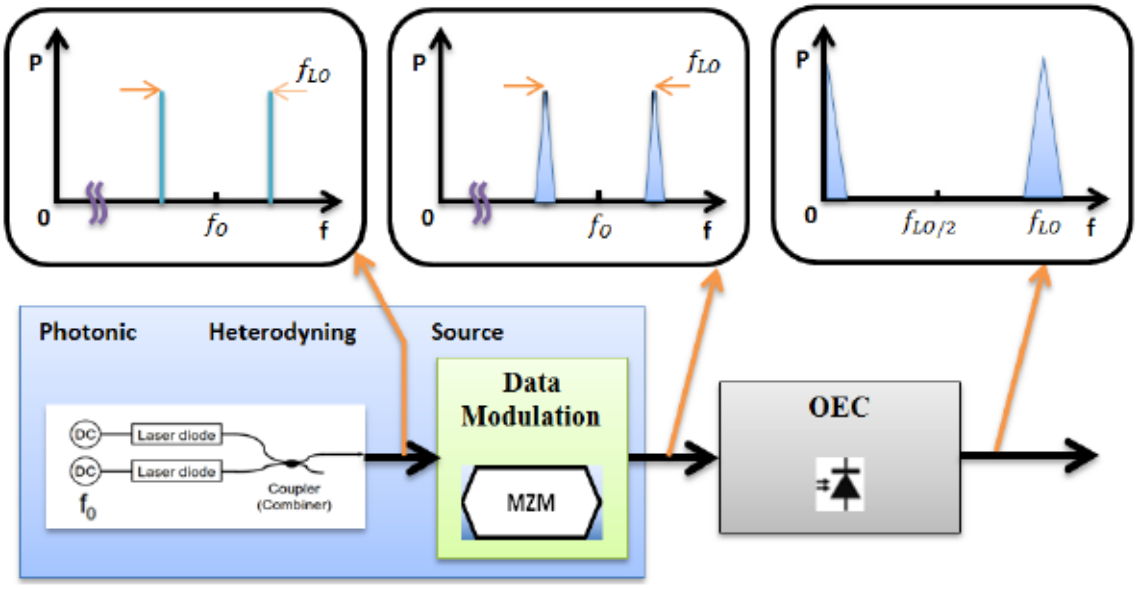

Figure 1.6. Heterodyne Source Technique using two Laser Diodes

Another method is the external modulation, in which a single CW optical source is followed by an external modulator, as shown in Figure 1.7. The modulation generates optical sidebands, which are phase locked, and allow transmitting this high frequency signal over the fiber. On one hand, we require an electronic source to generate the signal and a wide frequency bandwidth modulator. The current state of the art limits the maximum bandwidth to approximately 110 GHz [33]. On the other hand, it has excellent phase noise or stability of the generated signal as it depends on the RF synthesizer. Figure 1.7 shows the experimental arrangement of a CW laser and an external modulator.

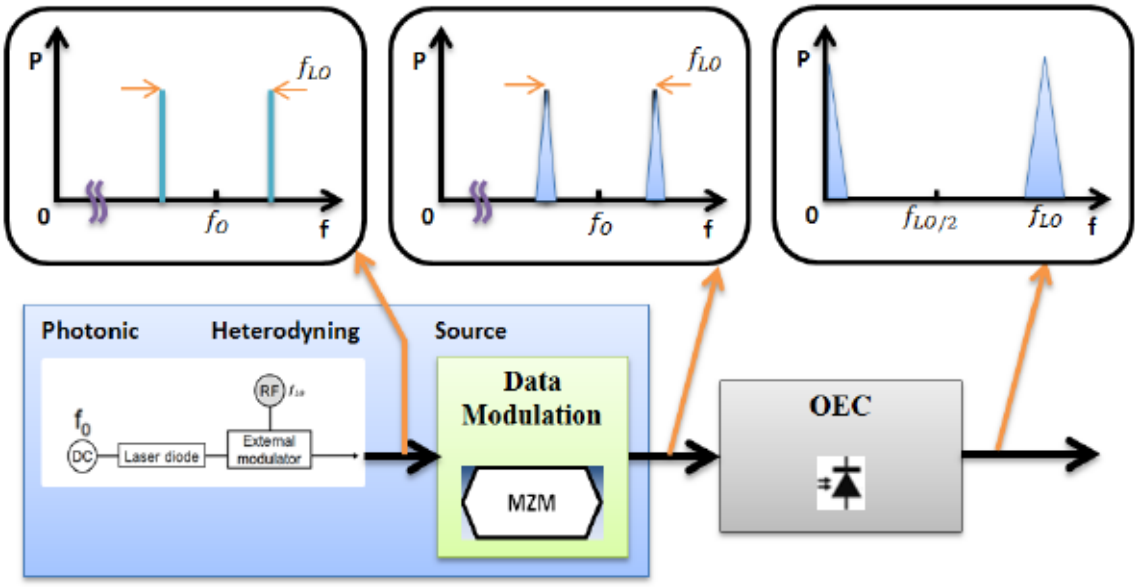

Figure 1.7. Heterodyne Source Technique using CW laser and an external modulator

The last method of optical heterodyne is an optical frequency comb generator (OFCG), which is one of the most sophisticated photonic signal generation schemes that satisfy all the requirements of bandwidth and tunability greater than 2 THz [34], power output is high determined by the laser diode and the stability or phase noise determined by electronics. Recent results have demonstrated that it is possible to integrate a comb source with > 2 THz bandwidth and < 10 Hz frequency error between comb lines using a ring hybrid mode-locked laser with an intracavity gain flattering filter [34]. For signal generation, the OFCG is followed by an optical filter block, which selects two wavelengths from the OFCG spaced by the frequency desired for the synthesized signal. It is necessary the use of an OEC, or photo mixer at the end to complete the total signal generation. Figure 1.8 sketches the structure for signal generation, the OFCG, the optical filter and the OEC in the block diagram.

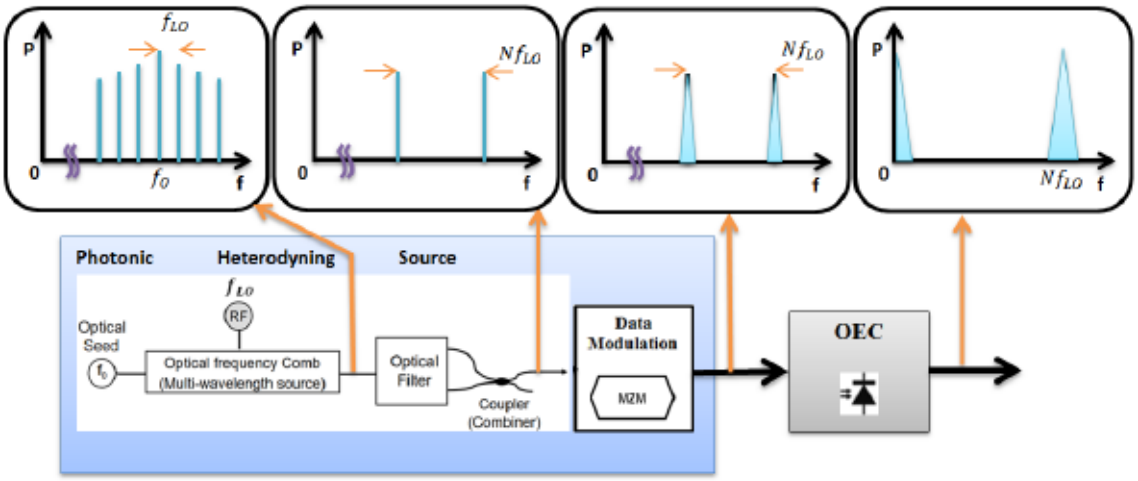

Figure 1.8. Heterodyne Source Technique using an optical frequency comb.

1.2.2 Pulsed Source Technique

A schematic diagram of a system using a pulsed signal generation technique is shown in Figure 1.9. The optical signal is a train of short optical pulses, equally spaced in time by the pulse repetition period and its inverse is the repetition rate frequency (Δf_{rep}). The optical spectrum of such a source are optical modes around the fundamental optical frequency (f_0), spaced by the repetition rate frequency (Δf_{rep}). A high speed optical modulator is then used to introduce the data signal, which can be noticed as an increase in the linewidth of the optical modes. When directed onto the OEC, an electrical signal is generated with its frequency given by the repetition rate of the pulses.

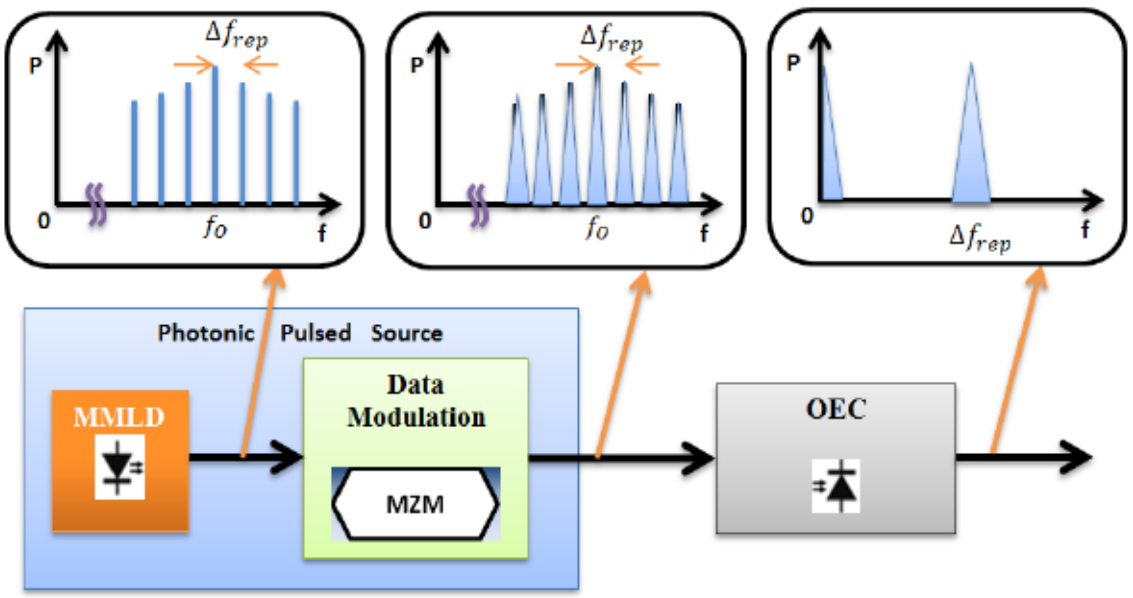

Figure 1.9. Pulsed Source Technique.

A common approach to implement a pulsed source technique is using Mode Locked Laser Diodes (MLLD), either in active, passive or hybrid regimes [30]. The repetition rate frequency (Δf_{rep}) is determined by the resonator cavity length, and usually has a reduced tunability, typically from 100 MHz to 1 GHz [35], [36].The phase noise of passively mode-locked lasers based on Fabry-Perot lasers is relatively high more than –70dBc/Hz at an offset frequency of 100 Hz [35]. The case of active mode locking, in which the laser is driven with an electronic oscillator, the phase noise is much lower (<–75dBc/Hz at an offset frequency of 100 Hz) [36], presenting an excellent stability.

1.2.3 Key Parameters of Photonic Signal Generation Techniques

Signal generation using photonic techniques have several advantages over electronic techniques in bandwidth, tunability and stability or phase noise, all of which are key parameters that are used to characterize a signal source. The ***bandwidth*** is related to the amount of information that can be transferred through a communication channel. A

band of a given width can carry the same amount of information regardless of where that band is located in the frequency spectrum. Therefore, bandwidth is the frequency range occupied by a modulated carrier wave. The ***tunability*** refers to the ability of the source to change the frequency of the generating signal controlled by some external command. The ***tuning range*** is then the range of frequencies within which is possible to adjust the frequency of the signal. Finally, the frequency generated by a signal source is not perfectly stable, but rather exhibits fluctuations due to noise, which leads to a finite linewidth of the signal. This noise is characterized by the ***phase noise*** (or Stability).

Each photonic generation technique has its own performance in terms of the aforementioned parameters. Table 1.1 shows a comparative among different photonic-based signal generation techniques. For optical heterodyne, we consider a) two laser diodes [31], [32], b) continuous-wave (CW) laser and an external modulator [33], and c) Optical Frequency Comb Generator (OFCG) [34]. Then, pulsed sources are represented by mode-locked laser diodes (MLLD) [31], [36].

Photonic Signal Synthesis Techniques	Method	Bandwidth	Tunability	Stability / Phase Noise
Heterodyne Sources	a) Heterodyning two LDs (with a short lasing cavity)	Excellent 0,1 to 10 THz	Excellent from 0,1 to 10 THz	Poor, bad Frequency drift large linewidth
	b) CW LD + external modulator	Good around 100 GHz	Good approximately 110 GHz	Excellent determined by electronics
	c) Optical comb (OFCG) + filter	Excellent > 2 THz	Excellent > 2 THz	Excellent determined by electronics
Pulsed Sources	d) Mode-Locked Laser Diode (passive/active)	Good Passive > 1 THz Active > 200 GHz	Bad from 0,1 to 1 GHz	Excellent for active Acceptable for passive

Table 1.1. Comparison among Photonic Signal Generation Techniques [37]

The common approach to implement these photonic signal generation schemes is to assemble such topologies using the required optical components such as laser, modulators, and combine them using optical fibres. However, the optical fibre

connections that are required introduce many problems, including path length variations due to thermal variations.

A novel approach, that is becoming readily available nowadays, is to use photonic integration circuits (PICs). Photonic integration allows placing all of the required optical components within a single chip. This has several advantages, starting from eliminating fibre coupling losses among the different components. Besides, a reduced size of the components gives a result a cost-effective solution. Therefore, pulsed sources are candidates to be implemented as a photonic integrated circuit in order to be used as a photonic source.

In summary, pulsed sources have the capability of generating an optical output power greater than the heterodyning sources [38]. It is because of many lasing modes are generated within the laser cavity. Also, pulsed sources have a wide range of applications. These kinds of sources have been successfully applied in optical communications [39], [40] and millimeter wave generation [41], [42] . Thus, pulsed sources are attractive option to be implemented with the novel approach of photonic integration.

In the frame of this work we have designed and characterized novel on-chip mode-locked laser structures which enable signal processing on chip. We have demonstrated that pulsed sources can be made in indium-phosphide-based photonic generic technologies using building blocks. As added value, the performance of the novel on-chip mode-locked laser structures allow them to be used as a pulsed source in E-band and F-Band wireless link demonstrations.

1.3 Outline

The present work describes the design and characterization of on-chip mode-locked laser structures capable to generate millimeter-wave signal for high data rate wireless communication systems using the pulsed source technique. In the frame of this work, the main objective is to develop novel on-chip mode-locked structures which have been characterized in terms of repetition rate (Δf_{rep}), pulse width ($\Delta\tau$) , time bandwidth product (TBP), linewidth (Δv_{RF}), timing jitter (σ_T), and amplitude jitter (N_{AM}).

Chapter 2 describes the fundamentals of mode-locked lasers where the principle of mode-locked regime and the structure of mode locked laser are presented. The different mode-locked techniques are introduced in order to identify the passive technique developed in the present work. Also, the mode-locked characterization methods used in the frame of this work are described. Taking advantage of previous reports, we have been able to obtain the state of the art mode-locked lasers.

Chapter 3 discusses the approaches that have been proposed to integrate mode-locked laser diodes on-chip due to the fact that the indium phosphide photonic integrated circuits have as key advantage enabling the integration of multiple photonic building blocks within a single chip to develop compact systems with increased functionality and performance. Among the on-chip integration approaches we have ring structures, Distributed Bragg Reflectors, Sagnac loop reflectors, and the novel multi-mode interference reflectors. Also, we describe the first samples developed using multi-mode interference reflectors.

Chapter 4 describes the work that we have developed in the design of on-chip colliding pulse mode locked laser diode (oc-CPM). The work was carried out through the study of the saturable absorber length, trying to optimize it with respect to the length of the gain section. The simulation results were obtained from the FreeTWM which is free software designed for the study of the dynamics of multi-section semiconductor lasers based on the traveling wave approach of Maxwell Bloch equations. The experimental results were acquired from four oc-CPMs with extended cavity linear laser configuration. The fundamental repetition was 25 GHz, which the colliding regime turns into 50 GHz. In order to enhance the structure, we carried out a comparison between simulation and experimental results which reveals the agreement between them.

Chapter 5 introduces the work that we presented for the first time, to the best of our knowledge which is a novel on-chip colliding pulse mode locked laser diode (oc-CPM) for millimeter wave Generation. The advantage of the resonator structure that we present is that the end-mirrors are defined through multimode interference reflectors (MIRs), which provide precise control of the cavity length avoiding the need for cleaved facets. This simplifies positioning the saturable absorber at the center of the resonator to achieve the colliding pulse mode-locked regime and double the repetition rate, reaching the millimeter wave frequency range. An additional advantage is that the pulsed output is delivered within the Photonic Integrated Circuit chip for further processing (i.e. modulation).

Chapter 6 presents the enhancement of the repetition rate frequency with a novel on-chip multiple colliding pulse mode-locked (oc-mCPM) semiconductor laser source. The device structure is fully integrated, replacing cleaved facet mirrors by using multimode

interference reflectors (MIRs), this allows to precise control the location of the saturable absorbers within the cavity length, which is critical to achieve the multiple colliding regime. We succeeded to achieve this regime generating a repetition rate at four times the fundamental round-trip frequency, demonstrating a repetition rate within the millimeter wave frequency range, at 100 GHz using a 25 GHz resonator cavity length. We also demonstrate the advantage of having the signal on-chip including a boost semiconductor optical amplifier in order to increase the output optical power.

Chapter 7 discusses two high data rate wireless link communication system demonstrations. We present an E-band and F-band wireless links based on two aforementioned photonic-based millimeter-wave signal sources which are the on-chip colliding pulse passive mode-locked and the on-chip multiple colliding pulse passive mode-locked laser diode structures, respectively. We were able to carry out high data rate wireless links which does not require any stabilization scheme due to the on-chip mode-locked structures working at passive technique does not require high frequency electronics for its operation. Also, the bit error rate (BER) measurement was performed in order to measure the quality of the wireless link.

Finally, Chapter 8 reports the conclusions of the present Thesis and suggests the future working lines.

This research was supported by the Spanish Ministerio de Economia y Competitividad DiDACTIC project (TEC2013-47753-C3-3-R) [43] and Consejería de Educación, Juventud y Deporte of Comunidad de Madrid DIFRAGEOS project (P2013/ICE-3004) [44]. Also, we acknowledge cooperation with foundry partners: SMART Photonics [45] and COBRA [46]; software partners: PhoeniX Software [47], FreeTWM [48]. The author, Carlos Diego Gordón Gallegos from the Technical

University of Ambato (UTA - Ecuador) [49] acknowledges financial support from SENESCYT (National Secretary of Science, Technology and Innovation, Quito-Ecuador) [50] for his PhD stage at Carlos III of Madrid University [51].

1.4 References

[1] T. Kleine and T. Nagatsuma, "A review on terahertz communications research," *J. Infrared Millim. Terahertz Waves*, vol. 32, no. 2, pp. 143–171, 2011.

[2] Thomas R. Clark Jr., Timothy P. McKenna, and Jeffrey A. Nanzer, "Photonic Millimeter Wave System for High Capacity Wireless Communications". *Johns Hopkins APL Technical Digest*, vol. 33, no. 1, 2015, www.jhuapl.edu/techdigest.

[3] S. Koenig, D. Lopez-Diaz, J. Antes, F. Boes, R. Henneberger, A. Leuther, A. Tessmann, R. Schmogrow, D. Hillerkuss, R. Palmer, T. Zwick, C. Koos, W. Freude, O. Ambacher, J. Leuthold, and I. Kallfass, "Wireless sub-THz communication system with high data rate," *Nature Photon.*, vol. 7, no. 12, pp. 977–981, Oct. 2013.

[4] T. Nagatsuma, H. J. Song, and Y. Kado, "Challenges for ultrahigh-speed wireless communications using terahertz waves," *Terahertz Science and Technology*, vol. 3, no. 2, pp. 55-65. 2010.

[5] J. Federici and L. Moeller, "Review of terahertz and sub-Terahertz wireless communications", *J. Appl. Phys.*, vol. 107, no. 11, pp. 1–22, 2010.

[6] A. J. Seeds, H. Shams, M. J. Fice, and C. C. Renaud, "TeraHertz Photonics for Wireless Communications," *IEEE J. Lightwave Technology*, vol. 33, no. 3, pp. 579-587, 2015.

[7] Communicators with Martin Cooper Interview, December 4th, 2014.

[8] N. Guo, R. C. Qiu, S. S. Mo, and K. Takahashi, "60-GHz millimeter-wave radio: Principle, technology, and new results," *EURASIP Journal on Wireless Communications and Networking*, pp. 1-8. 2007

[9] C. Stallo, E. Cianca, S. Mukherjee, T. Rossi, M. De Sanctis, and M. Ruggieri, "UWB for multi-gigabit/s communications beyond 60 GHz," *Telecommunication Systems*, vol. 52, no. 1, pp. 161-181, 2013.

[10] L. Riche, "The performance of high-order quadrature amplitude modulation schemes for broadband wireless communication systems," *ETD Collection for AUC Robert W. Woodruff Library*, paper 300, 2012.

[11] M. Luigi, "E-Band and V-Band - Survey on status of worldwide regulation," *ETSI White Paper*, no. 9, pp. 1-39, June 2015.

[12] Y. Xiao, &J. Rosdahl, "Throughput and delay limits of IEEE 802.11," *IEEE Communications Letters*, vol. 6, no. 8, pp. 355-357, 2002.

[13] N. Cvijetic, Dayou Qian, Jianjun Yu, Yue-Kai Huang, and Ting Wang, "100 Gb/s per channel free-space optical transmission with coherent detection and MIMO processing," *in Proc. 35th Eur. Conf. Opt. Commun.*, pp. 1–2 , 2009.

[14] A. Hirata, M. Harada, and T. Nagatsuma, "120-GHz Wireless Link Using Photonic Techniques for Generation, Modulation, and Emission of Millimeter-Wave Signals," *IEEE J. Lightwave Technology*, vol. 21, no. 10, pp. 2145-2153, 2003.

[15] S. Diddams, D. Jones, J. Ye, S. Cundiff, J. Hall, J. Ranka, & R. Windeler, "Direct RF to optical frequency measurements with a femtosecond laser comb," *IEEE Transactions on Instrumentation and Measurement*, vol. 50, no. 2, pp. 552-555, 2001.

[16] M. Tonouchi, "Cutting-edge terahertz technology", *Nature Photon.*, vol. 1, pp. 97-105, 2007.

[17] H. Song, N. Shimizu, T. Furuta, K. Suizu, H. Ito, & T. Nagatsuma, "Broadband-frequency-tunable sub-terahertz wave generation using an optical comb, AWGs, optical switches, and a uni-traveling carrier photodiode for spectroscopic applications", *IEEE J. Light wave Technology.*, vol. 26, no. 15, pp. 2521-2530, 2008.

[18] J. Federici, B. Schulkin, F. Huang, D. Gary, R. Barat, F. Oliveira, and D. Zimdars, "THz imaging and sensing for security applications—explosives, weapons and drugs", *Semiconductor Science Technology*, vol. 20, pp. 266-280. 2005.

[19] ITU, "Recommendation P.676-9, Attenuation by atmospheric gases", 2012.

[20] ITU, "Recommendation P.840-4, Attenuation due to clouds and fog", 2009.

[21] ITU, "Recommendation P.838-3, Specific Attenuation Model for Rain for Use in Prediction Methods", 2005.

[22] T. Nagatsuma, S. Horiguchi, Y. Minamikata, Y. Yoshimizu, S. Hisatake, S. Kuwano, N. Yoshimoto, J. Terada, and H. Takahashi, "Terahertz wireless communications based on photonics technologies," *Opt. Express*, vol. 21, no. 20, pp. 23736-23747, 2013.

[23] A. Hirata, R. Yamaguchi, T. Kosugi, H. Takahashi, K. Murata, T. Nagatsuma, N. Kukutsu, Y. Kado, N. Iai, S. Okabe, S. Kimura, H. Ikegawa, H. Nishikawa, T. Nakayama, and T. Inada, "10-Gbit/s wireless link using InP HEMT MMICs for generating 120-GHz-band millimeter-wave signal," *IEEE Trans. Microw. Theory Tech.*, vol. 57, no. 5, pt. 1, pp. 1102–1109, May 2009.

[24] I. Kallfass, J. Antes, T. Schneider, F. Kurz, D. Lopez-Diaz, S. Diebold, H. Massler, A. Leuther, and A. Tessmann, "All Active MMIC-Based Wireless Communication at 220 GHz," *IEEE Trans. THz Sci. Technol.,* vol. 1, no. 2, pp. 477-487, 2011.

[25] A. Hirata, T. Kosugi, H. Takahashi, R. Yamaguchi, F. Nakajima, T. Furuta, H. Ito, H. Sugahara, Y. Sato, and T. Nagatsuma, "120-GHz-band millimeter-wave photonic wireless link for 10-Gb/s data transmission," *IEEE Transactions on Microwave Theory and Techniques*, vol. 54, no. 5, pp. 1937-1944, 2006.

[26] A. Stohr, "Photonic millimeter-wave generation and its applications in high data rate wireless access," *IEEE Top. Meeting on Microwave Photonics (MWP)*, 5-9 Oct. 2010.

[27] J. Capmany, and D. Novak, "Microwave photonics combines two worlds," *Nature Photonics* , vol. 1, pp. 319-330, June 2007.

[28] T. Nagatsuma, and K. Kato, "Photonically-assisted 300-GHz wireless link for real-time 100-Gbps transmission," *IEEE MTT-S International Microwave Symposium (IMS)*, pp.1-4, 1-6 June 2014.

[29] A. Stohr, A. Akrout and others, "60 GHz radio-over-fiber technologies for broadband wireless services," *Journal of Optical Networking*, vol. 8, no. 5, pp. 471-487, 2009.

[30] G. Carpintero, R. Guzman, C. Gordon, G. Kervella, M. Chtioui, & F. Van Dijk, "Photonic Integrated Circuits for Radio-frequency signal generation," *IEEE J. Lightwave. Technology*., vol. 34, no. 32, pp. 508-515, 2016.

[31] Z. Fan, and M. Dagenais, "Optical Generation of a mHz-Linewidth Microwave Signal Using Semiconductor Lasers and a Discriminator-Aided Phase-Locked Loop," *IEEE Trans. Microwave Theory and Tech*., vol. 45, no. 8, pp. 1296-1300, 1997.

[32] A. Hirata, M. Harada, K. Sato, and T. Nagatsuma, "Low-Cost Millimeter-Wave Photonic Techniques for Gigabit/s Wireless Link," *IEICE Transactions on Electronics* , vol. E86-C, no.7, pp.1123-1128, 2003.

[33] D. Chen, H. Fetterman, A. Chen, W. Steier, L. Dalton, W. Wang, and Y. Shi, "Demonstration of 110 GHz electro-optic polymer modulators," *Applied Physics Letters,* vol. 70, no. 25, pp. 3335-3337, 1997.

[34] A. Coldren , S. Parker, A Sivananthan, M. Lu, and L. Johansson, "Integrated Phase-locked Multi-THz Comb for Broadband Offset Locking," *Optical Fiber Communication Conference and the National Fiber Optic Engineers Conference (OFC/ NFOEC),* pp.1-3, 4-8 March 2012.

[35] K. Sato, "100 GHz optical pulse generation using Fabry-Perot laser under continuous wave operation," *Electron Letters*, vol. 37, no. 12, pp. 763-764, 2001.

[36] K. Sato, I. Kotaka, Y. Kondo, and M. Yamamoto, "Active mode locking at 50 GHz repetition frequency by half- frequency modulation of monolithic semiconductor lasers integrated with electro absorption modulators," *Appl. Phys. Lett.* , vol. 69, no. 18, pp. 2626-2628, 1996.

[37] T. Nagatsuma, N. Kukutsu, and Y. Kado, "Photonic Generation of Millimeter and Terahertz Waves and Its Applications," *Automatika,* vol. 49, pp. 51-59, 2008.

[38] L. Moeller, A. Shen, C. Caillaud, and M. Achouche, "Enhanced THz generation for wireless communications using short optical pulses, " *In Infrared, Millimeter, and Terahertz Waves (IRMMW-THz)*, pp. 1-3, 2013.

[39] H. Takara, "High-speed optical time-division-multiplexed signal generation," *Opt. Quantum Electron*, vol. 32, pp. 795-810, 2001.

[40] M. M. Mielke, G. A. Alphonse, and P. J Delfyett, "Multiwavelength modelocked semiconductor lasers for photonic access network applications," *IEEE Journal on selected Areas in Communications*, vol. 25, no. 3, pp. 120-128, 2007.

[41] S. Arahira, Y. Matsui, and Y. Ogawa, "Mode-locking at very high repetition rates more than terahertz in passively mode-locked distributed-Bragg-reflector laser diodes," *IEEE Journal of Quantum Electronics*, vol. 32, no. 7, pp. 1211-1224, 1996.

[42] D. J. Derickson, R. J. Helkey, A. Mar, J. G. Wasserbauer, Y. G. Wey, and J. E. Bowers, "Microwave and millimeter wave signal generation using mode-locked semiconductor lasers with intra-waveguide saturable absorbers," *IEEE Microwave Symposium Digest*, vol. 2, pp. 753-756, 1992.

[43] DiDACTIC project, http://www.mineco.gob.es/portal/site/mineco/.

[44] DIFRAGEOS project, http://www.madrid.org/cs/Satellite?cid=1142321526158& pageid=1191581 521356&pagename=PortalJoven/JUVE_Generico_FA/JUVE_generico.

[45] SMART Photonics, The pure play InP Photonics Foundry, http://smartphotonics.nl/.

[46] Cobra research Institute, Eindhoven University of Technology, Eindhoven, Netherlands. 5612AZ. https://www.tue.nl/en/university/departments/electrical-engineering/research/research-institutes/ research- institute-cobra-andresearch-center-for-integrated-nanophotonics/.

[47] PhoeniX Software, http://www.phoenixbv.com.

[48] J. Javaloyes and S. Balle, "Freetwm: a simulation tool for multisection semiconductor lasers," available at http://www.uib.es/depart/dfs/onl/Softwares, 2012.

[49] Technical University of Ambato, Faculty of systems electronics and industrial engineering, Ambato, Ecuador, http://www.uta.edu.ec/v3.0/index.php/es/.

[50] SENESCYT, National Secretary of Science, Technology and Innovation, Quito, Ecuador, 170516. http://www.educacionsuperior.gob.ec/.

[51] Carlos III of Madrid University, Department of Electronics Technology, Leganés, Madrid, Spain, 28911. http://www.uc3m.es/Inicio.

Chapter 2

Fundamentals of Mode-Locked Laser

2.1 Fabry-Perot Laser

A Fabry-Perot (FP) laser is the simplest structure of semiconductor lasers based on a Fabry-Perot cavity resonator containing a gain section within a cavity length (L_{cav}) between two mirrors. The gain section provides the optical gain in a laser diode in order to overcome the cavity loss and achieve the laser operating regime [1]. The laser emission of a Fabry-Perot laser is a set of longitudinal resonator modes (m) separated by the optical mode spacing (Δf_{rep}) between any two adjacent modes [2] as shown in Figure 2.1. The mode spacing is defined by the speed of light and the resonator length, described by the relation in Eq. (2.1).

$$\Delta f_{rep} = \frac{c}{2nL_{cav}} \qquad (2.1)$$

Where:

$\Delta f_{rep} = optical\ mode\ spacing$

$c = speed\ of\ light$

$n = group\ refractive\ index$

$L_{cav} = cavity\ length$

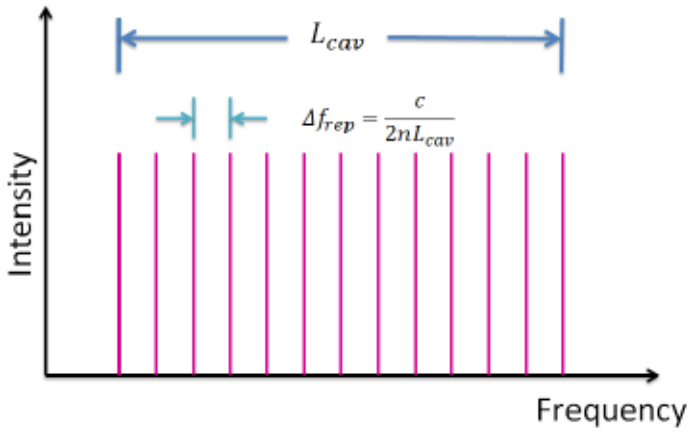

Figure 2.1. Longitudinal cavity modes.

All lasers produce the oscillating modes over some natural bandwidth or range of frequencies. The bandwidth of a laser is determined mainly by the gain section contained into the laser cavity, and the range of frequencies over which a laser may operate is known as the spectral bandwidth Δv at the full-width half-maximum (FWHM) which is depicted in Figure 2.2(a). Thus, the number of modes that oscillate is defined by the spectral bandwidth over which the laser gain exceeds the cavity loss. The optical spectrum of oscillating modes is sketched in Figure 2.2(b).

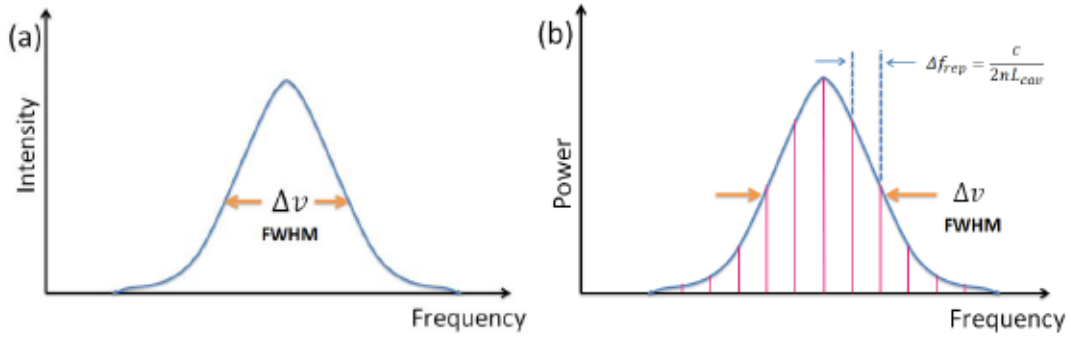

Figure 2.2. (a) Spectral bandwidth. (b) Optical spectrum of oscillating modes.

The output of the laser $E(t)$ defined in Eq. (2.2), only considering the time distribution(t), is given as a sum of frequency components that correspond to the oscillating modes.

$$E(t) = \sum_{m} A_m \, e^{i\,[(m_o + m\,\Delta f_{rep})t + \phi_m]} \qquad (2.2)$$

Where:

$A_m = Amplitude\ of\ the\ mth\ mode$

$m = th\ resonator\ mode = \ 0, 1, 2, 3\ \ldots$

$m_o = Fundamental\ mode$

$\phi_m = Phase\ \ of\ the\ mth\ mode$

$t = Time$

In FP lasers, the relative phases between the oscillating modes are randomly fluctuating when nothing fixes the phases (ϕ_m). The laser output will vary randomly in time and the average power being approximately equal to the simultaneous one.

2.2 Mode-Locked Regime

When the oscillating modes are forced to maintain a fixed phase and amplitude relationship as described in Eq. (2.3) and Eq. (2.4). The resulting operation regime is known as mode-locked [2].

$$\phi_m - \phi_{m-1} = \delta\phi \qquad (2.3)$$

$$A_m\, e^{i\phi_m} = A_o\, e^{i\,(\phi_o + m\,\delta\phi)} \qquad (2.4)$$

Where:

$\delta\phi = fixed\ phase\ relation\ among\ modes$

$\phi_{m-1} = phase\ of\ the\ previous\ mode$

$A_o = Amplitude\ of\ the\ fundamental\ mode$

$\phi_o = Phase\ of\ the\ fundamental\ mode$

Then, the output of the laser will be a periodic function of time defined in Eq. (2.5):

$$E(t) = A_o\, \frac{\sin\left[(k+1)\,\Delta f_{rep}\ t_1/2\right]}{\sin\left[\,\Delta f_{rep}\ t_1/2\right]}\, e^{i m_o t} \qquad (2.5)$$

Where:

$\Delta f_{rep} = fundamental\ repetition\ rate\ frequency$

$k = number\ of\ locked\ modes$

$t_1 = t + \delta\phi/\,\Delta f_{rep}$

The operating condition determined by Eq. (2.3) and Eq. (2.5) results in the generation of a train of regularly spaced optical pulses. The term mode-locked is a dynamic regime which refers to the fixed phase relation among modes of a multi-mode laser spectrum. The phases of the different spectral components are said to be locked when they differ only by a constant phase shift at all times [3]. Therefore, the mode-locked laser diode (MLLD) is a pulsed source which allows emitting ultrashort pulses in the range of picoseconds and sub-picoseconds under mode-locked conditions [4].

The pulse train generated by a MLLD is shown in Figure 2.3, in which the time between pulses (ΔT_{rep}) and the pulse width $(\Delta\tau)$ at the full-width half-maximum (FWHM) are identified. Also, the fundamental repetition rate frequency has an inverse relation to the time between pulses of the mode-locked laser diode which is described in Eq. (2.6). The pulse width defined in Eq. (2.7) can be calculated from the optical mode spacing and the number of modes (N) within the envelope at full-width half-maximum of the spectral bandwidth [5].

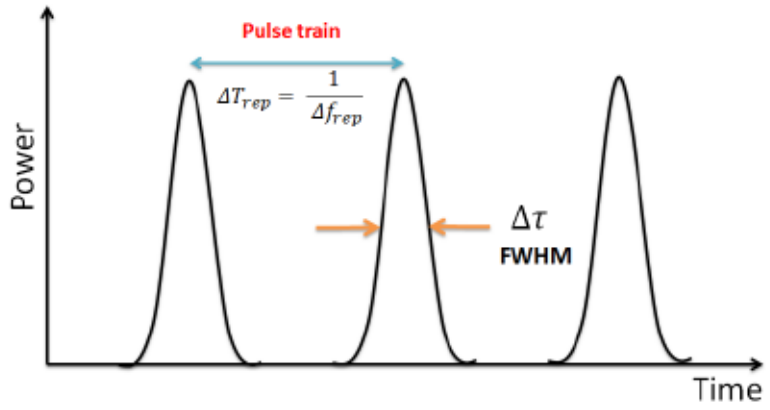

Figure 2.3. Pulse train from a MLLD.

$$\Delta T_{rep} = \frac{1}{\Delta f_{rep}} \qquad (2.6)$$

$$\Delta\tau = \frac{2nL}{N\,c} = \frac{1}{N\,\Delta f_{rep}} \qquad (2.7)$$

Where: $\Delta T_{rep} = time\ between\ pulses$

$\Delta\tau = pulse\ width$

$N = number\ of\ modes\ within\ the\ spectral\ bandwidth$

The spectral bandwidth and the pulse width define the time-bandwidth product (TBP) which is described in Eq. (2.8). The TBP indicates how close the pulse duration is to the limit that is set by its spectral bandwidth [6]. The transform limited pulse is such pulse which is as short as its spectral bandwidth permits. The TBP is a figure of merit to establish the quality of a source.

$$TBP = \Delta v * \Delta\tau \qquad (2.8)$$

The importance of mode-locked lasers is their diverse applications. MLLDs have been researched for a number of years for a wide range of applications [7]. In communication systems, mode locking lasers have served as stable pulse sources in optical time division multiplex (OTDM) systems [8], or as multi-wavelength sources in wavelength division multiplex (WDM) networks [9]. Mode-locking lasers can generate ultra-short optical pulses which have application for millimeter and terahertz wave generation [10], [11], high-speed sampling [12], high-speed clock acquisition [13], ultrahigh-speed logic [14], ultrafast signal processing [15], analogue to digital conversion [16], spectroscopy [17] and so on.

2.3 Structure of Semiconductor Mode-Locked Laser Diode

The simplest structure of a mode-locked laser diode (MLLD) is composed by two main elements, a gain section and an absorber section. The first is implemented using a semiconductor optical amplifier (SOA), while the saturable absorber (SA) is a reverse bias SOA section. The structure of MLLD with the SOA and SA, between two cleaved facets is depicted in Figure 2.4. MLLD have the advantages of semiconductor lasers, such as easy manufacturability, compactness, high potential for integrability, ease of pumping, etc. [18]. The gain and the absorption sections in a MLLD play an essential role in the optical pulse generation. Both sections contribute to establish the pulse profile by the interplay of pulse compression in the absorber section and the pulse broadening in the gain section [19].

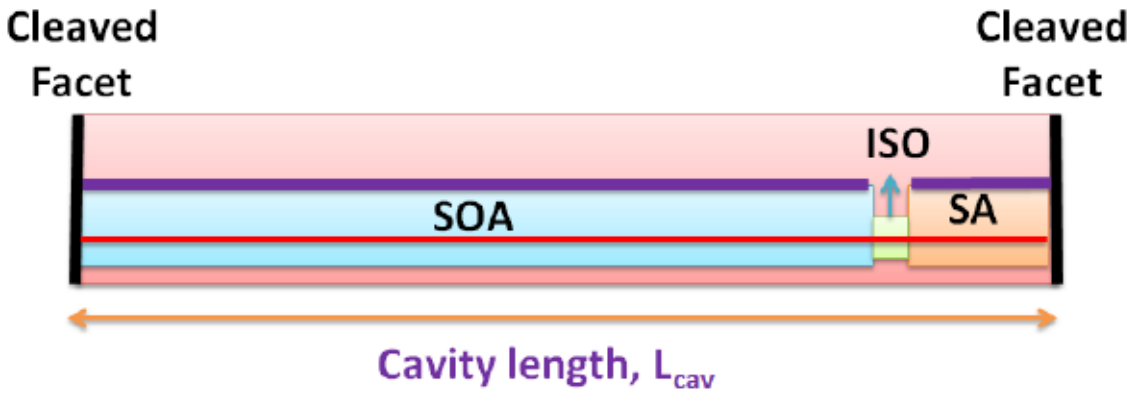

Figure 2.4. Simplest structure of a mode-locked laser. SOA and SA separated by an isolator (ISO).

The gain section provides a finite bandwidth which set the lower limit for the pulse width in a mode locking laser. The study of MLLD using time-domain modeling reveals that the pulse broadening from the gain bandwidth is widely accredited to the gain

saturation [20]. The gain saturation is attributable to the reduced instantaneous gain due to the finite scattering times related with the spectral hole burning and carrier heating which are time constants in the order of 50-100 fs [21], [22], [23]. Also, the pulse broadening while increasing the gain current is usually attributable to self-phase modulation (SPM) [24], and the group velocity dispersion induced by the gain dispersion [25]. Besides, the pulse duration is sensitive to another design parameter like the contact geometries, which have been demonstrated to achieve near Fourier limited pulse widths [19].

The purpose of the absorber section is to force a fixed phase relation among the oscillating modes into the cavity [2]. The absorber section has an important incidence in the pulse width of the MLLD. On one hand, the pulse width compression is observed while reducing the length of the absorber section [7]. Absorber lengths of order 20 um – 80 um have been implemented in experimental [26] and simulation results of MLLD [27]. Also, mode locking operating regimes have been obtained from devices with absorber lengths required to be 1% - 3% of the resonator cavity length [22], [28]. On the other hand, the pulse width also reduces while decreasing the absorber recovery time [22].The recovery time of the absorber has strong dependence on the absorber reverse voltage [29]. So, it has been demonstrated how the pulse width decreases exponentially while the reverse voltage increases in negative value. As and added value, the saturable absorption mainly causes a pulse compression by reducing the loss at the peak of the pulse [7].

2.3.1 Cavity Configuration.

An important aspect of the mode-locked laser structures is the number and location of the saturable absorber sections within the Fabry-Perot cavity. Also, the interplay between SOA and SA sections has been extensively studied [7]. MLLDs can operate either at its fundamental repetition rate frequency or even at higher frequencies. When the MLLD works at higher frequency than the fundamental repetition rate, it is called harmonic mode-locked (HML) laser [30]. The cavity configuration can help to define the fundamental repetition rate and also increase the fundamental repetition rate frequency in order to achieve harmonic mode locking operation regimes [30], [31]. The simplest cavity configuration is obtained when the SA is located at one extreme of the FP cavity. Mode locking regimes at the fundamental repetition rate frequency are achieved and the arrangement is called self-colliding mode locking laser (sCPM) [28] which is depicted in Figure 2.5 (a).

Harmonic mode-locked can be reached placing the SA sections at specific locations within the FP cavity [31]. So, HML structures have been achieved through symmetric and asymmetric colliding pulse mode-locked geometries. The Nth harmonic of the round-trip frequency has been achieved with N increasing from N = 2 to N= 12. On one hand, repetition rates at 192 GHz [30], 240 GHz [32] and 377 GHz [33] were realized with one or more SAs located at multiples of an integer fractional position L_{cav} /N of the cavity length, where N is the Nth harmonic of the round trip frequency. Thus, when the SA is located in the middle of the cavity, the N = 2 harmonic is generated and the configuration is named symmetric colliding or just colliding pulse mode-locking, (CPM) [34] and shown in Figure 2.5(b). The N = 3 or 4 harmonics are realized when the SA is placed in the 1/3 and 1/4 positions of the laser cavity, respectively and the pattern

is termed multiple colliding pulse mode-locking (mCPM) [35] which is sketched in Figure 2.5(c). Also, other structures as shown in Figure 2.5 (d) use more than one SA with the intention of enhance the mCPM regime [30], [36]. On the other hand, higher repetition rates up to 860 GHz [31] have been reached with a single SA situated at the position $M.L_{cav}/N$ of the cavity length, where M and N are relative prime (M<N). In this case, the N harmonic is N = 12 and the mode locking structure is called asymmetric colliding pulse mode-locking (ACPM) which is depicted in Figure 2.5 (e). We would like to highlight that all these structures [30]…, [36] use cleaved facet mirrors.

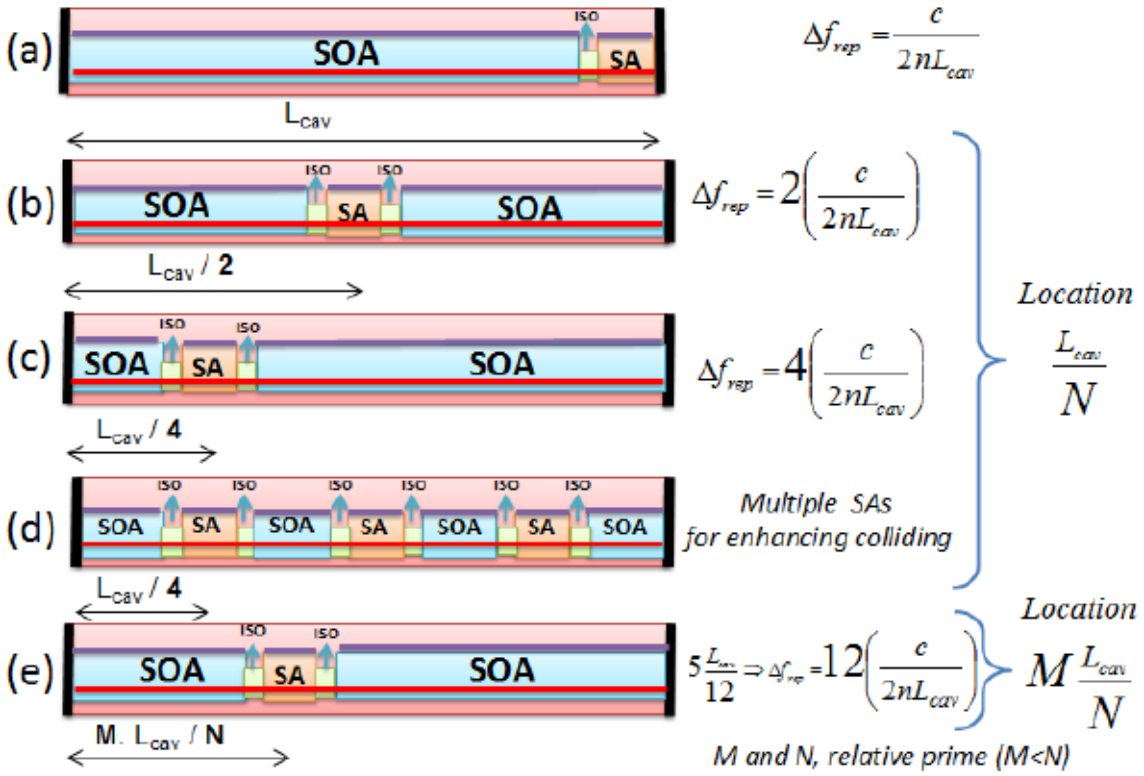

Figure 2.5. Cavity configuration of MLLD. (a) Self-colliding. (b) Colliding. (c) Multiple colliding. (d) Multiple colliding with several SAs. (a) Asymmetric colliding.

2.4 Mode-Locked Techniques

The great advantage of the mode locking technique is that it is capable to generate shorter pulses than gain and Q-Switching techniques [2]. The mode locking can be realized by three standard methods. They are active, passive and hybrid mode locking.

2.4.1 Active Mode-Locked

The active mode locking method is one of the first efforts in order to achieve mode locking regimes. This method consists in modulating an optical loss or gain inside the resonator cavity. The key requirement is to provide a frequency from an electronic source reference (radio frequency, RF) that is equal to the optical mode spacing defined by the round-trip time [2]. When the electronic source offers a signal which meets the fundamental repetition rate frequency of the laser cavity and the optical section supports amplification at minimal loss, the active mode locking is realized and it allows producing a train of optical pulses with a pulse width shorter than the round trip time [37]. The main limitation of active mode locking is to apply this method in lasers with small lengths. For instance in a laser with 400 μm length an electronic source reference at 100 GHz is required but actually an electronic source at such frequency does not exist. For this reason, the active mode locking method has been successfully implemented in external cavity lasers in which lower frequencies from the electronic source reference is required [2].

Active mode-locked regimes have been reported by using either Mach-Zehnder [38] or acousto-optic modulator [39]. In the modulation process, the current modulation causes the modulation of the carrier density around the threshold value (n_{th}). The current

modulation allows creating a very short time window of the net gain in the laser and this implies generating a pulse (significantly shorter than the round trip time) when the carrier density exceeds the threshold value for a short time during each modulation period [2]. The structure of a single contact semiconductor diode laser and the modulation process in active mode-locked are depicted in Figure 2.6(a) and Figure 2.6(b), respectively.

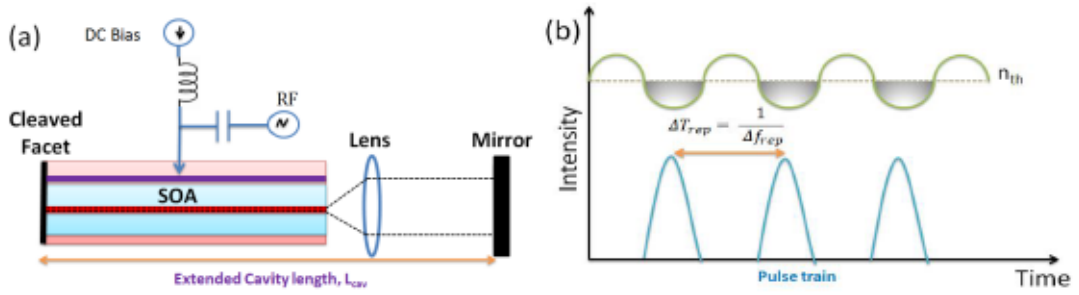

Figure 2.6. (a) Active mode-locked structure. (b) Modulation process in active mode-locked.

2.4.2 Passive Mode-Locked

One of the simplest methods to achieve mode-locked regimes is the passive method which only requires the forward bias of the gain section and the reverse bias of the saturable absorber section. Passive mode-locking does not require the electronic source reference, so this technique avoids the limitation of the electrical bandwidths of the active mode locking method and it has been stated that passive mode locking is a promising method for the pulse width compression and also for increasing the repetition rate [40]. By using the passive mode locking method, pulses less than 1 ps [41], [42] and repetition rates exceeding 1 THz [11], [43] has been reported.

The concept of passive mode-locking in semiconductor lasers is based on a mechanism which combines a slow gain saturation recovery and a slow SA saturation

recovery [44], [45]. The structure of the passive mode-locking is sketched in Figure 2.7(a). The saturation process in a slow saturable absorber passive mode-locked is carried out when the optical pulse is travelling back and forth and saturates the SA. Then, the leading edge of the pulse becomes steeper and the peak experiences a high net gain. Next, the gain in the amplifier is saturated towards the trailing edge of the pulse. The gain and SA saturation processes have recovery times that are much longer than the pulse duration. By combining both processes in a way that the SA saturation process precedes the gain saturation, a short net gain window appears and in consequence the optical pulse creation [2]. The saturation process in a slow saturable absorber passive mode-locked laser is depicted in Figure 2.7(b).

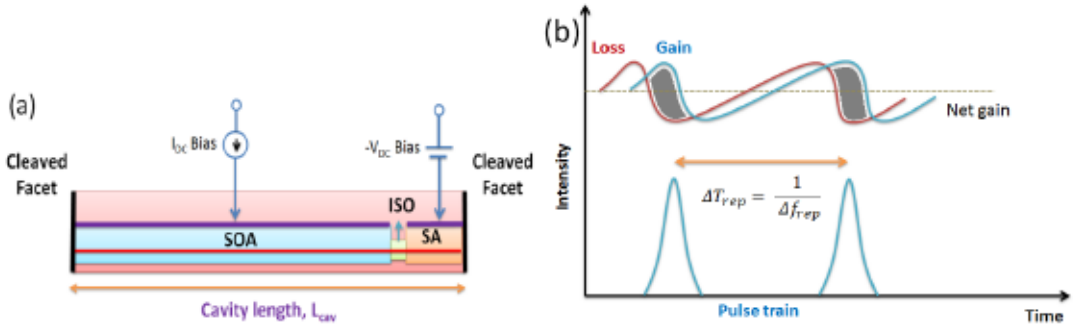

Figure 2.7. (a) Passive mode-locked structure. (b) Saturation process in passive mode-locked.

2.4.3 Hybrid Mode-Locked

The combination of active and passive mode-locked provides another method called hybrid mode-locked. This method uses the reverse bias applied in passive method and the modulation from the active method, so the reverse bias applied to the absorber section is modulated at a frequency close to the repetition rate [46]. Hybrid mode locked improves the stability of the mode locking regime by reducing the jitter down to

hundreds of femtoseconds while the influence on the pulse width and shape is negligible [47], [48]. The structure of the hybrid mode-locked is sketched in Figure 2.8.

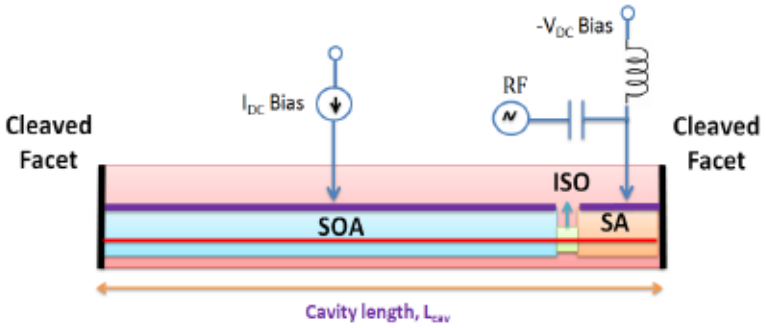

Figure 2.8. Hybrid mode-locked structure.

2.5 Mode-Locked Characterization Methods

The characterization of the pulsed signal from a mode-locked laser often requires high performance of the used instrumentation in terms of operation range, sensitivity, resolution and so on. The properties of the optical pulse train generated by mode-locked lasers need to be characterized by different measurements mainly frequency spectrum and pulse width to evaluate the time bandwidth product. Also, noise measurements are required to estimate the stability of the pulsed signal.

2.5.1 Frequency Spectrum Measurement

Considering the generated pulsed signal from a mode-locked laser at 193.5 THz and the pulse repetition rate in order of GHz after being converted into an electrical domain by a photodiode the optical and the electrical spectrum analyzers are used, respectively.

Measurements with the Optical Spectrum Analyzer (OSA)

The OSA delivers information about the optical mode spectrum of the generated pulse train by measuring and displaying the distribution of power of the MLLD over a specified wavelength range [49]. In the frame of this work the optical spectrum was observed with a Yokogawa AQ6370B optical spectrum analyzer (OSA, resolution 0.02 nm, 2.5 GHz). The key parameters of MLLD obtained from the optical spectrum are the optical power, operation wavelength, and optical mode spacing. Particularly, the OSA allows measuring the power difference between two adjacent optical modes for colliding pulse mode-locked lasers, which we have named side mode suppression ratio. Also, the OSA allows estimating qualitatively the mode locking regime and self-phase modulation by considering the optical spectrum symmetry and shape envelope without any additional spectral components [50]. Figure 2.9 depicts the Yokogawa AQ6370B OSA available in the laser characterization laboratory.

Figure 2.9. Yokogawa AQ6370B, Optical Spectrum Analyzer.

Measurements with the Electrical Spectrum Analyzer (ESA)

The ESA function is to display the electrical frequency content of the input signal after being converted into electrical domain by a high speed photodiode (HF-PD) [51].

The available ESA in the laser characterization laboratory is the Anritsu MS2668C electrical spectrum analyzer [52]. We have two photodiodes. The first one with 40 GHz -3 dB bandwidth U2T XPDV2120R PIN-photodiode [53] and the second one with 90 GHz -3 dB bandwidth U2T XPDV4120R PIN-photodiode [54]. Also, we have two external mixers (MXRs) to down-convert the repetition rate frequency of the signal to the input range of the electrical spectrum analyzer. One of them is the Anritsu MA2744A (50 GHz - 75 GHz) [55] and the other is the Rohde & Schwarz FS-Z110 (75 GHz - 110 GHz) [56]. Figure 2.10(a) and Figure 2.10(b) depict the electrical spectrum analyzer and one of the photodiodes available in the laser characterization laboratory, respectively.

Figure 2.10. (a) Anritsu MS2668C Electrical spectrum analyzer. (b) U2T XPDV2120R PIN photodiode

2.5.2 Pulse Width Measurement

Generally, the pulse width measurement is limited by the bandwidth and the resolution of the detector. For example, in order to have an idea of the limitation of bandwidth and resolution, the measurement of the pulse width of $\Delta\tau = 1\,ps$ needs a detector bandwidth up to 1 THz for exact recovery of the pulse shape. There are

different devices for pulse width measurements such as streak cameras, optical sampling oscilloscopes, electrical sampling oscilloscopes, and autocorrelators [2]. Among them, the commonly used device is the autocorrelator (AC).

The autocorrelation is carried out between the pulse train and the delayed replica of the pulse train which coincide in a nonlinear crystal for second harmonic generation (SHG). The phase matching between the incoming signal and the generated second harmonic signal into the nonlinear crystal allow achieving the efficient second harmonic generation. Then, the second harmonic light is detected by a photomultiplier tube or photodiode, which has been filtered to block transmission of light at the wavelength of the laser. By last, the autocorrelation measurement is achieved when moving one of the retro reflectors on a shaker with a frequency of several Hertz [57].

The measurement results in the autocorrelation function $G_{(\tau)}$ described in Eq. (2.9), which provides the pulse width ($\Delta\tau$) at the FWHM by comparison with the autocorrelation traces of known input pulse shapes [58]. The $\Delta\tau$ value is obtained by multiplying the FWHM of the autocorrelated signal ($\Delta\tau_{AC}$) with the deconvolution factor ($\Delta\tau/\Delta\tau_{AC}$).

$$G_{(\tau)} = \frac{\int I(t).I(t-\tau)\,dt}{\left|\int I^2\,dt\right|} \qquad (2.9)$$

The autocorrelation function $G_{(\tau)}$ does not contain information of the pulse temporal orientation of leading and trailing edge of the pulse, nor about trailing or previous pulse pedestals. Also, the autocorrelation is independent of timing jitter because of the simultaneous influence on both pulse replicas and the measurement omits phase information [57].

The common functions for deconvolution and estimation of measured pulse shapes are depicted in Table 2.1

Pulse -shape	Intensity $I_{(t)}$	$G_{(\tau)}$	$\Delta\tau/\Delta\tau_{AC}$	$TBP = \Delta v * \Delta\tau$
Gaussian	e^{-t^2}	$e^{\left(\frac{-\tau^2}{2}\right)}$	0.7071	0.4413
Hyperbolic Secant	$sech^2(t)$	$3\frac{\tau\, coth(\tau) - 1}{sinh^2(\tau)}$	0.6482	0.3148
Lorentzian	$\frac{1}{1+t^2}$	$\frac{1}{1+\left(\frac{\tau}{2}\right)^2}$	0.5000	0.2206
Symmetric Exponential	$e^{-2\lvert t\rvert}$	$(1+2\tau)e^{(-2\lvert\tau\rvert)}$	0.4130	0.1420

Table 2.1. Pulse shape functions for autocorrelation measurements [58].

Enough SHG intensity is required to avoid disturbing measurement floors. For this reason, the measurement of optical pulse signals from a MLLD is usually carried out increasing the optical signal level using an erbium doped fiber amplifier (EDFA). The available autocorrelator and EDFA in the laser characterization laboratory is the APE (applied physics and electronics) Pulse-Check autocorrelator [57] and Nortel FA14UFAC telecom erbium doped fiber amplifier [59], respectively.

2.5.3 Noise Measurement

Another set of measurements are needed to quantify the deviation of the generated optical pulses from a perfect train of identical pulses. Deterministic noise and random fluctuations are the components of the total noise. Deterministic noise usually comes from insufficient locking of harmonic modes in laser sources while random fluctuations are caused by the quantum nature of the emission by spontaneous amplification processes [50].

In the frame of this work, two kinds of noise are considered in the pulse train such as amplitude noise (AN) and phase noise (PN) which are depicted in Figure 2.11. The AN is the variation from the average pulse energy while the PN is the deviation from the arrival time expected for a pulse in a perfect pulse train. The phase noise allows defining the timing jitter which provides a number for the stability in terms of femto seconds and the amplitude noise describes the amplitude jitter in terms of power ratio to a carrier signal (dBc) [60]. Using the Von der Linde method, which establishes the noise in the electrical spectrum of the MLLD, the timing jitter can be extracted from the integration of the single side band phase noise level over a frequency range [61] while the amplitude jitter is defined by the integration of the relative intensity noise [62]. It is common to use the international telecommunications union (ITU) recommended integration ranges defined by viable clock recovery techniques [63], in order to define the timing jitter and the amplitude jitter. In the frame of this work, the noise quantification was extracted from the integration range [4-80 MHz] which is used to define the amplitude jitter and the timing jitter [64].

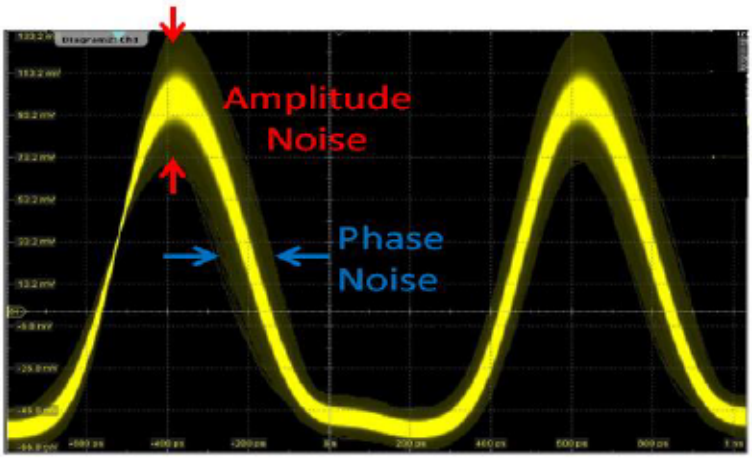

Figure 2.11. Amplitude noise and phase noise in a pulse train.

By last, the features of the used instrumentation available in the laser characterization laboratory are summarized in Table 2.2.

Device	Model	Operation Range	Sensitivity	Resolution	Ref.
OSA	Yokogawa AQ6370B	0.6μm - 1.7μm	-90 dBm	0.02 nm	[49]
ESA	Anritsu MS2668C	9 KHz - 40 GHz	-115 dBm	1 Hz	[51]
PD	U2T XPDV2120R	0 GHz - 40 GHz	0.7 A/W	-	[53]
PD	U2T XPDV4120R	0 GHz - 100 GHz	0.6 A/W	-	[54]
MXR	Anritsu MA2744A	50 GHz - 75 GHz	-	-	[55]
MXR	Rohde & Schwarz FS-Z110	75 GHz - 110 GHz	-	-	[56]
AC	APE Pulse-Check	1.1μm - 1.6μm	10-4 W2	< 1 fs	[57]
EDFA	Nortel FA14UFAC	1525-1565 nm	-14.5 dBm	-	[59]

Table 2.2. Used instrumentation.

2.6 State of the Art of Monolithic Semiconductor Mode-Locked Laser Diodes

The wide range of applications of mode locked lasers is the main reason for the long time research of them. The exploration of mode locking lasers has been carried out with the different methods and structures aforementioned.

Monolithic semiconductor mode-locked laser diodes have many features which have been demonstrated that are capable to be managed with a wide range of choices such as the cavity structure (CS), repetition rate (Δf_{rep}), pulse width ($\Delta\tau$) , time bandwidth product (TBP), linewidth (Δv_{RF}), timing jitter (σ_T), and amplitude jitter (N_{AM}).

Table 2.3 shows the reports of monolithic semiconductor mode-locked lasers with their features in terms of, method, cavity structure, repetition rate, pulse width, time bandwidth product, linewidth, timing jitter, amplitude jitter. The cavity structure will use the following abbreviation for its sections: gain (G), absorber (A), distributed bragg reflector (DBR), modulator (M), passive waveguide (PW) components, quantum well (QW), quantum well intermixing (QWI), type of laser (TL).

Method	Cavity Configuration	Δf_{rep} (GHz)	$\Delta\tau$ (ps)	TBP	$\Delta\nu_{RF}$ (MHz)	σ_T (ps)	N_{AM} (dBc)	TL	Ref.
Active	G-PW	4.4	9	9.6	-	-	-	QW	[65]
	G-PW-DBR	8.1	20	0.34	-	-	-	QW	[66]
	A-G	10	2.4	1	-	0.071	-	QW	[63]
	A-G	16.3	2	1.2	-	-	-	QW	[67]
	A-G	50	3.2	1.0	-	-	-	QW	[68]
Passive	G-A-G-PW	2.5	15	-	0.0063	-	-	QW	[69]
	A-G-PW	9.3	3.5	-	0.300	9.3	-	QWI	[25]
	A-G	10	2.4	1	-	0.570	-	QW	[63]
	A-G	21.31	0.86	0.57	0.030	-	-	QW	[24]
	A-G-M-DBR	40	5	0.44	-	-	0.010 - 0.192	QW	[70]
	PW-DBR-PW-G	40.4	8.8	0.45	-	-	-	QW	[71]
	G-A	80	5.4	0.65	-	-	-	QW	[72]
	A-G-M-DBR	1540	0.43	-	-	-	-	QW	[11]
Colliding	G-A-G	16.7	8	-	-	-	-	QW	[73]
	G-A-G	80	1.28	0.34				QW	[74]
	G-A-G	126	0.43	-	-	-	-	QW	[34]
	G-A-G-A-G-A-G	192	0.75	0.31	1.1	-	-	QW	[30]
	G-A-G-A-G-A-G	240	0.88	0.42				QW	[32]
	G-A-G-A-G-A-G	375	1	0.436	-	-	-	QW	[35]
	G-A-G	377	0.72	-	-	-	-	QW	[33]
	G-A-G	480	0.52	0.31	-	-	-	QW	[75]
	G-A-G	860	-	-	-	-	-	QW	[31]
Hybrid	A-DBR-PW-G	4.9	8.0	0.3	-	-	-	QW	[76]
	A-G-G-PW	20	0.79	0.39	-	-	-	QW	[42]
	A-G-W-DBR	20	8.3	0.32	-	-	-	QW	[77]
	A-G	40	2.8	0.40	-	0.073	-	QW	[78]

Table 2.3. State of the art of MLLD.

From the state of the art of mode-locked laser, we are able to establish the actual limits of mode-locked lasers according to the different methods of implementation. We identify the wide range of repetition rates provided by mode-locked lasers from 2.5 GHz to 1.5 THz [11]. The short pulse durations between 0.43 ps and 8.8 ps. Time bandwidth products lower than one (1) and close to the transform limit. Also, it is important to highlight the low values of linewidth from 300 KHz to 1.1 MHz. Timing jitter lower than 9.3 ps towards 73 fs and amplitude jitter ranging from 0.010 dBc to 0.192 dBc.

As a result, a potential field of application of mode-locked lasers is the generation of carrier wave frequencies in the millimeter and terahertz wave range for broadband wireless communications [79].

Each application field of mode-locked laser has specific requirements. For example, it is essential to address the pulse source requirements for broadband wireless communications. The pulse train requires low timing jitter, at least less than the pulse width or the bit slot. For example a timing jitter of 260 fs is required for an error free operation of 160 Gbit/s systems. Also, the amplitude jitter has to be low due to the fact that higher amplitude jitter reduces the receiver sensitivity and limits the system margin [80].

Other requirements are the quality evaluation of the optical and electrical spectrums of the mode locking lasers. For error free operation transmission systems, optical modes with a large mode comb height are required, preferably more than 20 dBm [50]. Another requirement for error free operation transmission systems is the short linewidth which is estimated essentially in the electrical spectrum. The usefulness of a carrier signal is defined by the linewidth so it is necessary to take into account the linewidth requirements for transmission systems. Linewidths around MHz are useful for direct envelop detection methods [81]. But, for coherent detection we have to consider the MHz linewidth limitation [82] because of a lower linewidth such us 200 KHz is required for higher order modulation schemes.

Finally, it is important to highlight that the main goal of the present work is the design, characterization and experimental application of on-chip mode-locked laser for broadband wireless communications systems.

2.7 Conclusions

- In conclusion, mode-locked lasers have been researched for many years and this kind of lasers have a wide range of applications which reveals the great impact in many areas of science.
- Also, the simplest structure of the monolithic semiconductor mode-locked laser is considered in the frame of this work with the intention of develop new compact devices which are able to generate higher frequencies.
- Finally, the measurement equipment available in the laser characterization laboratory provides the necessary equipment for the characterization of the on-chip mode locked microwave photonic integrated circuits.

2.8 References

[1] L. Coldren, S. W. Corzine, and M. L. Masanovic, "Diode lasers and photonic integrated circuits," New Jersey: *John Wiley & Sons*, 2012.

[2] P. Vasil'ev P, "Ultrafast Diode Lasers: Fundamentals and Applications," London: *Artech House*, 1995.

[3] B. E. Saleh, and M. C. Teich, "Fundamentals of photonics," New York: *Wiley*. 1991.

[4] E. M. Garmire, and A. Yariv, "Laser mode-locking with saturable absorbers". *IEEE Journal of Quantum Electronics*, vol. 3, no. 6, pp. 222-226, 1967.

[5] M. Young, "Optics and lasers: including fibers and optical waveguides," New York: *Springer – Verlag*, 1993.

[6] R. Paschotta, "Encyclopedia of Laser Physics and Technology", Volume A-M, 2012.

[7] K. A. Williams, M. G. Thompson, and I. H. White, "Long-wavelength mononolithic mode-locked diode lasers," *New. J. Phys.*, vol. 6, pp. 1 - 32, 2004.

[8] H. Takara, "High-speed optical time-division-multiplexed signal generation," *Opt. Quantum Electron*, vol. 32, pp. 795-810, 2001.

[9] M. M. Mielke, G. A. Alphonse, and P. J Delfyett, "Multiwavelength modelocked semiconductor lasers for photonic access network applications," *IEEE Journal on selected Areas in Communications*, vol. 25, no. 4, pp. 120-128, 2007.

[10] D. J. Derickson, R. J. Helkey, A. Mar, J. G. Wasserbauer, Y. G. Wey, and J. E. Bowers, "Microwave and millimeter wave signal generation using mode-locked semiconductor lasers with intra-waveguide saturable absorbers," *IEEE Microwave Symposium Digest*, vol. 2, pp. 753-756, 1992.

[11] S. Arahira, Y. Matsui, and Y. Ogawa, " Mode-locking at very high repetition rates more than terahertz in passively mode-locked distributed-Bragg-reflector laser diodes," *IEEE Journal of Quantum Electronics*, vol. 32, no. 7, pp. 1211-1224, 1996.

[12] K. J. Weingarten , M. J. W. Rodwell, and D. M. Bloom, "Picosecond optical sampling of GaAs integrated circuits," *IEEE Journal of Quantum Electronics,* vol. 24, no. 2, pp. 198-220, 1988.

[13] T. Ohno, K. Sato, R. Iga, Y. Kondo, I. Ito, T. Furuta, K. Yoshino, and H. Ito, "Recovery of 160 GHz optical clock from 160 Gbit/s data stream using modelocked laser diode," *Electron. Lett.*, vol. 40, no. 4, pp. 265, 2004.

[14] K. Vlachos, N. Pleros, C. Bintjas, G. Theophilopoulos, and H. Avramopoulos, "Ultrafast time-domain technology and its application in all-optical signal processing," *Journal of Lightwave Technology*, vol. 21, no. 9, pp. 1857-1868. 2003.

[15] H. Kurita, I. Ogura, and H. Yokoyma, "Ultrafast all-optical signal processing with mode-locked semiconductor lasers," *IEICE Trans. Electron*. E81-C 2 129, 1998.

[16] P. W. Juodawlkis, J. C. Twichell, G. E. Betts, J. J. Hargreaves, R. D. Younger, J. L. Wasserman, F. O´Donell, K. Ray, and R. C.Williamson, "Optically sampled analog-to-digital converters," *IEEE Transactions on Microwave Theory and Techniques*, vol. 49, no. 10, pp. 1840-1853, 2001.

[17] T. Gherman, and D. Romanini, " Mode–locked cavity–enhanced absorption spectroscopy," *Optics Express*, vol. 10, no. 19, pp. 1033-1042, 2002.

[18] E. A. Avrutin, J. H.Marsh, and E. L. Portnoi, "Monolithic and multi-Giga Hertz mode-locked semiconductor lasers: Constructions, experiments, models and applications," *IEE Proceedings-Optoelectronics*, vol. 147, no. 4, pp. 251-278, 2000.

[19] S. Bischoff, M. P. So, J. Mo, S. D. Brorson, T. Franck, J. M. Nielsen, and A. Mo, "Pulse shaping mechanism in colliding pulse mode locked laser diodes," *Applied physics letters*, vol. 67, no. 26, pp. 3877-3879, 1995.

[20] W. Yang, and A. Gopinath, "Study of passive mode locking of semiconductor lasers using time domain modeling," *Applied physics letters*, vol. 63, no. 20, pp. 2717-2719, 1993.

[21] U. Bendelow, M. Radziunas, J. Sieber, and M. Wolfrum, "Impact of gain dispersion on the spatio-temporal dynamics of multisection lasers," *IEEE Journal of Quantum Electronics*, vol. 37, no. 2, pp. 183-188, 2001.

[22] S. Bischoff, J. Mørk, T. Franck, S. D. Brorson, M. Hofmann, K. Fröjdh, L. Prip and M. P. Sørensen, "Monolithic colliding pulse mode-locked semiconductor lasers". *Quantum and Semiclassical Optics: Journal of the European Optical Society Part B*, vol. 9, no. 5, pp. 655-674, 1997.

[23] P. A. Morton, R. J. Helkey, and J. E. Bowers, "Dynamic detuning in actively mode-locked semiconductor lasers". *IEEE Journal of Quantum Electronics*, vol. 25 no. 12, pp. 2621-2633, 1989.

[24] K. Merghem, A. Akrout, A. Martinez, G. Moreau, P. Tourrenc, F. Lelarge, F Van Dijk, H. Duan, G. Aubin, and A. Ramdane, "Short pulse generation using a passively mode locked single InGaAsP/InP quantum well laser," *Optics express*, vol. 16, no. 14, pp. 10675-10683, 2008.

[25] F. Camacho, E. A. Avrutin, A. C. Bryce, and J. H. Marsh, "Passive modelocking in semiconductor lasers with monolithically integrated passive waveguides," *IEE Proc.-Optoelectron.*, vol. 145, no. 1, pp. 43– 46, Feb. 1998.

[26] S. Arahira, Y. Katoh, and Y. Ogawa, "Generation and stabilization of ultrafast optical pulse trains with monolithic mode-locked laser diodes," *Optical and Quantum Electronics*, vol. 33, no. 7, pp. 691-707, 2001.

[27] J. Javaloyes, and S. Balle, "Mode-locking in semiconductor Fabry-Pérot lasers," *IEEE Journal of Quantum Electronics*, vol. 46, no. 7, pp. 1023-1030, 2010.

[28] D. J. Jones, L. M. Zhang, J. E. Carroll, and D. D. Marcenac, "Dynamics of monolithic passively mode-locked semiconductor lasers," *IEEE Journal of Quantum Electronics*, vol. 31, no. 6, pp. 1051-1058, 1995.

[29] J. R. Karin, R. J. Helkey, D. J. Derickson, R. Nagarajan, D. S. Allin, J. E. Bowers, and R. L. Thornton, "Ultrafast dynamics in field enhanced saturable absorbers," *Applied physics letters*, vol. 64, no. 6, pp. 676-678, 1994.

[30] Y. Katagiri, A. Takada, "A Harmonic Colliding-Pulse Mode-Locked Semiconductor Laser for Stable Subterahertz Pulse Generation," *IEEE Photon. Technol. Lett.*, vol. 9, no. 11, pp. 1442–1444, Nov. 1997.

[31] T. Shimizu, I. Ogura, H. Yokoyama, "860 GHz rate asymmetric colliding pulse modelocked diode lasers," *Electron. Lett.*, vol. 33, no. 22, pp. 1868–1869, Oct. 1997.

[32] L. Hou, M. Haji, and J. H. Marsh, "240 GHz pedestal-free colliding pulse mode-locked laser with a wide operation range," *Laser Phys. Lett.* , vol. 11, no. 115804, pp. 1-5, 2014.

[33] T. Shimizu, X. Wang, and H. Yokoyama, "Asymmetric colliding-pulse mode-locking in InGaAsP semiconductor lasers," *Optical Rev.*, vol. 2, no. 6, pp. 401-403, 1995.

[34] G. Tandoi, J. Javaloyes, E. Avrutin, C. N. Ironside, and J. H. Marsh, "Subpicosecond colliding pulse mode locking at 126 GHz in monolithic GaAs/AlGaAs quantum well lasers: Experiments and theory," *IEEE J. Sel.Top. Quantum Electron.*, vol. 19, no. 4, pp.1100608, 2013.

[35] J. F. Martins-Filho, S. D. McDougall, E. A. Avrutin, and C. N. Ironside, "Multiple colliding-pulse mode-locked quantum-well lasers for high repetition rate (up to 375 GHz) short pulse generation," *IET in Towards Terabit Transmission, IEE Colloquium* , , May 1995, pp. 1-6.

[36] A. R. Rae, M. G. Thompson, R. V. Penty, I. H. White, A. R. Kovsh, S. S. Mikhrin, and I. L. Krestnikov, "Harmonic mode-locking of a quantum-dot laser diode," *LEOS 19th Annual Meeting of the IEEE Lasers and Electro-Optics Society.*, Montreal, Oct. 2006, pp. 874-875.

[37] E. U. Rafailov, M. A. Cataluna, W. Sibbett, N. D. Il'inskaya, Y. M. Zadiranov, A. E. Zhukov, V. M. Ustinov, D. A. Livshits, A. R. Kovsh, and N. N. Ledentsov, "High-power picosecond and femtosecond pulse generation from a two-section mode-locked quantum-dot laser," *Appl. Phys. Lett.*, vol. 87, no. 8, pp. 081107, Aug. 2005.

[38] L. Schares, R. Paschotta, L. Occhi, and G. Guekos, "40-GHz mode-locked fiber-ring laser using a Mach-Zehnder interferometer with integrated SOAs," *J. Light. Technol.*, vol. 22, no. 3, pp. 859-873, Mar. 2004.

[39] L. E. Hargrove, R. L. Fork, and M. A. Pollack, "Locking of He-Ne laser modes induced by synchronous intracavity modulation," *Appl. Phys. Lett.*, vol. 5, no. 1, pp. 4-5, 1964.

[40] S. Arahira, and Y. Ogawa, "High-repetition-rate optical pulse generation and control techniques," *Measurement Science and Technology*, vol. 13, no. 11, pp. 1664-1670, 2002.

[41] J. P. Van der Ziel, W. T. Tsang, R. A. Logan, R. M. Mikulyak, and W. M. Augustyniak, "Subpicosecond pulses from passively mode-locked GaAs buried optical guide semiconductor lasers," *Applied Physics Letters*, vol. 39, no. 7, pp. 525-527, 1981.

[42] S. Arahira, Y. Katoh, and Y. Ogawa, "20GHz subpicosecond monolithic modelocked laser diode," *Electronics Letters*, vol. 36, no. 5, pp. 454-456, 2000.

[43] S. Arahira, S. Oshiba, Y. Matsui, T. Kunii, and Y. Ogawa, "Terahertz-rate optical pulse generation from a passively mode-locked semiconductor laser diode," *Optics letters*, vol. 19, no. 11, pp. 834-836, 1994.

[44] U. Keller, "Recent developments in compact ultrafast lasers," *Nature*, vol. 424, no. 6950, pp. 831-838, Aug. 2003.

[45] H. A. Haus, "Modelocking of semiconductor laser diodes," *Jpn. J. Appl. Phys.*, vol. 20, no. 6, pp. 1007–1020, 1981.

[46] R. Arkhipov, A. Pimenov, M. Radziunas, D. Rachinskii, A. G. Vladimirov, D. Arsenijevic, H. Schmeckebier, and D. Bimberg, "Hybrid mode locking in semiconductor lasers: simulations, analysis, and experiments," *IEEE Journal of selected Topics in Quantum Electronics*, vol. 19, no. 4, pp. 1100208, 2013.

[47] M. Kuntz, G. Fiol, M. Laemmlin, C. Meuer, and D. Bimberg, "High-speed mode-locked quantum-dot lasers and optical amplifiers," *Proceedings of the IEEE*, vol. 95, no. 9, pp. 1767-1778, 2007.

[48] M. J. Heck, E. J. Salumbides, A. Renault, E. A. Bente, Y. S. Oei, M. K. Smit, R. Veldhoven, R. Notzel, K. Eikema, and W. Ubachs, "Analysis of hybrid mode-locking of two-section quantum dot lasers operating at 1.5 μm," *Optics express*, vol. 17, no. 20, pp. 18063-18075, 2009.

[49] Yokogawa, Optical spectrum Analyzer, Available http://tmi.yokogawa.com/es/products/optical-measuring-instruments/optical-spectrum-analyzer/.

[50] M. Kroh, " Semiconductor mode-locked laser for high-speed OTDM transmission," PhD thesis, Fakultät IV–Elektrotechnik und Informatik–der, Technischen Universität Berlin, 2006.

[51] Keysight technologies, electrical spectrum analyzer, Available http://www.keysight.com/en/pcx-x2015002/spectrum-analyzers-signal-analyzers?cc=US&lc=eng.

[52] Anritsu MS2668C manual, Available http://www.anritsu.com/en-US/test-measurement/products/MS2668C.

[53] U2T XPDV2120R manual, Available https://www.finisar.com/ sites/default/files/ downloads/ xpdv21x0r _50ghz_photodetector _product_brief_reva1.pdf

[54] U2T XPDV4120R manual, Available https://www.finisar.com/optical-components/xpdv412xr.

[55] Anritsu MA2744A manual, Available http://configure.us.anritsu.com/catalog/i/MA2744A.

[56] Rohde & Schwarz FS-Z110 manual, Available http://www.rohde-schwarz.es/product/fs-z60/-z75/-z90/-z110.html.

[57] Manual by APE GmbH: APE Autocorrelator Pulse Check, July 2001.

[58] K. Sala, G. Kenney-Wallace, and G. Hall, "CW autocorrelation measurements of picosecond laser pulses," *IEEE J. Quantum Electron.*, vol. 16, no. 9, pp. 990–996, 1980.

[59] Nortel FA14UFAC manual, Available http://www.artisantg.com/TestMeasurement/55031 /Nortel_ FA17UFAC_119C28_ Telecom_EDFA.

[60] K. Yvind, "Semiconductor mode-locked lasers for optical communication systems," PhD thesis, Technical University of Denmark, Department of Photonics Engineering, Nanophotonics, 2003.

[61] D. von der Linde, "Characterization of the noise in continuously operating mode-locked lasers," *Appl. Phys., A Mater. Sci. Process.*, vol. 39, pp. 201–217, 1986.

[62] H. C. Bao, and H. F. Liu, "Amplitude Noise of Subharmonically Hybrid Mode-Locked Pulses Generated From a Monolithic Semiconductor Laser". *IEEE photonics technology letters*, vol. 14, no. 1, pp. 6-8, January 2002.

[63] K. Yvind, D. Larsson, L. J. Christiansen, J. Mørk, J. M. Hvam, and J. Hanberg, "High-performance 10GHz all-active monolithic modelocked semiconductor lasers," *Electron. Lett.* vol. 40, no. 12, pp. 735–736, 2004.

[64] G. Carpintero, M. G. Thompson, R. V. Penty, and I. H. White, "Low noise performance of passively mode-locked 10-GHz quantum-dot laser diode," *IEEE Photon. Technol. Lett.*, vol. 21, no. 6, pp. 389–391, March 2009.

[65] G. Raybon, P. B. Hansen, U. Koren, B. I. Miller, M. G. Young, M. Newkirk, P. Iannone, C. Burrus, J. Centanni, and M. Zirngibl, "Two contact, 1 cm long, monolithic extended cavity laser actively mode-locked at 4.4 GHz," *Electronics Letters*, vol. 28, no. 24, pp. 2220-2221, 1992.

[66] P. B. Hansen, G. Raybon, M. D. Chien, U. Koren, B. I. Miller, M. G. Young, J. Verdiell, and C. A. Burrus, "A 1.54-um monolithic semiconductor ring laser: CW and mode-locked operation," *IEEE Photonics Technology Letters*, vol. 4, no. 5, pp. 411-413, 1992.

[67] K. Sato, K. Wakita, I. Kotaka, Y. Kondo, M. Yamamoto, and A. Takada, "Monolithic strained-InGaAsP multiple-quantum-well lasers with integrated electroabsorption modulators for active mode locking," *Applied physics letters*, vol. 65, no. 1, pp. 1-3, 1994.

[68] K. Sato, I. Kotaka, Y. Kondo, and M. Yamamoto, "Active mode locking at 50 GHz repetition frequency by half-frequency modulation of monolithic semiconductor lasers integrated with electroabsorption modulators," *Applied physics letters*, vol. 69, no. 18, pp. 2626-2628, 1996.

[69] S. Latkowski, V. Moskalenko, S. Tahvili, L. Augustin, M. Smit, K. Williams, and E. Bente, "Monolithically integrated 2.5 GHz extended cavity mode-locked ring laser with intracavity phase modulators," *Optics letters*, vol. 40, no. 1, pp. 77-80, 2015.

[70] H. C. Bao, H. F. Liu, and Y. J. Wen, "Amplitude noise of 40-GHz pulses from a subharmonically synchronous mode-locked semiconductor laser," *IEEE Photonics Technology Letters*, vol. 14, no. 4, pp. 540-542, 2002.

[71] T. Nishimura, and Y. Nomura, "Passively mode-locked pulse generation at 40 GHz repetition rate by semiconductor lasers with distributed Bragg reflector for oscillating mode control," *Japanese Journal of Applied Physics*, vol. 42, no. 4S, pp. 2325, 2003.

[72] S. Arahira, Y. Matsui, T. Kunii, S. Oshiba, and Y. Ogawa, "Optical short pulse generation at high repetition rate over 80 GHz from a monolithic passively modelocked DBR laser diode," *Electronics letters*, vol. 29, no. 11, pp. 1013-1015, 1993.

[73] M. Hofmann, S. Bischoff, T. Franck, L. Prip, S. D. Brorson, J. Mork, and K. Fröjdh, "Chirp of monolithic colliding pulse mode-locked diode lasers," *Applied physics letters*, vol. 70, no. 19, pp. 2514-2516, 1997.

[74] M. C. Wu, Y. K. Chen, T. Tanbun-Ek, R. A. Logan, and M. A. Chin, "Tunable monolithic colliding pulse mode-locked quantum-well lasers," *IEEE Photonics Technology Letters*, vol. 3, no. 10, pp. 874-876, 1991.

[75] S. Arahira, and Y. Ogawa, "Transform-limited 480 GHz colliding-pulse modelocked laser diode," *Electronics Letters*, vol. 37, no. 16, pp. 1026-1027, 2001.

[76] P. B. Hansen, G. Raybon, U. Koren, B. I. Miller, M. G. Young, M. A. Newkirk, ... and C. A. Burrus, "Monolithic semiconductor soliton transmitter," *Journal of Lightwave Technology*, vol. 13, no. 2, pp. 297-301, 1995.

[77] I. Ogura, H. Kurita, T. Sasaki, and H. Yokoyama, "Precise operation-frequency control of monolithic mode-locked laser diodes for high-speed optical communication and all-optical signal processing," *Optical and Quantum Electronics*, vol. 33, no. 7-10, pp. 709-725, 2001.

[78] K. Yvind, D. Larsson, L. J. Christiansen, C. S. Angelo, L. K. Oxenløwe, J. Mørk, D. Birkedal, J. Hvam, and J. Hanberg, "Low-jitter and high-power 40 GHz all-active mode-locked lasers," *IEEE Photonics Technology Letters*, vol. 16, no. 4, pp. 975-977 , 2004.

[79] A. Stohr, S. Babiel, P. J. Cannard, B. Charbonnier, F. van Dijk, S. Fedderwitz, D. Moodie, L. Pavlovic, L. Ponnampalam, C. C. Renaud, D. Rogers, V. Rymanov, A. Seeds, A. G. Steffan, A. Umbach, and M. Weiss, "Millimeter-wave photonic components for broadband wireless systems," *IEEE Trans. Microwave Theory Tech.*, vol. 58, no. 11, pp. 3071–3082 , 2010.

[80] R. Neil, "Understanding Jitter and Wander Measurements and Standards," Agilent Technologies, Feb 2003.

[81] I. Aldaya, G. Campuzano, C. Gosset, and G. Castañón, "Phase-insensitive RF envelope detection allows optical heterodyning of MHz-linewidth signals," *IEEE Photon. Technol. Lett.*, vol. 25, no. 22, pp. 2193-2196, 2013.

[82] T. Ishikawa, H. Tanaka, M. Shibata, M. Tajima, Y. Oka, and T. Kaneko, "Narrow Spectral Linewidth Full-Band Wavelength Tunable Lasers for Digital Coherent Communication Systems," *Sei Technical Review*, no. 77, pp. 54-58, 2013.

Chapter 3

On-chip Semiconductor Laser Structures

3.1 Introduction

The main objective of the present work has been to develop monolithically integrated mode-locked laser diodes, to be able to use them within a Photonic Integrated Circuit, combined with additional photonic components to increase the functionality on the chip. The selected approach has been to use the current European Indium Phosphide (InP) Generic Photonic integration technology platforms, in which a standard set of components can be integrated together on a single chip [1]. InP photonic integrated circuits (PICs) have as key advantage enabling the integration of multiple photonic building blocks within a single chip eliminating the need to fiber couple these photonic building blocks, having a huge impact on the cost and component footprint as well as increasing the functionality [2].

This technology platforms use active-passive integration to enable the use of active and passive components, using butt-joint coupling technique, in which the index guiding structure for the passive and active components is at the same height on the chip [3]. The butt-joint coupling technique depicted in Figure 3.1(a), provides a quality of the transition between the active and the passive waveguide structure with -50 dB reflection, which is a minimum value required for good laser operation [4]. Also, the butt-joint coupling technique offers maximum flexibility for the design such as layer thicknesses, layer composition and doping concentrations. The main advantage of the butt-joint coupling technique is the re-grow of a passive film without doping in the index guiding layers which allows achieving much lower losses in passive waveguides than by using, selective area growth [5], quantum well intermixing [6] or multiple vertical waveguide structure technique using evanescent field coupling [7].

The active components are the shallow etched quantum well semiconductor optical amplifier (SOA) and electro-refractive phase modulators (ERM) while the passive components are isolators (ISO), splitters, filters, deep etched and shallow etched passive waveguides (PW) [8]. Figure 3.1(b) shows the five basic components available in the fabrication technology. The samples are fabricated with the current InP photonic generic integration technology by using a library of standardized building blocks (BBs) and the fabrication is carried out by the SMART Photonics InP active-passive integration foundry service within a commercial multi-project wafer (MPW) run [9].

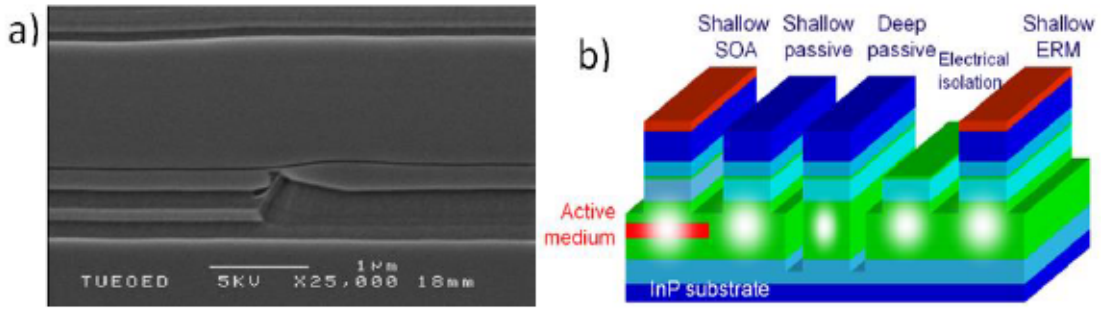

Figure 3.1. a) Scanning Electron Microscope photograph of the butt-joint coupling technique [3]. b) Five components available in the fabrication technology [8].

In order to develop mode-locked structures on-chip, the availability of reflective elements is essential to form the resonator cavity. The most common approach to build monolithic semiconductor lasers has been using the cleaved facets of the semiconductor as reflectors [10]. From the state of the art performed in chapter 2, we have observed that most mode-locked lasers reported to date used cleaved facets in order to achieve mode-locked regimes. Figure 3.2 depicts a monolithic mode-locked structure using cleaved facets to form the resonator cavity. Cleaved facets are relatively easy to obtain by cleaving the semiconductor. However, the main disadvantage of such structures is

that the optical signal is not available on the chip anymore, avoiding the integration on-chip for subsequent photonic signal processing operations within the chip (modulation, optical filtering, pulse rate multiplication and so on) [11]. Also, the cleaving process introduces a ±10μm uncertainty in the resonator cavity length formed by two cleaved facets. As a result, the cleaving process causes the mode spacing to differ between different fabrication runs [12].

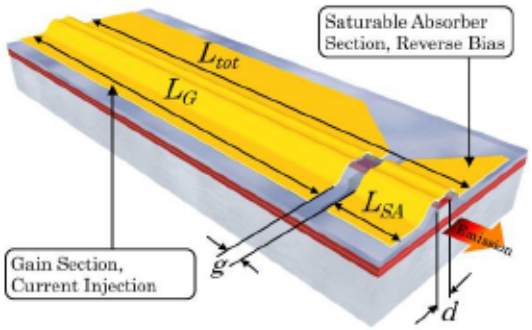

Figure 3.2. Mode-locked laser using cleaved facets [13].

Two main approaches have been proposed to develop mode locked laser resonator structures on-chip, without need for cleaved facets.

The first approach is using ring resonators, which offer the merit of lithographic control of the cavity length. Monolithic passively mode-locked semiconductor ring laser with ring radius of 150 μm capable to emit a continuous train of 1.3 ps transform-limited lasing pulses at higher repetition rate $\Delta f_{rep} = 86$ GHz has been reported [14] and its structure is shown in Figure 3.3(a). Also, the mode-locked semiconductor ring laser allows the directional control of optical power using the relative positioning of the amplifier and absorber within the ring cavity [15]. Figure 3.3(b) depicts the mode-locked semiconductor ring laser with the asymmetric location of the SOA and SA

within the ring cavity for the directional control of the optical power. However, a drawback for ring mode-locked lasers in order to achieve higher repetition rates is the minimum radius allowed in the lithographic process of curved waveguides not lower than 100 μm [11].

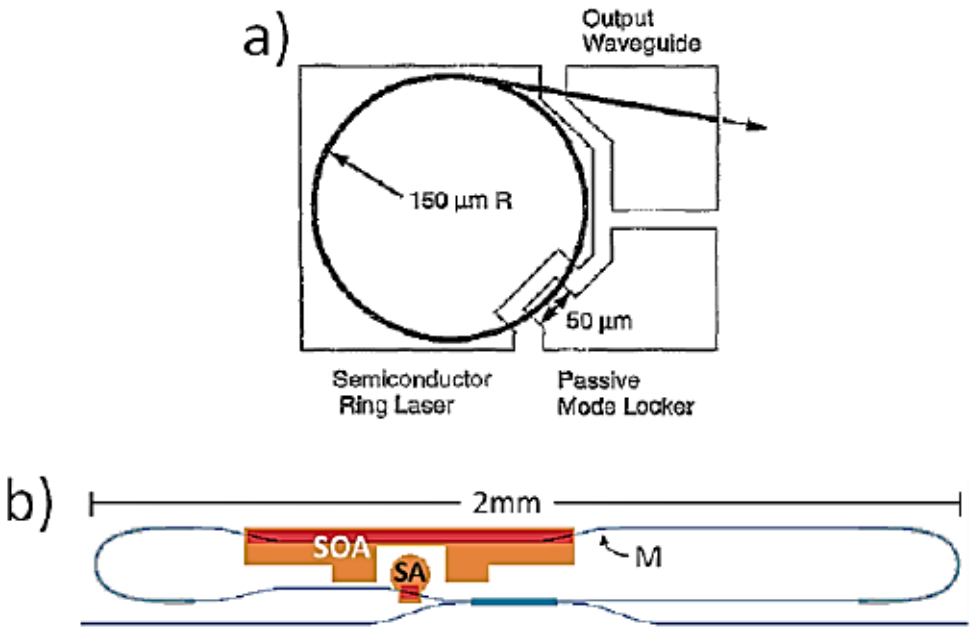

Figure 3.3. Ring mode-locked lasers. a) Higher repetition rate $\Delta f_{rep} = 86$ GHz.[14]. b) Directional control of the optical power [15].

The second approach is to form the Fabry-Perot resonator using a cleaved facet to define the mirror on one end, and a Distributed Bragg Reflector (DBR) to define the mirror on the opposite side [16]. This technique has recently been improved, demonstrating mode-locking when a surface-etched grating is used [17], with simpler fabrication process than the fairly complicated DBR. The main merit of DBR is that they can be located anywhere within the chip so the signal is still available on-chip. But, a significant drawback is that the integration of DBRs with other components imposes restrictions to the fabrication process and requires a very high degree of process control

to obtain the desired reflection/transmission ratio [18]. Figure 3.4 depicts a mode-locked laser structure integrated with DBR.

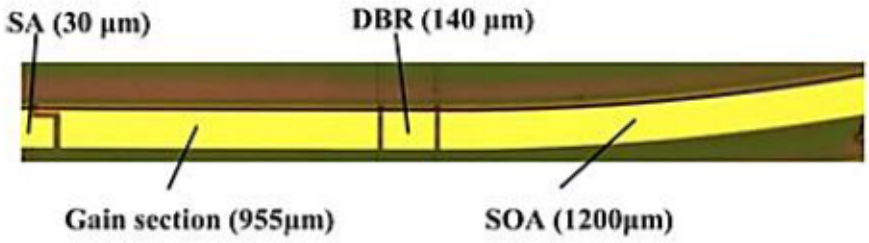

Figure 3.4. Mode-locked laser structure integrated with DBR [17].

Simpler reflector structures can be achieved using standard optical components, such as the Sagnac loop reflectors (SLRs) depicted in Figure 3.5. These are composed of an optical multimode interference (MMI) coupler [19], in which two of its outputs are connected to each other with a loop waveguide [20], [21]. These types of mirror structures have been used in hybrid silicon colliding pulse mode-locked lasers [22] and linear arrayed waveguide grating multi-wavelength lasers [23]. The SLRs are an attractive option for on-chip integration due to avoid restrictions on the on-chip location so the transmitted light is still available on chip. Unfortunately, these structures are usually quite large as at least a 180° bend is needed to connect the splitter outputs [24] and also locally enhanced optical confinement structure is required in the loop waveguide to reduce the minimum bend radius [20].

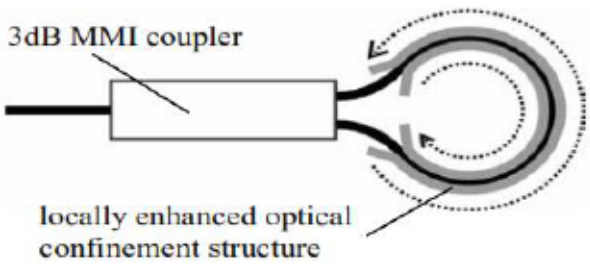

Figure 3.5. Structure of the Sagnac loop reflector [20].

Another approach using the same standard processes of the technology platforms is to employ multi-mode interference reflectors (MIRs), which are novel on-chip mirrors, offering a compact structure which requires only the use of a deep etch fabrication step [25]. Its structure is sketched in Figure 3.6. MIRs have a broadband response and they can therefore be a good candidate to substitute deep-etched DBRs and loop mirrors. MIR typical lengths around 100 µm make them smaller than loop mirrors, but larger than deep DBRs. The merit of MIRs over DBRs is their simpler fabrication process [25]. All the advantages make MIRs a potential option for on-chip integration. As a result, MIR have already been applied in several photonic integrated circuits, so Fabry–Perot laser structures have been recently demonstrated with resonator cavity lengths down to 415 µm [26].

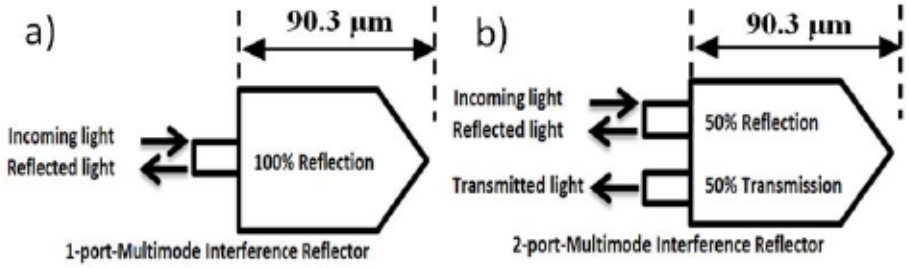

Figure 3.6. Structure of the multi-mode interference reflectors.

The MIR mirror structures derive from a standard multimode interference (MMI) coupler [19], in which deeply etched 45° mirrors at suitable locations reflect back the light by total internal reflection. The length and width of the MIR mirror are 90.3 µm and 6 µm respectively [25]. There are two types of MIRs depending on the number ports in the MMI. One has a single port (1x0 MIR), and is based on a 1x2 MMI coupler to offer a 100% light reflection, it is shown in Figure 3.6(a). An alternate design is

based on a 2x2 MIR coupler, defining the 2x0 MIR reflector depicted in Figure 3.6(b). This option has two access ports, so that the light entering into one of these ports is divided evenly and reflected back to the two ports. This offers a 50% reflection mirror at each output.

3.2 On-chip Fabry–Perot Lasers.

In order to experimentally asses the optical length of the MIR reflectors, we developed on-chip Fabry–Perot laser (oc-FP) structures using MIR reflectors as end facets. Another goal of these devices was to experimentally determine the group refractive index of shallow and deep etched waveguide sections in the laser cavity. The oc-FP lasers were designed as a photonic integrated circuit, using a library of standardized building blocks (BBs) and fabricated within a commercial multi-project wafer (MPW) run available through SMART Photonics InP active-passive integration foundry service [27]. The structure and the microscope photograph of the oc-FP laser is depicted in Figure 3.7(a) and Figure 3.7(b), respectively.

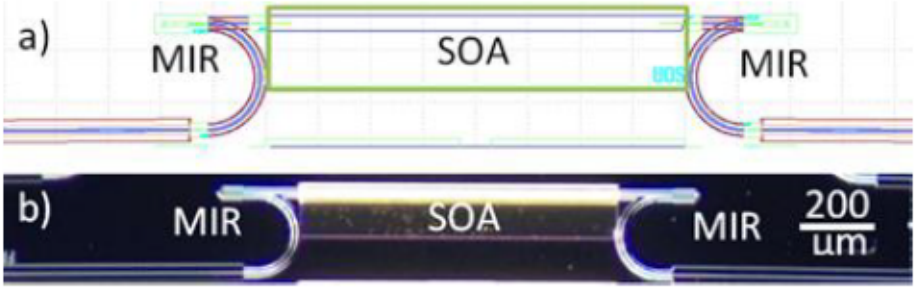

Figure 3.7. On-chip Fabry–Perot laser structures.(a) Structure of the oc-FP. (b) Microscope photograph of the oc-FP.

We developed two oc-FP lasers each having a different active section within but both having the same cavity length. The difference between them was the ratio between the lengths of the deep and shallow etched waveguides. Dev_A with L_{SOA_A} = 800 µm and Dev_B with L_{SOA_B} = 400 µm. The total length of the cavity was established by considering all the building blocks. Mainly, multimode interference reflectors (MIRs), passive waveguides (PWs), Deep2Shallow transition (D2S), Shallow2Deep transition (S2D) and Semiconductor optical amplifier (SOA). Eq. 3.1 describes the total cavity length (L_{cav}) of the oc-FP in function of the building blocks length.

$$Lcav = L_{MIR} + L_{PW} + L_{D2S} + L_{SOA} + L_{S2D} + L_{PW} + L_{MIR} \qquad (3.1)$$

Where:

$$L_{cav} = Cavity\ \ length$$

$$L_{MIR} = Multimode\ interference\ reflector\ \ length$$

$$L_{PW} = Passive\ waveguide\ length$$

$$L_{D2S} = \ \ Deep2Shallow\ transition\ length$$

$$L_{SOA} = \ \ Semiconductor\ optical\ amplifier\ length$$

$$L_{S2D} = \ \ Shallow2Deep\ transition\ length$$

According to previous report of refractive index calculation [3], the Deep2Shallow and Shallow2Deep transition are considered shallow etched, so the shallow length (LS) in the oc-FP is described by Eq. 3.2. Also, Table 3.1 summarizes the lengths of the elements in Dev_A and Dev_B.

$$L_S = L_{D2S} + L_{SOA} + L_{S2D} \qquad (3.2)$$

Building Block Length	Etching	oc-FP Dev_A (μm)	oc-FP Dev_B (μm)
L_{PW}	Deep	168	368
L_{D2S}	Shallow	33	33
L_{SOA}	Shallow	800	400
L_{S2D}	Shallow	33	33
L_{PW}	Deep	168	368
L_S	Shallow	866	466
L_{cav}	-	1202 (error ≈ ±1 μm)	1202 (error ≈ ±1 μm)
L_S/L_{cav}	-	0,720	0,387

Table 3.1. Lengths of the elements in Dev_A and Dev_B.

The unknown parameters are the length of the MIR and the refractive index of the shallow and deep etched waveguide sections. Eq. 3.2 labels the relation between refractive index of the shallow and deep etched waveguide sections and some of the know parameters summarized in Table 3.1. Finally, it is necessary to perform the experimental measurements of the optical spectrum in order to obtain the center wavelength and the optical mode spacing of each oc-FP laser.

$$\frac{L_{optic}}{L_{cav}} = \frac{\lambda_c^2}{2.\Delta\lambda.L_{cav}} = N_D + \frac{L_S}{L_{cav}}.(N_S + N_D) \qquad (3.3)$$

Where: $L_{optic} = Optical\ length$

$\lambda_c = Center\ wavelength$

$\Delta\lambda = Optical\ mode\ spacing\ (nm)$

$L_S = Shallow\ length$

$N_S = Shallow\ group\ refractive\ index$

$N_D = Deep\ group\ refractive\ index$

3.2.1 Experimental Setup

The experimental setup is shown in Figure 3.8, in which the thermoelectric (TEC) control sets the operation temperature at 17 °C. The on-chip Fabry–Perot lasers are mounted on copper carriers, with submounts boards to give electrical access to the pads through bond wires. The light output from the angled facets is collected through lensed fibers with anti-reflection coated tip, spliced to an optical isolator followed by a 90/10 splitter. The 10% output is taken to a power meter and the 90% output either to a Yokogawa AQ6370B optical spectrum analyzer.

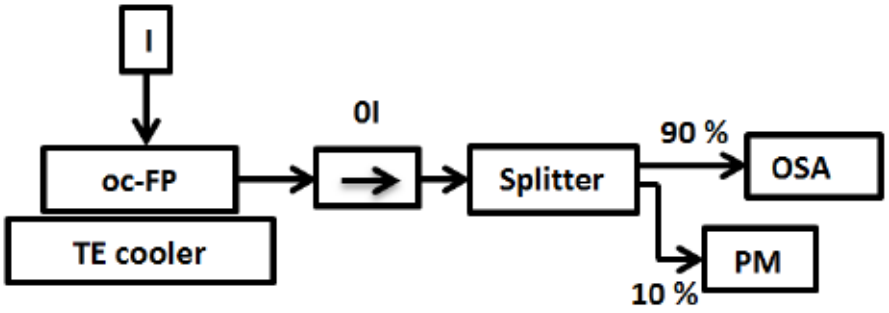

Figure 3.8. Experimental setup for oc-FP characterization. I: Current source, OI: optical isolator, PM: power meter, OSA: optical spectrum analyzer.

3.2.2 Measurement Results

The experimental results provided the optical spectrum of Dev_A and Dev_B sketched in Figure 3.9(a) and Figure 3.9(b), respectively. The gain section of the oc-FP lasers was forward biased at I_{SOA} = 50 mA on both cases. From Figure 3.9(a) we obtain the center wavelength λc = 1548 nm and the optical mode spacing of Dev_A $\Delta\lambda$ = 0.268 nm while From Figure 3.9(b) we obtain the center wavelength λc = 1550 nm and the optical mode spacing of Dev_A $\Delta\lambda$ = 0.272 nm.

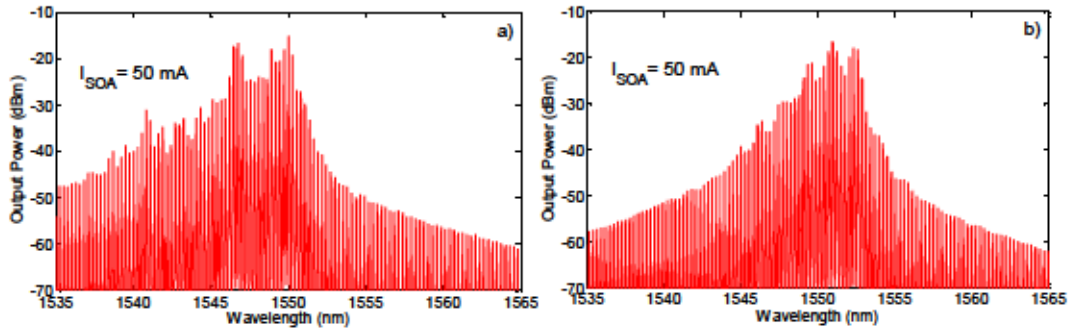

Figure 3.9. Optical Spectrum of the on-chip Fabry–Perot lasers, resolution 0.02 nm. (a) oc-FP Dev_A. (b) oc-FP Dev_B.

Then, considering Eq. 3.3 we are able to obtain an equation for each oc-FP. As a result, Eq. 3.4 and Eq. 3.5 correspond to Dev_A and Dev_B, respectively.

$$L_{optic\_A}/L_{cav\_A} = N_D + L_{S\_A}/L_{cav\_A}(N_S - N_D) \qquad (3.4)$$

$$L_{optic\_B}/L_{cav\_B} = N_D + L_{S\_B}/L_{cav\_B}(N_S - N_D) \qquad (3.5)$$

The relation L_{optic_A}/L_{cav_A} is obtained from the optical spectrum measured for each oc-FP.

$$\frac{L_{optic}}{L_{cav}} = \frac{\lambda_c^2}{2.\Delta\lambda.L_{cav}}$$

$$\frac{L_{optic_A}}{L_{cav_A}} = \frac{\lambda_c^2}{2.\Delta\lambda.L_{cav}} = \frac{1548}{2*0.268*1202} = 3.717 + \Delta\left(\frac{L_{optic_A}}{L_{cav_A}}\right)$$

$$\frac{L_{optic_B}}{L_{cav_B}} = \frac{\lambda_c^2}{2.\Delta\lambda.L_{cav}} = \frac{1550}{2*0.268*1202} = 3.672 + \Delta\left(\frac{L_{optic_B}}{L_{cav_B}}\right)$$

In order to provide precision in the group refractive index calculation, we include the error parameters (uncertainties) $\Delta\left(\frac{L_{optic_A}}{L_{cav_A}}\right)$ and $\Delta\left(\frac{L_{optic_B}}{L_{cav_B}}\right)$ which allow obtaining the refractive index with its corresponding uncertainty. Then, replacing the relations L_{optic_A}/L_{cav_A} and L_{optic_B}/L_{cav_B} with the required values from Table 3.1 in Eq. 3.4

and Eq. 3.5, we have two equations with two unknowns. So we have to solve a system of two equations with two unknowns which are the deep group refractive index and the shallow group refractive index.

$$3.717 = N_D + 0.387\,(N_S - N_D) \qquad (3.4)$$

$$3.672 = N_D + 0.720(N_S - N_D) \qquad (3.5)$$

From the equation system, we obtain the best values of the deep group refractive index and the shallow group refractive index with error $\pm\Delta N_S$ and $\pm\Delta N_D$, respectively. The shallow and deep group refractive indexes are shown in Table 3.2.

Group refractive index	Value
N_S (Shallow)	3.634 $\pm\Delta N_S$
N_D (deep)	3.770 $\pm\Delta N_D$

Table 3.2. Shallow and deep group refractive indexes.

3.2.3 Error Analysis

Next, we perform the error analysis in order to estimate the measurement error of the deep group refractive index and the shallow group refractive index. Fractional uncertainties give us an indication how reliable our experiment is [28]. For this reason, fractional uncertainties are included in order to estimate the error of the measurement.

Considering, Eq. 3.4 for Laser A:

$$\frac{L_{optic_A}}{L_{cav_A}} = \frac{\lambda_c^2}{2.\Delta\lambda.L_{cav}}$$
$$\frac{L_{optic_A}}{L_{cav_A}} = \frac{\lambda_c\,.\,\lambda_c}{2.\Delta\lambda.L_{cav}}$$

Adding fractional uncertainties, we have:

$$\left|\frac{\Delta\left(\frac{L_{optic_A}}{L_{cav_A}}\right)}{\frac{L_{optic_A}}{L_{cav_A}}}\right| = \frac{1}{2}\left[\left|\frac{\Delta\lambda_c}{\lambda_c}\right| + \left|\frac{\Delta\lambda_c}{\lambda_c}\right| + \left|\frac{\Delta(\Delta\lambda)}{\Delta\lambda}\right| + \left|\frac{\Delta L_{cav}}{L_{cav}}\right|\right] \quad (3.6)$$

OSA resolution = 0.02 nm, then OSA error = 0.04 nm. Length resolution = 1 um, then length error = 2 um. In Eq. 3.6, replacing errors and values from Table 3.1:

$$\left|\frac{\Delta\left(\frac{L_{optic_A}}{L_{cav_A}}\right)}{\frac{L_{optic_A}}{L_{cav_A}}}\right| = \frac{1}{2}\left[\left|\frac{0.04}{1548}\right| + \left|\frac{0.04}{1548}\right| + \left|\frac{0.04}{0.268}\right| + \left|\frac{2}{1202}\right|\right]$$

The error when measuring Laser A:

$$\left|\frac{\Delta\left(\frac{L_{optic_A}}{L_{cav_A}}\right)}{\frac{L_{optic_A}}{L_{cav_A}}}\right| = 0.075$$

Considering, Eq. 3.5 for Laser B:

$$\frac{L_{optic_B}}{L_{cav_B}} = \frac{\lambda_c^2}{2.\Delta\lambda.L_{cav}}$$
$$\frac{L_{optic_B}}{L_{cav_B}} = \frac{\lambda_c.\lambda_c}{2.\Delta\lambda.L_{cav}}$$

Adding fractional uncertainties, we have:

$$\left|\frac{\Delta\left(\frac{L_{optic_B}}{L_{cav_B}}\right)}{\frac{L_{optic_B}}{L_{cav_B}}}\right| = \frac{1}{2}\left[\left|\frac{\Delta\lambda_c}{\lambda_c}\right| + \left|\frac{\Delta\lambda_c}{\lambda_c}\right| + \left|\frac{\Delta(\Delta\lambda)}{\Delta\lambda}\right| + \left|\frac{\Delta L_{cav}}{L_{cav}}\right|\right] \quad (3.7)$$

OSA resolution = 0.02 nm, then OSA error = 0.04 nm. Length resolution = 1 um, then length error = 2 um. In Eq. 3.7, replacing errors and values from Table 3.1:

$$\left|\frac{\Delta\left(\frac{L_{optic_B}}{L_{cav_B}}\right)}{\frac{L_{optic_B}}{L_{cav_B}}}\right| = \frac{1}{2}\left[\left|\frac{0.04}{1550}\right| + \left|\frac{0.04}{1550}\right| + \left|\frac{0.04}{0.272}\right| + \left|\frac{2}{1202}\right|\right]$$

The error when measuring Laser B:

$$\left|\frac{\Delta\left(\frac{L_{optic_B}}{L_{cav_B}}\right)}{\frac{L_{optic_B}}{L_{cav_B}}}\right| = 0.074$$

Then, considering the principle that all errors are added, we have the error $\Delta(L_{optic}/L_{cav})$.

$$\left|\frac{\Delta\left(\frac{L_{optic}}{L_{cav}}\right)}{\frac{L_{optic}}{L_{cav}}}\right| = \left|\frac{\Delta\left(\frac{L_{optic_A}}{L_{cav_A}}\right)}{\frac{L_{optic_A}}{L_{cav_A}}}\right| + \left|\frac{\Delta\left(\frac{L_{optic_B}}{L_{cav_B}}\right)}{\frac{L_{optic_B}}{L_{cav_B}}}\right| = 0.149$$

3.2.4 Obtaining the Group Refractive Index Error

Considering, Eq. 3.3.

$$\frac{L_{optic}}{L_{cav}} = N_D + \frac{L_S}{L_{cav}}(N_S + N_D)$$

As, $N_S \approx N_D$, we reduce the Eq.3.3 and obtain:

$$\frac{L_{optic}}{L_{cav}} = N_D + 2N_D\frac{L_S}{L_{cav}}$$

Adding fractional uncertainties, we have:

$$\left|\frac{\Delta\frac{L_{optic}}{L_{cav}}}{\frac{L_{optic}}{L_{cav}}}\right| = \left|\frac{\Delta N_D}{N_D}\right| + 2\left|\frac{\Delta N_D}{N_D}\right| + \left|\frac{\Delta L_S}{L_S}\right| + \left|\frac{\Delta L_{cav}}{L_{cav}}\right|$$

$$3\left|\frac{\Delta N_D}{N_D}\right| = \left|\frac{\Delta\frac{L_{optic}}{L_{cav}}}{\frac{L_{optic}}{L_{cav}}}\right| + \left|\frac{\Delta L_S}{L_S}\right| + \left|\frac{\Delta L_{cav}}{L_{cav}}\right| \quad (3.8)$$

In Eq. 3.8, replacing error $\Delta(L_{optic}/L_{cav})$ and values from Table 3.1 for the worst condition (more error). Length resolution = 1 um, then length error = 2 um.

$$3\left|\frac{\Delta N_D}{N_D}\right| = 0.149 + \left|\frac{2}{466}\right| + \left|\frac{2}{1202}\right|$$

$$\left|\frac{\Delta N_D}{N_D}\right| = 0.052$$

Finally, the error for the group refractive indexes is estimated $\Delta N \pm 0.052$ and they are shown in Table 3.3.

Group refractive index	Value
N_S (Shallow)	3.634 ± 0.052
N_D (deep)	3.770 ± 0.052

Table 3.3. Shallow and deep group refractive indexes with error analysis.

Finally, it was possible to establish the physical length of the multimode interference reflectors using the obtained group refractive indexes. The physical length of MIR (L_{MIR} = 90.3 μm) with the uncertainty is shown in Table 3.4.

Building Block	Physical Length
MIR	90.3 ± 1.0 μm

Table 3.4. Physical length of MIR.

3.3 On-chip Self-Colliding Pulse Mode-Locked Lasers

In this section, we demonstrate the experimental characterization results of novel on-chip self-colliding pulse mode-locked laser diode (oc-sCPM), which employs multimode interference reflectors to eliminate the need of cleaved facet mirrors to form

the resonator cavity [29]. The result is an oc-sCPM that does not require cleaved facets to operate, enabling us to locate this oc-sCPM at any location within the photonic chip. This oc-sCPM provides a simple source of optical pulses that can be inserted within a (PIC) chip for subsequent photonic signal processing operations within the chip.

On the active area, based on shallow etched multi-quantum-well active layer, the waveguide includes a SOA for optical gain and the SA. In the passive area we define the MIR reflectors and the output waveguides. These elements belong to the building block library of the InP technology platform. From these building blocks we designed the oc-sCPM with the length of the resonator (L_{cav} = 2480 µm) defined by the MIR reflectors. In our design the saturable absorber, was located at one of the extremes of the gain section (locating it at $L_{cav}/4$ from the right hand side MIR), as shown in Figure 3.10.

The device was fabricated, using 2-port MIR on both ends, the output waveguide direct the light out of the chip for analysis. In order to reduce back-reflections from the edges to a minimum, the output waveguides were angled 7° to the chip edge and anti-reflection (AR) coating was used at the facets. The active section length in the oc-sCPM is fixed to 800 µm, using 780 µm for the SOA and 20 µm for the SA. The SA, as shown in Figure 3.10 (b), is on the right end of the active waveguide. This location was intended to be 620 µm away from the right hand side MIR reflector, to place the SA at $L_{cav}/4$ and set the device operation at its fourth harmonic (72 GHz) [30]. But, due to the fact that the SA is located at one extreme, the self-colliding structure was achieved and the mode-locked regime at the fundamental repetition rate was obtained in the experimental results [31]. The microscope photograph of the fabricated sample is depicted in Figure 3.10 (b)

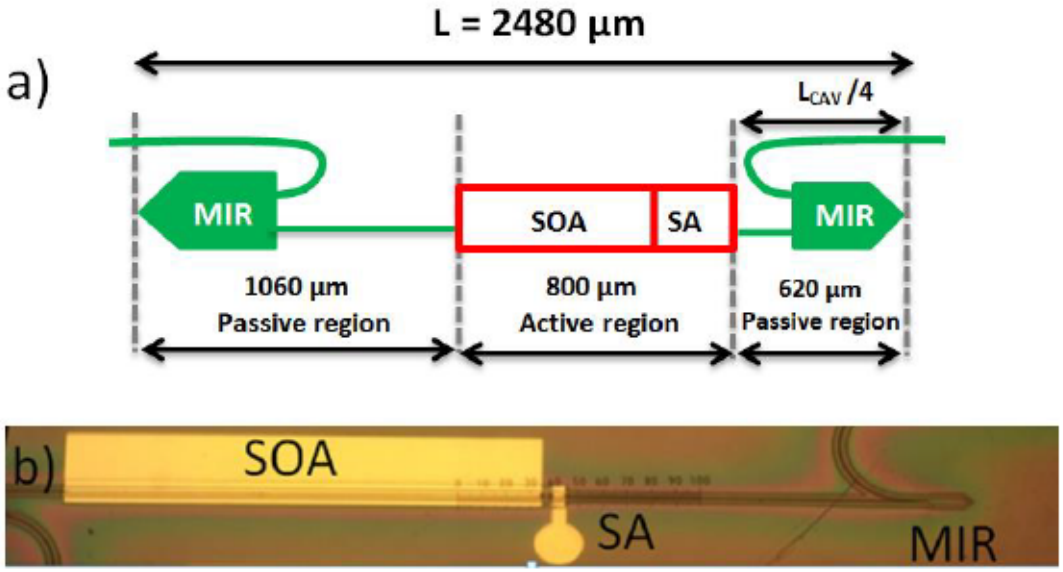

Figure 3.10. On-chip self-colliding pulse mode-locked laser. a) Structure. b) Microscope photograph.

3.3.1 Experimental Setup

Figure 3.11 depicts the experimental setup for oc-sCPM characterization. The thermoelectric (TEC) control sets the operation temperature at 17 °C. The oc-sCPM is mounted on copper carriers, with submounts boards to give electrical access to the pads through bond wires. The light output from the angled facets is collected through a lensed. Then spliced to an optical isolator followed by a 90/10 splitter. The 10% output is taken to a power meter and the 90% output either to a Yokogawa AQ6370B optical spectrum analyzer, to a high speed photodiode connected to an electrical spectrum analyzer or an optical auto-correlator.

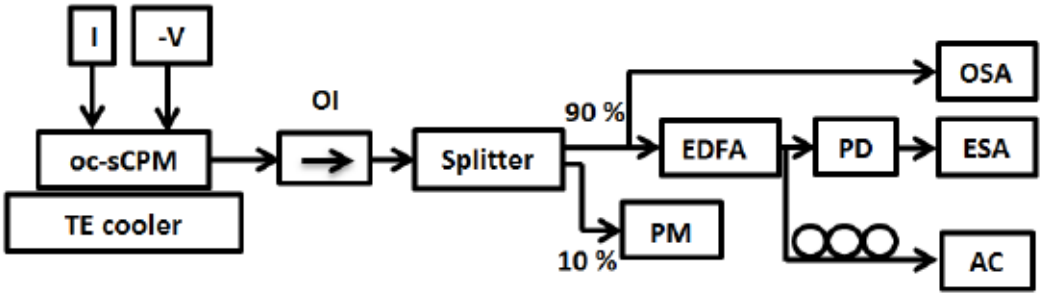

Figure 3.11. Experimental setup for oc-sCPM characterization. I: Current source, -V: reverse bias voltage, OI: optical isolator, EDFA: erbium doped fiber amplifier, PM: power meter, OSA: optical spectrum analyzer, ESA: electrical spectrum analyzer, PD: photodiode, PC: polarization controller, AC: autocorrelator.

3.3.2 Measurement Results

The optical power versus input current characteristic (L-I curve) is shown in Figure 3.12(a), traced when the input current is swept for a fixed SA reverse voltage (V_{SA} = -2.5 V). The threshold current is found to be 38 mA. As the current is swept to measure the optical power, the optical spectra map is measured simultaneously, shown in Figure 3.12(b).

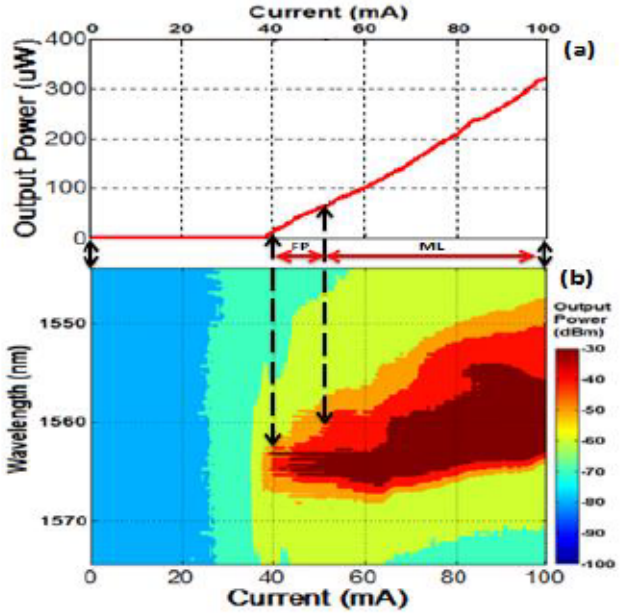

Figure 3.12. (a) Optical power versus current (L-I curve). Regions, FP: fabry-perot, ML: mode locked. (b) Optical spectra map.

From these two plots, we observe that the device presents different modes of operation. Close to threshold, the device operates as a Fabry-Perot laser, exhibiting lasing on several modes. Above a current level (50 mA), the device enters into a mode locked state. A detailed view of the optical spectrum in the mode-locked state is shown in Figure 3.13, when the bias conditions are I_{SOA} = 90 mA and V_{SA} = -2.5 V. The center wavelength is located around 1558 nm, and the inset shows a mode spacing of 16.7 GHz (0.134 nm). This evidences that the device is not working at the intended harmonic frequency but at its fundamental (16.7 GHz), different from the designed target, revealing the uncertainty at the design stage of establishing the optical length of the MIR. This uncertainty has an impact on the location of the SA for colliding pulse mode locking, and we have reached mode locking at the fundamental frequency. However, using this frequency we are able to establish that the optical length of the

resonator is 2480 µm, from which the optical length of the MIR can be confirmed to be 90.3 µm for future designs.

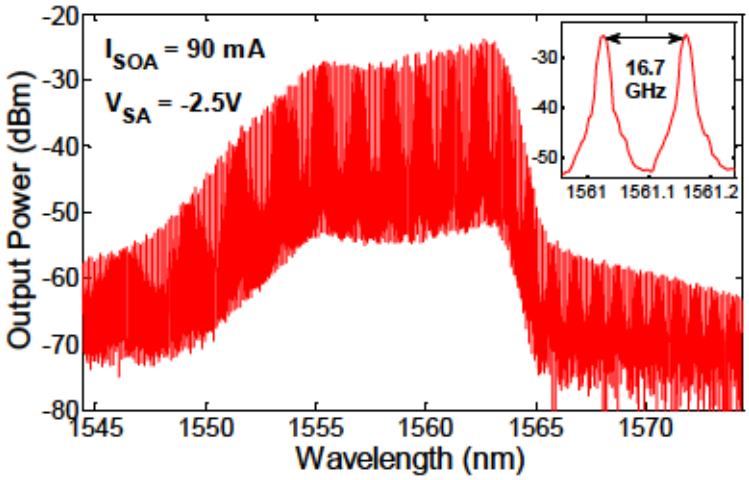

Figure 3.13. Optical spectrum of the oc-sCPM in the mode-lock state. Central wavelength 1558 nm, span 30 nm. The inset shows the frequency mode spacing, the resolution is 0.02 nm.

Following this analysis, the optical signal output was injected into a XPDV2020R U2T high speed photodiode with 40 GHz bandwidth to convert into an RF signal, measuring the electrical spectrum using an Anritsu MS2668C Electrical Spectrum Analyzer. We observe the position and power of the repetition frequency, shown in Figure 3.14 for the same conditions in which the optical spectrum was shown, I_{SOA} = 90 mA and V_{SA} = -2.5 V. In accordance with the frequency spacing of the optical modes, the fundamental frequency appears at frep ~ 16.7 GHz, 47 dB over the noise floor. The linewidth of the beating RF spectrum fitted to a Lorentzian line-shape at full width half maximum (FWHM) is 91.90 kHz.

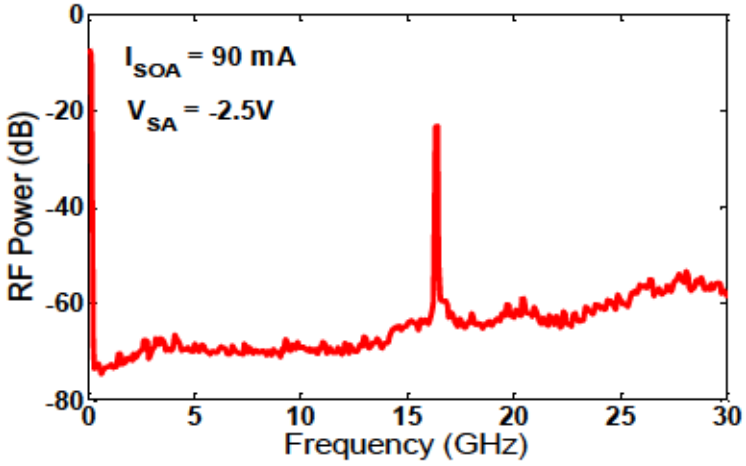

Figure 3.14. Electrical spectrum of the oc-sCPM. Center frequency, 15 GHz, Span 30 GHz, Resolution Bandwidth (RBW) = 1 MHz, Video Bandwidth (VBW) = 1 MHz.

The existence of optical pulses is demonstrated using an intensity autocorrelation measurement, with an APE Pulse-Check auto-correlator. The pulse widths have been measured for varying current injection levels into the SOA (I_{SOA}) and reverse voltages on the SA (V_{SA}), showing the measured data in Figure 3.15(a) and Figure 3.15(b) respectively. We observe the same trends as in other mode-locked structures in which pulses broaden with increasing injection current, usually attributed to self-phase modulation (SPM), and shorten with increasing absorber reverse voltage, when the absorber recovery time is shortest [32], [33]. The shortest pulse-width that has been measured is 1.72 ps with -2.5 V reverse bias to the absorber and 50 mA to the gain section (current level needed for the onset of mode-locking). In order to provide a detail of the pulse shape, Figure 3.15(c) presents the autocorrelator output for the bias conditions in which we have shown the optical and electrical spectrums, I_{SOA} = 90 mA and V_{SA} = -2.5 V. The measured trace has its best fit using a Gaussian pulse shape, from which we obtain that the pulse width is 2.92 ps. Further, this allows us to calculate the

Time Bandwidth Product (TBP), obtaining 0.49, closed to the Fourier transform limited Gaussian pulse (0.4413) [34].

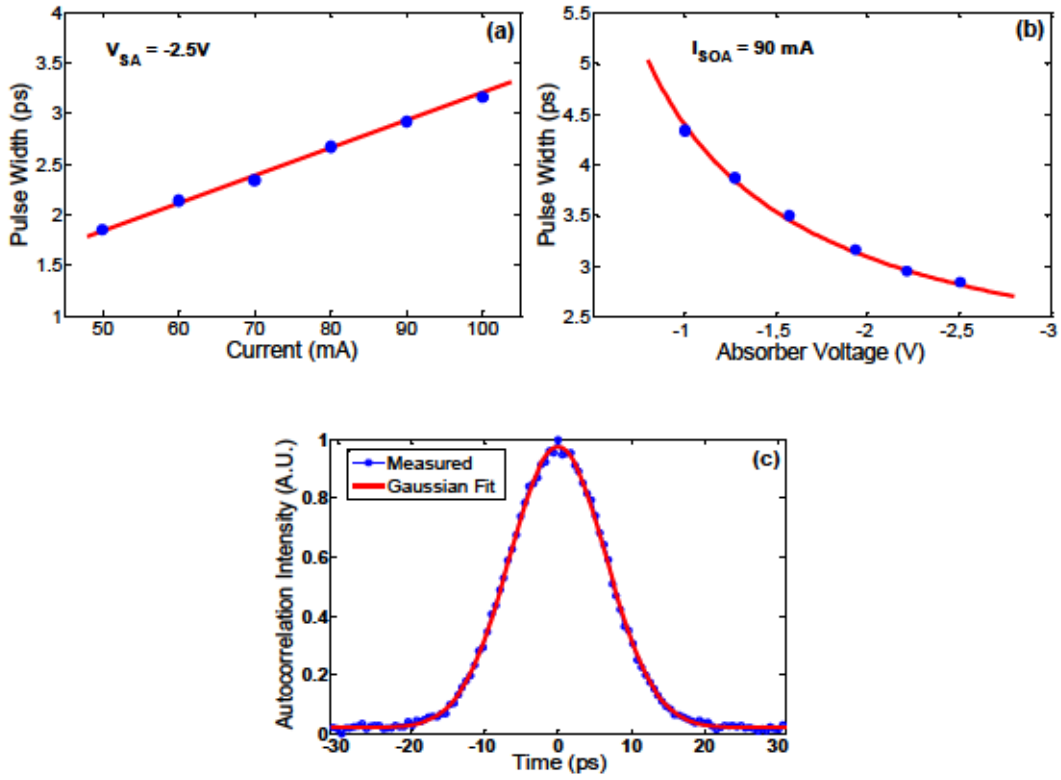

Figure 3.15. (a) Pulse width versus gain section current level at fixed V_{SA}, (b) Pulse width versus reverse absorber voltage at fixed I_{SOA} , and (c) Measured optical pulse shape (blue, line marked with circles) fitted to a Gaussian lineshape (red, continuous line).

Figure 3.16 shows the map of the mode-locked regimes of the oc-sCPM working at 16.7 GHz. The stable self-colliding pulse mode-locked operation was achieved for a wide range of bias conditions when the forward bias current in the SOA sections are ranging from 51 mA to 100 mA and the reverse bias voltage in the absorber section varying within a – 1.5 V to – 2.8 V range which is depicted by the red area in Figure 3.16. At the same time, the degradable, deteriorated, poor, unstable and no existence of self-colliding pulse mode-locked regime is denoted by the white areas. The no lasing regime lower than the threshold current at 38 mA is depicted by the yellow area and the

continuous wave regime is denoted by the black area when the forward bias current in the SOA sections are ranging from threshold current to 50 mA and the reverse bias absorber section varying in the whole range within a 0 V to – 3 V.

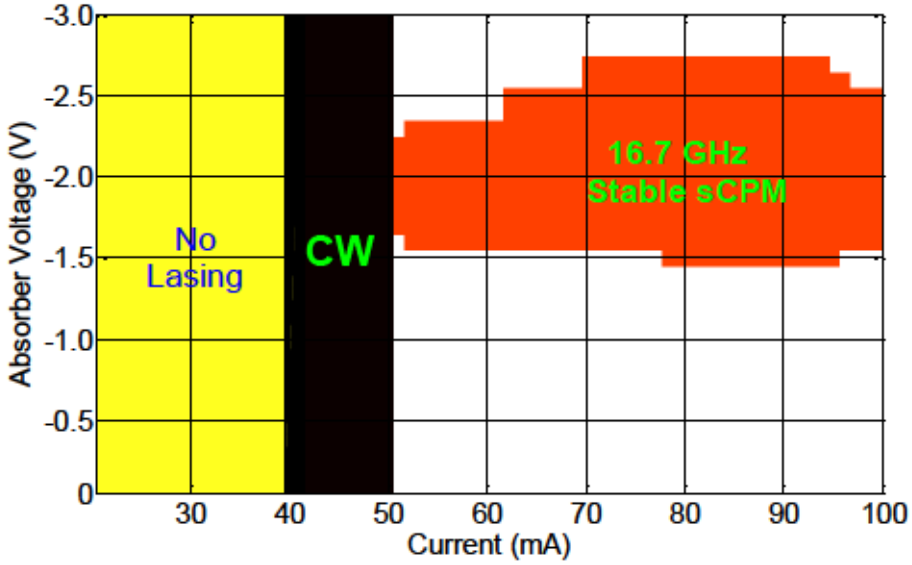

Figure 3.16. Measured map of the self-colliding pulse mode-locked regime as a function of forward bias current and the reverse bias voltage.

3.4 Conclusions

- There are different options to integrate mode-locked lasers on chip, among them MIR reflectors are the good candidates to substitute deep-etched DBRs and loop mirrors. The merit of MIRs over DBRs is their ease fabrication process and the high fabrication tolerances with respect to the length and width of the device.
- The experimental measurements of on-chip Fabry–Perot lasers allow establishing experimentally the length of MIR reflectors and the group refractive index of shallow and deep etched waveguide sections in the laser cavity.
- We report for the first time, to the best of our knowledge a novel fully integrated on-chip mode-locked laser diode using multimode interference reflectors. The device has been shown to operate at the fundamental repetition rate, from the optical and RF spectrum measurements.

3.5 References

[1] K. A. Williams, E. A. J. M. Bente, D. Heiss, Y. Jiao, K. Lawniczuk, X. J. M. Leijtens and M. K. Smit, "InP photonic circuits using generic integration", *Photon. Res.*, vol. 3, no. 5, pp. B60-B68, Oct. 2015.

[2] M. Smit, X. Leijtens, E. Bente, J. Van der Tol, H. Ambrosius, D. Robbins, M. Wale, N. Grote, and M. Schell, "Generic foundry model for InP-based photonics ICs," *IET Optoelectron.*, vol. 5, no. 5, pp. 187–194, 2011.

[3] Y. Barbarin, "1.55 μm Integrated Mode locked Semiconductor Lasers", Ph. D. thesis, Dept. Elect. Eng., Technical University of Eindhoven (TU/e), Eindhoven, The Netherlands, 2007.

[4] R.W. Tkach and A.R. Chraplyvy, "Regimes of feedback effects in 1.5 um distributed feedback lasers", *Journal Lightwave Technology*, vol. 4, pp. 1655-1661, 1986.

[5] N. Futakuchi, X. Song, D. Miyashita, M. Kato, Y. Nakano, "Fabrication of InGaAsP/InP Mach-Zehnder interferometer optical amplifier switches by metalorganic vapor phase selective area epitaxy," *in Proc. IEEE IPRM*, pp. 583-586, 2001.

[6] E.J. Skogen, J.S. Barton, S.P. Denbaars, L.A. Coldren, "A quantum-well-intermixing process for wavelength-agile photonic integrated circuits", *IEEE Journal of Selected Topics in Quantum Electronics*, vol. 8, no. 4, pp. 863- 869, 2002.

[7] L. XU, M. R. Gokhale, P. Studenkov, J. C. Dries, C.P. Chao, D. Garbuzov, and S. R. Forrest, "Monolithic Integration of an InGaAsP-InP MQW LaserNaveguide Using a Twin-Guide Structure with a Mode Selection Layer," *IEEE Journal Photonics Technology Letters*, vol. 9, no. 5, pp. 369-371, 1997.

[8] E. Bente, V. Moskalenko, S. Latkowski, S. Tahvili, L. Augustin and M. Smit, "Monolithically integrated InP based modelocked ring laser systems", *In SPIE Photonics Europe International Society for Optics and Photonics,* vol. 9134, pp. 91340C-91340C, 2014.

[9] K. A. Williams, E. A. J. M. Bente, D. Heiss, Y. Jiao, K. Lawniczuk, X. J. M. Leijtens and M. K. Smit, "InP photonic circuits using generic integration", *Photon. Res.*, vol. 3, no. 5, pp. B60-B68, Oct. 2015.

[10] M. Ettenberg, "A new dielectric facet reflector for semiconductor lasers,"*Applied Physics Letters*, vol. 32, no. 11, pp. 724–725, 1978.

[11] E. Kleijn. "Passive components in indium phosphide generic integration technologies," Ph. D. thesis, Dept. Elect. Eng., Technical University of Eindhoven (TU/e), Eindhoven, the Netherlands, 2014.

[12] D. Larsson. "Fabrication and characterization of low-noise monolithic mode-locked lasers," Ph. D. thesis, Dept. Photon. Eng., Technical University of Denmark (DTU), Kongens Lyngby, Denmark, pp. 26, 2006.

[13] V. V. Pusino, M. J. Strain, and M. Sorel, "Passive mode-locking in semiconductor lasers with saturable absorbers bandgap shifted through quantum well intermixing," *Photonics Research*, vol. 2, no. 6, pp. 186-189, 2014.

[14] J. P. Hohimer, and G. A. Vawter, "Passive mode locking of monolithic semiconductor ring lasers at 86 GHz," *Appl. Phys. Lett.* vol. 63, no. 12, pp. 1598-1600, 1993.

[15] M. S. Tahvili, Y. Barbarin, X. J. Leijtens, T. de Vries, E. Smalbrugge, J. Bolk, H. P. Ambrosius, M. K. Smit, and E. A. Bente, "Directional control of optical power in integrated InP/InGaAsP extended cavity mode-locked ring lasers," *Opt. Lett.* vol. 36, no. 13, pp. 2462-2464, 2011.

[16] S. Joshi, N. Chimot, R. Rosales, S. Barbet, A. Accard, A. Ramdane, and F. Lelarge, "Mode-locked InAs/InP quantum dash based DBR laser monolithically integrated with a semiconductor optical amplifier," *in 25th International Conference on Indium Phosphide and Related Materials (IPRM)*, 2013, pp. 1-2.

[17] L. Hou, M. Haji, and J. H. Marsh, "Monolithic mode-locked laser with an integrated optical amplifier for low-noise and high-power operation," *IEEE J. Sel. Top. Quantum Electron.*, vol. 19, no. 4, pp. 1100808, 2013.

[18] B. Docter, E. Geluk, M. Sander-Jochem, F. Karouta, and M. Smit, "Deep etched DBR gratings in InP for photonic integrated circuits," *IPRM '07. IEEE 19th International Conference in Indium Phosphide and Related Materials*, 2007, pp. 226–228.

[19] L. Soldano, and E. Pennings, "Optical multi-mode interference devices based on self-imaging: principles and applications," *J. Lightwave Technol.*, vol. 13, no. 4, pp. 615-627, 1995.

[20] Y. Ikuma, M. Yasumoto, D. Miyamoto, J. Ito, and H. Tsuda, "Small helical reflective arrayed-waveguide grating with integrated loop mirrors," *33rd European Conference and Exhibition of Optical Communication (ECOC)*, September 2007, pp. 1–2.

[21] L. Xu, X. Leijtens, P. Urban, E. Smalbrugge, T. de Vries, Y. Oei, R. Nötzel, H. de Waardt, and M. Smit, "Novel reflective SOA with MMI-loop mirror based on semi-insulating InP," *in Proceedings of the 13th Annual Symposium of the IEEE Photonics Benelux Chapter*. Enschede, The Netherlands, November 2008, pp. 43–46.

[22] Srinivasan, E. Norberg, T. Komljenovic, M. Davenport, G. Fish, and J. E. Bowers, "Hybrid Silicon Colliding-Pulse Mode-Locked Lasers With On-Chip Stabilization," *IEEE J. Sel. Top. Quantum Electron.*, vol. 21, no. 6, pp. 24-29, Nov./Dic. 2015.

[23] P. Muñoz, R. García-Olcina, C. Habib, L. R. Chen, X. J. M. Leijtens, T. de Vries, D. Robbins, and J. Capmany, "Label swapper device for spectral amplitude coded optical packet networks monolithically integrated on InP," *Opt. Express*, vol. 19, no. 14, pp. 13540-13550, 2011.

[24] W. Yuan, C. Seibert, and D. Hall, "Single-facet teardrop laser with matched-bends design," *Journal of Selected Topics in Quantum Electronics*, vol. 17, no. 6, pp. 1662–1669, November 2011.

[25] E. Kleijn, M. K. Smit, and X. J. M. Leijtens, "Multimode interference reflectors: A new class of components for photonic integrated circuits," *J. Lightwave Technol.*, vol. 31, no. 18, pp. 3055-3063, 2013.

[26] J. Zhao, E. Kleijn, P. J. Williams, M. K. Smit, and X. J. M. Leijtens, "On-chip laser with multimode interference reflectors realized in a generic integration platform," *in Compound Semiconductor Week (CSW/IPRM), and 23rd International Conference on Indium Phosphide and Related Materials,* Berlin, Germany, pp. 1–4, 2011.

[27] The pure play InP Photonics foundry, "SMART Photonics", http://www.smartphotonics.nl/.

[28] J. R. Taylor, "An Introduction to Error Analysis," California: *University Science Books, Mill Valley*, 1982.

[29] C. Gordón, R. Guzmán, X. Leijtens, and G. Carpintero, "On-chip mode-locked laser diode structure using multimode interference reflectors," *Photonics Res.,* vol. 3, no. 1, pp. 15-18, 2015.

[30] J. F. Martins-Filho, S. D. McDougall, E. A. Avrutin, and C. N. Ironside, "Multiple colliding-pulse mode-locked quantum-well lasers for high repetition rate (up to 375 GHz) short pulse generation. IET in Towards Terabit Transmission," *IEE Colloquium*, pp. 16-1, May 1995.

[31] D. J. Jones, L. M. Zhang, J. E. Carroll, and D. D. Marcenac, "Dynamics of monolithic passively mode-locked semiconductor lasers," *IEEE Journal of Quantum Electronics*, vol. 31, no. 6, pp. 1051-1058, 1995.

[32] K. A. Williams, M. G. Thompson, and I. H. White, "Long-wavelength monolithic mode-locked diode lasers," *New J. Phys. A,* vol. 6, no. 179, pp. 1 – 31, 2004.

[33] K. Merghem, A. Akrout, A. Martinez, G. Moreau, P. Tourrenc, F. Lelarge, F Van Dijk, H. Duan, G. Aubin, and A. Ramdane, "Short pulse generation using a passively mode locked single InGaAsP/InP quantum well laser," *Optics express*, vol. 16, no. 14, pp. 10675-10683, 2008.

[34] K. Sala, G. Kenney-Wallace, and G. Hall, "CW autocorrelation measurements of picosecond laser pulses," *IEEE J. Quantum Electron*., vol. 16, no. 9, pp. 990-996, 1980.

Chapter 4

On-chip Colliding Pulse Mode-Locked Lasers

4.1 Introduction

Colliding pulse mode-locked laser diodes (CPM) are well known sources of ultrafast and ultra-short optical pulses [1], which have been shown to produce Fourier-transform-limited optical pulses with 0.52 to 1.28 ps pulse durations, repetition rates within the range 40 GHz to 500 GHz [2]. CPM laser structures offer shorter pulses and increased repetition rates compared to Q-switching and gain switching structures [3]. The main characteristic of the CPM structure is to locate the saturable absorber (SA) at the center of the optical resonator, which enhances the saturation of the absorber from the fact that it actually results in two counter-propagating pulses coexisting in the cavity, which reach simultaneously the SA. Figure 4.1 sketches the structure of the colliding pulse mode locked laser.

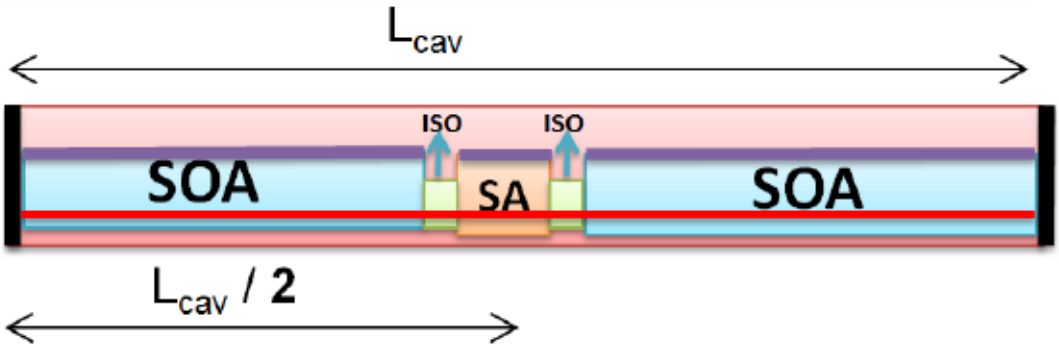

Figure 4.1. Structure of the colliding pulse mode-locked laser.

The simplicity of their structure allows CPM structures to be implemented in a photonic integrated circuit (PIC) [4], which would allow developing compact system around it, adding functionalities [5]. PIC technology improves circuit-level performance by removing assembly complexity and variability. This technology also enables sustained increases in the functionality, and reliability of circuits, while reducing their

size, power, and cost [6]. Some previous examples where the benefits of on-chip integration bring to mode-locked laser diodes are the combination of different mode-locked sources for wavelength division multiplexing (WDM) [7], or an increase of the optical pulse average power including a tapered semiconductor optical amplifier at the output [8]. However, the common approach for mode locked laser diodes, defining the resonator using the cleaved facet mirrors, rules out photonic integration [9], [10].

4.2 On-Chip Colliding Pulse Mode-Locked Laser Structure

We have developed an on-chip colliding pulse mode-locked (oc-CPM) laser structure with an extended cavity configuration, using MIR reflectors to define the resonator on-chip. The saturable absorber (SA) is easily located at the center of the cavity, designing the resonator to be symmetrical on both sides of the SA. Therefore, the precision with which the SA is positioned at the center depends on the lithographic process tolerances, down to the nanometer range and the wafer uniformity which is typically good.

The structure of the oc-CPM is shown Figure 4.2. The saturable absorber (SA) is located at the center of the resonator cavity, then defining the structure symmetrically from each side of the SA. The first element to include is the optical gain, using a semiconductor optical amplifier (SOA) component. On each side of the SA, SOAs of equal length are placed. The SOA is then followed by an active-passive transition and a passive waveguide. This waveguide, which is necessary to connect the SOA to the multimode interference reflectors (MIR), allows us to control the cavity length, and therefore, the repetition rate. The shorter this waveguide is, the shorter the cavity and

the higher the repetition rate. On each side, a 2x0 MIR reflector defines the resonator and provides optical output. We have used the same type of MIR reflector on both ends in order to ensure symmetry around the SA, as this is a critical aspect in CPM to ensure the best quality for the generated optical pulses [1].

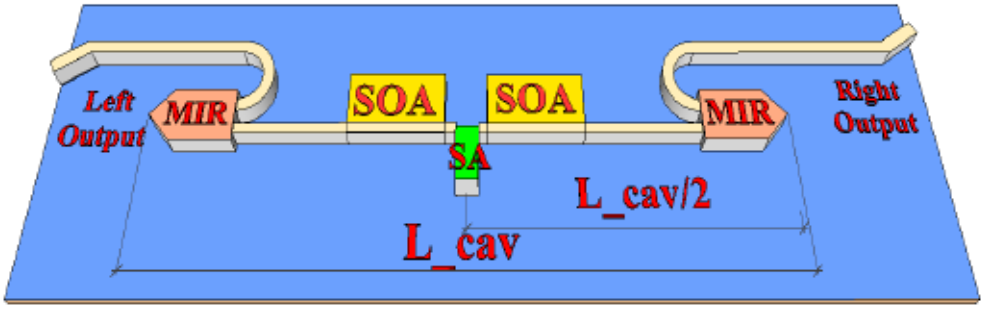

Figure 4.2. Schematic of the structure On-chip colliding mode locked lasers based on multimode interference reflectors.

4.3 Design of the On-Chip Colliding Pulse Mode-Locked Laser Structure

One of the most important aspects in the CPM structure design is to establish the saturable absorber length, trying to optimize it with respect to the length of the gain section. In order to enhance the structure, we carried out a comparison between simulation results and experimental data.

We developed four oc-CPMs with extended cavity linear laser configuration. The fundamental repetition was 25 GHz, which the colliding regime turns into 50 GHz. The only parameter which changes is the saturable absorber length while maintaining the total gain section the same. The selected absorber lengths for the study were 50 um, 40 um, 30 um and 20 um which are typical lengths reported in theoretical and experimental reports of colliding pulse mode-locked lasers [1], [11]. These samples were also

fabricated through SMART Photonics InP active-passive integration foundry service [12].

A microscope photograph of device samples is shown in Figure 4.3, where the SA contacts are visible at the center of the cavity with their respective length. The different elements in the resonator are clearly visible, showing the symmetry around the SA. The four colliding pulse mode-locked laser structures were designed with the same cavity length. All of them have the same active region length, fixed to 1000 µm. The lengths of the two SOAs add up to 930, 940, 950, 960 µm, separated by the 50, 40, 30, 20 µm SA at the center respectively. In each case two 20 um isolators at both sides of the SA are located. Table 4.1 summarizes the features of all devices developed in the MPW run, with the component lengths, fundamental frequency (FF) which is the repetition rate $\left(\Delta f_{rep} = {}^{c}/_{2nL_{cav}}\right)$ and second harmonic frequency (SHF) which is the expected colliding pulse mode locked repetition rate.

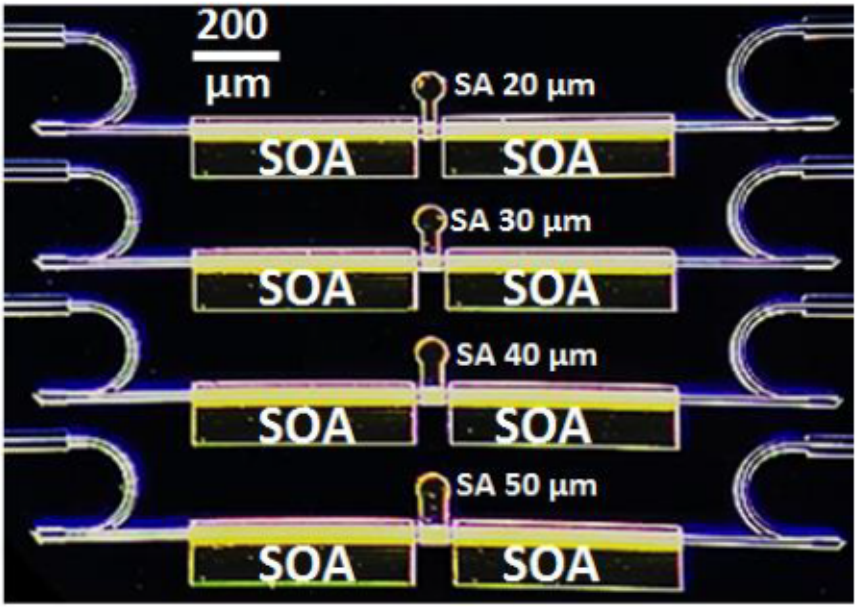

Figure 4.3. Microscope photograph of different devices, with different saturable absorber lengths.

Components Length (um)						
Devices	*MIR*	*SOA*	*SA*	*ISO*	*PW*	L_{cav}
Dev_SA50	90.3	455	50	20	451.4	1632
Dev_SA40	90.3	460	40	20	451.4	1632
Dev_SA30	90.3	465	30	20	451.4	1632
Dev_SA20	90.3	470	20	20	451.4	1632

Table 4.1. Features of devices fabricated for the Saturable Absorber Length Optimization.

The four colliding pulse mode-locked laser structures were designed considering the rules provided by previous reports [1], [11], [13]. The design rules provide the design criteria for the optimized design of mode locked semiconductor lasers which meet the pulse source requirements for communications systems [14]. The essential rules are related to the length of the saturable absorber and the relation between the gain and absorber section lengths.

- **Rule 1**: the length of the saturable absorber related to the total cavity length (L_{SA}/L_{cav}) ranging from 1% to 5 % provides stable mode locked regimes [1], [11].
- **Rule 2**: the relation between the gain and absorber section lengths (L_{SOA}/L_{SA}) from 10 to 20 times allows reaching stable mode locked regimes [1], [13].

A recent study experimentally demonstrated a mode-locked laser diode with an extremely long ring cavity capable to generate 2.5 GHz repetition rate [15]. The design rule 1 was not satisfied because of the 50 µm saturable absorber length used in the device provided a relation $L_{SA}/L_{cav} < 1\%$ due to the long cavity length configuration, while the design rule 2 is satisfied with the relation $L_{SOA}/L_{SA} \approx 15$ times. This

recommends that the most critical rule that needs to be satisfied is the design rule 2, in order to obtain stable mode-locked regimes.

Table 4.2 shows the design rules and the result of its application in the design stage of the four samples.

Design Criteria	Dev_SA50	Dev_SA40	Dev_SA30	Dev_SA20
Rule 1 : L_{SA}/L_{cav} **1% to 5 %**	50/1632 ≈ 3 %	40/1632 ≈ 2.45 %	30/1632 ≈ 1.84 %	20/1632 ≈ 1.23 %
Rule 2 : L_{SOA}/L_{SA} **10 to 20**	455/50 ≈ 10	460/40 ≈ 12	465/30 ≈ 16	470/20 ≈ 24
Result	The design meets the criteria	The design meets the criteria	The design meets the criteria	Close to the limit of Rule 2. (It was done with the intention to study the mode-locked regimes)

Table 4.2. Design rules and the result of its application.

4.3.1 Simulation Stage

The simulation of the oc-CPM was carried out by using the FreeTWM (Travelling Wave Model) software. FreeTWM is free software designed for the study of the dynamics of multi-section semiconductor lasers based on the traveling wave approach of Maxwell Bloch equations [16]. Active-passive coupled sections can be modeled by using this free software. The program is implemented as an ensemble of functions to be used from within Octave or Matlab. The FreeTWM software allows reproducing the dynamics of semiconductor lasers which we will use to fit our experimental results qualitatively.

There are several key parameters that affect the dynamics and the mode-locked properties of semiconductor Fabry–Perot lasers with intracavity saturable absorber such

us the influence of the saturable absorber length, recovery time of the saturable absorber, intraband relaxation time, and gain/absorber relative frequency shift, which have been theoretically studied with the FreeTWM software [13]. In the present work, we have studied as key parameter, the influence of the saturable absorber length section.

The structure of mode-locked laser is composed of different sections within the mode locked laser cavity such as gain (SOA), absorber (SA), and passive (PW) sections. Figure 4.4 depicts the different sections considered in the FreeTWM.

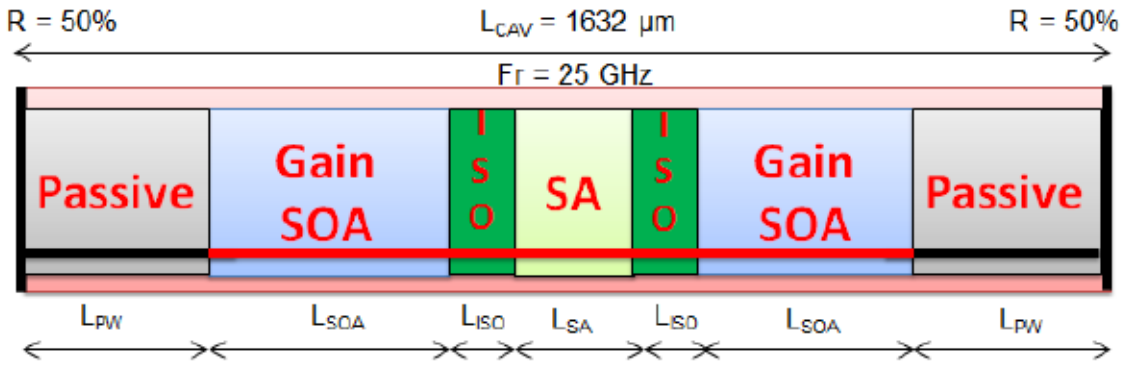

Figure 4.4. Structure of the oc-CPM used by the FreeTWM.

Also, it is necessary to set the material parameters for each section. The waveguide parameters are well known for semiconductor InP waveguides with the emission wavelength at 1.55 µm. The facet reflectivity is 0.50 provided by the two ports MIR reflectors and the single trip time in the cavity is 12.5 ps which correspond to 25 GHz fundamental repetition rate linear cavity mode-locked laser.

The parameters for the gain section such as the internal losses, saturated gain factor, polarization decay rate, and the transparency carrier density have been confirmed by gain measurements of a InGaAsP/InP quantum well based gain section. While the

recombination coefficients A, B, C correspond to the InGaAsP/InP material [17] and the rest of parameters have been obtained from previous theoretically studies [11].

The absorber section works in the regime of slow saturation, so the absorber recovery time of the saturable absorber must be taken longer than the pulse duration and shorter than the round trip time. The absorber recovery time used in the simulation has 10 ps and the bandgap offset is 5 THz. Also, the parameters for the passive section are set to zero (0) due to the fact that there are not saturated gain factor, non radiative recombination, spontaneous recombination and Auger recombination. All the parameters required by the FreeTWM software for the different sections are summarized in Table 4.3.

Meaning	Symbol	Value	Units
Waveguide Parameters			
Emission wavelength	λo	1.55	μm
Group refractive index	n_g	3.57	
Transparency Carrier Density	N_t	$1x10^{18}$	cm^{-3}
Group Velocity	$v_g = \frac{c}{ng}$	$0.84x10^8$	m/s
Left facet reflectivity	R_r	0.5	_
Right facet reflectivity	R_l	0.5	_
Single trip time in the cavity	τ_g	12.5	ps
Gain Section Parameters			
Internal losses	$2\alpha_i$	14.4	cm^{-1}
Saturated gain factor	$2\chi_o$	424	cm^{-1}
Intraband relaxation time	τ_k	125	fs
Bandgap offset	Ωg	0	THz
Empty band contribution	Ω_T	90	THz
Transparency current	J_t	$8.1x10^8$	cm^3s^{-1}
Non radiative recombination	A	$1x10^8$	s^{-1}
Spontaneous recombination	B	$7x10^{-10}$	cm^3s^{-1}
Auger recombination	C	$1x10^{-29}$	cm^6s^{-1}
Ambipolar diffusion coefficient	$\mathcal{D}$	12	cm^2s^{-1}
Spontaneous emission rate	β	$3x10^{-3}$	-
Absorber Section Parameters			
Bandgap offset	Ωg	5	THz
Non radiative recombination	A	$1/10x10^{-12}$	s^{-1}
Absorber recovery time	τ_{SA}	10	ps

Table 4.3. Table of parameters used by FreeTWM [17].

The FreeTWM software provides the profiles for the optical power, electric field intensity and carriers concentration against a discretized length, obtained after 500 single trips in the cavity. The discretized length is directly related to the cavity length in micrometers, so 1632 um in the cavity length correspond to 1632 points in the discretization. The blue and red lines in Figure 4.5(a) represent the forward and the backward waves, respectively.

We clearly observe the intensities and fields of the two optical pulses coexisting within the cavity which are depicted Figure 4.5(a) and Figure 4.5(b). Also, it is clearly observable the amount of carriers concentrated in SOA sections which are depicted in Figure 4.5(c).

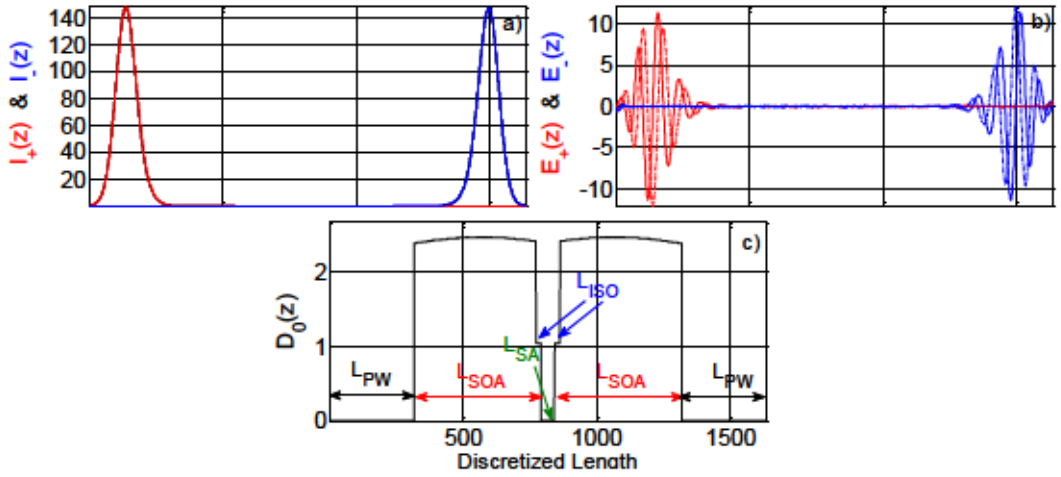

Figure 4.5. Profiles of Dev_SA 50, delivered by FreeTWM. (a) Optical Power, (b) Electrical field Intensity, and (c) Carriers concentration.

4.3.2 Experimental Setup

The setup that we have used to characterize the chip is sketched in Figure 4.6. The device is mounted on a copper chuck that was temperature stabilized to 16 °C. The

electrical access was provided through DC needle probes. The current into the two SOA sections was supplied from a single ILX 3724B laser diode controller, while the reverse bias into the SA was provided by an Agilent E3631A voltage source. The optical output from the angled facet of the oc-CPM was collected using anti-reflection coated lensed fibers, including an optical isolator (OI). This element was followed by a 90/10 splitter which divided the light in two branches. The 10% branch is connected to a Newport 842-PE power meter (PM), providing a constant measure of the generated optical power. The other branch, with 90% split, is used to characterize the device using different instruments. The optical characterization includes a Yokogawa AQ6370B optical spectrum analyzer (OSA), to observe the optical spectrum. Also, after being amplified on a Nortel FA14UFAC telecom erbium doped fiber amplifier (EDFA), an APE pulse-check auto-correlator (AC) to measure the pulse autocorrelation. For the electrical characterization of the RF beat signal we used a 90 GHz -3-dB bandwidth U2T XPDV4120R photodiode (PD) to perform the optoelectronic conversion. Depending on the frequency range, we have external mixers which down-convert the signal frequency. We have used the mixer from Anritsu, MA2744A (50 GHz - 75 GHz).

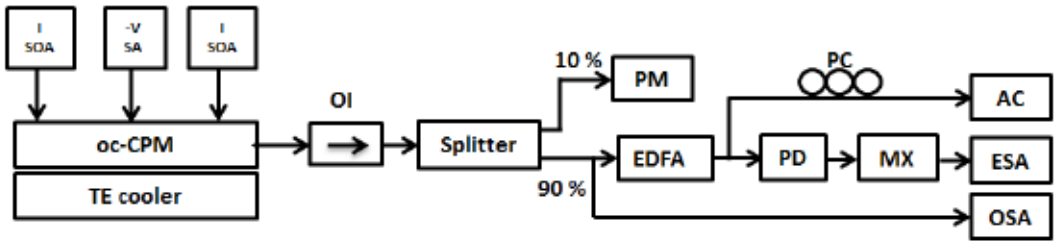

Figure 4.6. Structure of the oc-CPM used by the FreeTWM. Experimental setup. I: Current source, -V: reverse bias voltage, TE cooler: thermoelectric cooler, OI: optical isolator, PM: power meter, EDFA: erbium doped fiber amplifier, PC: polarization controller, AC: autocorrelator, PD: photodiode, MX: mixer, ESA: electrical spectrum analyzer, OSA: optical spectrum analyzer.

4.3.3 Simulation vs. Experimental Results of Saturable Absorber Length Optimization

The characterization in detail of the colliding pulse mode-locked regime was carried out at a bias setting which exhibits a colliding pulse mode-locked regime. For the experimental results the gain section was forward bias at I_{SOA} = 64 mA which is double of the threshold current and SA reverse biased V_{SA} = -2.2 V. Similarly, for the simulation results the bias setting was at injected carrier rate $J_{(ZJ)SOA} = 120.e^{8}s^{-1}$ which is also double of the threshold current rate obtained from the FreeTWM, and the absorber section works in the regime of slow saturation so the absorber recovery time is $\tau_{SA} =$ 10 ps. We will refer to these bias settings as colliding pulse bias settings for all the samples developed in the saturable absorber length optimization. Once the simulation and experimental processes have been carried out, we present the results for each laser with different length of the SA.

50 µm Saturable Absorber, CPM

The optical spectrum log scale of the Dev_SA50 in the simulation and experimental stages at CPB settings are shown in Figure 4.7(a) and Figure 4.7(b) respectively. The agreement between the simulation and experimental is evaluated in terms of shape, optical mode spacing, and the side mode suppression ratio. As a result, the simulation and experimental results have common features, Gaussian shape around peak, the inset in each picture shows the optical mode spacing of 25 GHz and twice this frequency 50 GHz due to the colliding pulse mode locking condition. Also, the side mode suppression ratio is around 35 dBm in each case. But, the spectral bandwidth of the experimental

optical spectrum is narrow than the simulated optical spectrum. The estimated spectral width of the simulated optical spectrum of Dev_SA50 is $\Delta v_s = 370$ GHz while for the measured optical spectrum is $\Delta v_m = 325$ GHz obtained from the Gaussian fitting of both results. Further analysis is now needed varying the parameters in the model to identify the processes giving rise to the differences.

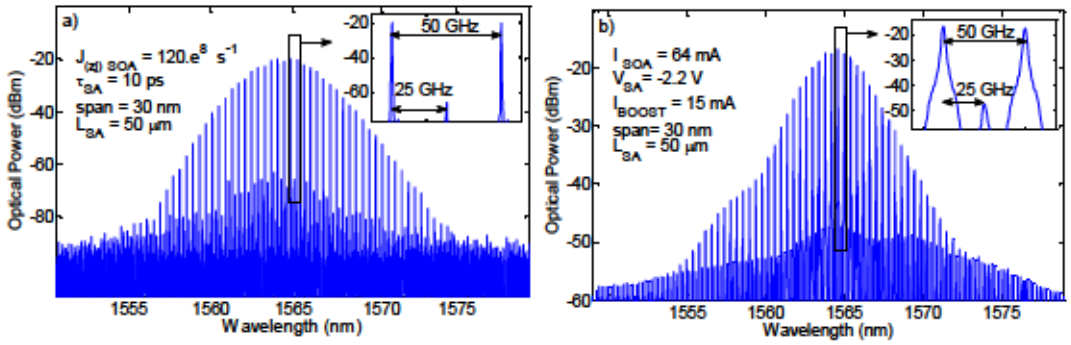

Figure 4.7. Optical Spectrum Dev_SA50. (a) Simulation. (b) Experimental, OSA trace.

The quality of the optical pulse train is evaluated in terms of the repetition rate frequency, pulse shape, and pulse width. In this case, the optical pulse train allows evaluating the repetition rate frequency. The simulation and experimental results of the optical pulse train of the Dev_SA50 in a period of 50 ps is depicted in Figure 4.8(a) and Figure 4.8(b), respectively. The agreement is in terms of repetition rate at 50 GHz which corresponds to a 20 ps time between pulses and the stable pulse train without any amplitude variation. But, in the experimental result obtained from the autocorrelator it is appreciable the noise at the background level while the simulation result does not have this kind of background level.

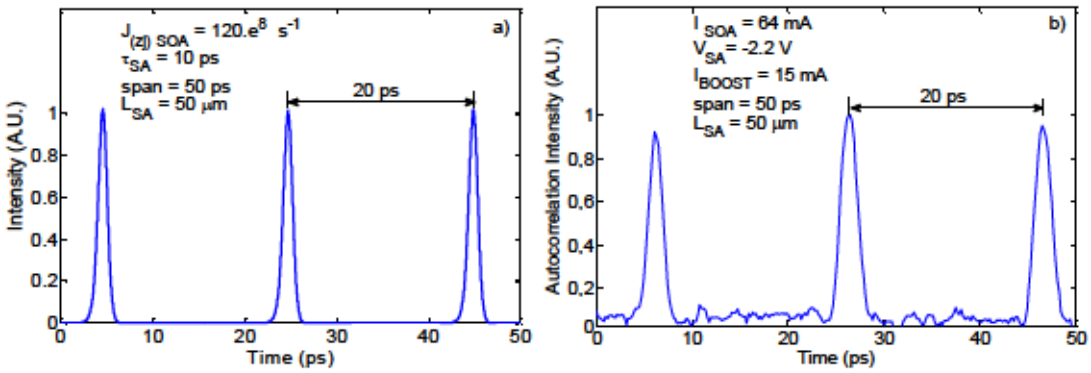

Figure 4.8. Optical pulse characterization Dev_SA50. (a) Simulated pulse train. (b) Experimental autocorrelation trace.

The quality of the optical pulses in terms of pulse shape and pulse width is evaluated in a 15 ps span by Figure 4.9(a) and Figure 4.9(b) which depict the optical pulse of the simulation and experimental results, respectively. The pulse width of $\Delta\tau_s = 1.3$ ps and $\Delta\tau_m = 1.5$ ps were estimated by a deconvolution of the Gaussian pulse shape fitting and the time bandwidth product obtained was $TBP_s = 0.48$ and $TBP_m = 0.49$, close to the Fourier transform limit Gaussian pulses for simulation and experimental results, respectively.

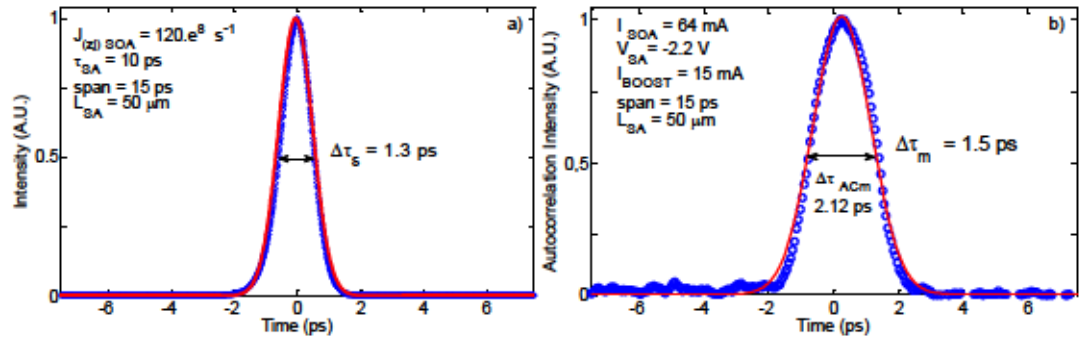

Figure 4.9. Pulse width Dev_SA50. (a) Simulation. (b) Experimental autocorrelation trace.

40 µm Saturable Absorber, CPM

The simulation and experimental results of the optical spectrum of the Dev_SA40 are shown in Figure 4.10(a) and Figure 4.10(b), respectively. The 40 um length of the saturable absorber in the Dev_SA40 simulation and experimental results have common features, Gaussian shape around peak, the inset in each picture shows the optical mode spacing of 25 GHz and double this frequency 50 GHz due to the colliding pulse mode locking condition with the side mode suppression ratio around 25 dBm in each case. But, in the experimental result there is lack of symmetry in the blue region of the optical spectrum. The estimated spectral width of the simulated optical spectrum is $\Delta v_s = 350$ GHz while for the measured optical spectrum is $\Delta v_m = 360$ GHz obtained from the Gaussian fitting of both results of Dev_SA40.

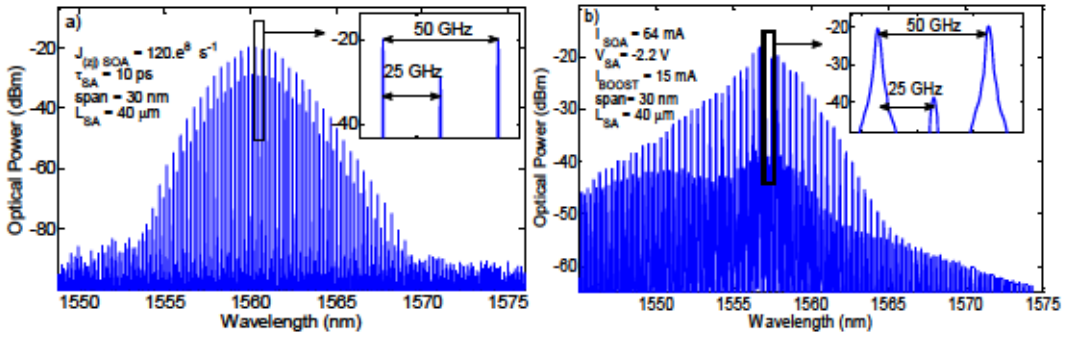

Figure 4.10. Optical Spectrum Dev_SA40. (a) Simulation. (b) Experimental, OSA trace.

The optical pulse train of Dev_SA40 from the simulation and experimental results are depicted in Figure 4.11(a) and Figure 4.11(b), respectively. In the period of 50 ps, we observe three pulses in agreement in terms of repetition rate at 50 GHz for both results. But, in the experimental AC signal we observe the background noise and the slight variation of the amplitude of the pulse train.

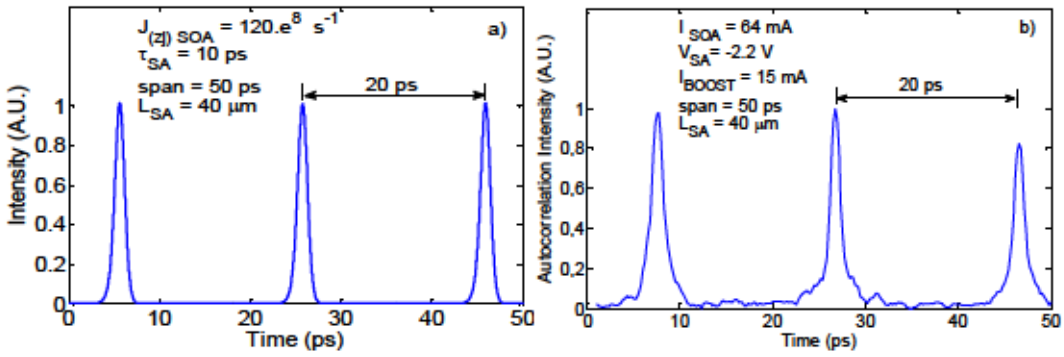

Figure 4.11. Optical pulse characterization Dev_SA40. (a) Simulated pulse train. (b) Experimental autocorrelation trace.

The hyperbolic secant pulse shape was used for the estimation of the pulse width obtained from the simulation and experimental results which are depicted in Figure 4.12(a) and Figure 4.12(b), respectively. The deconvolution of the hyperbolic secant pulse shape fitting provided the pulse width of $\Delta\tau_s$ = 1.2 ps and the time bandwidth product TBP_s = 0.42 from the simulations results while a pulse width of $\Delta\tau_m$ = 1.22 ps and TBP_m = 0.44 were obtained from the experimental measurement results. Also, close to the Fourier transform limit, hyperbolic secant pulses for both cases were obtained.

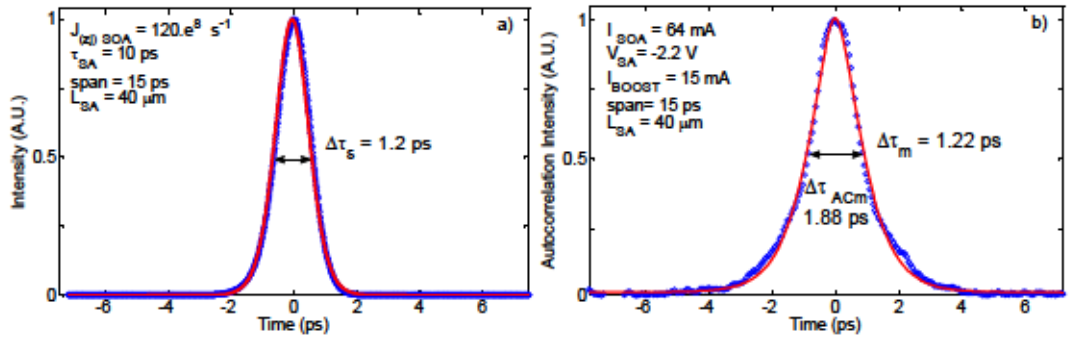

Figure 4.12. Pulse width Dev_SA40. (a) Simulation. (b) Experimental autocorrelation trace.

30 µm Saturable Absorber, CPM

Figure 4.13(a) and Figure 4.13(b) depict the optical spectrum of Dev_SA30 from the simulation and experimental results at 30 nm span, respectively. The comparison between simulation and experimental results reveals the agreement in the Gaussian shape around peak, the inset in each picture shows the optical mode spacing of 25 GHz and twice this frequency 50 GHz due to the colliding pulse mode locking condition with the reduction of the side mode suppression to around 20 dBm in the optical spectrum. Also, the spectral bandwidth of the simulated optical spectrum is narrower than the experimental optical spectrum. The estimated spectral width of the simulated optical spectrum is $\Delta v_s = 360$ GHz while for the measured optical spectrum is $\Delta v_m = 410$ GHz obtained from the Gaussian fitting of both results of Dev_SA30.

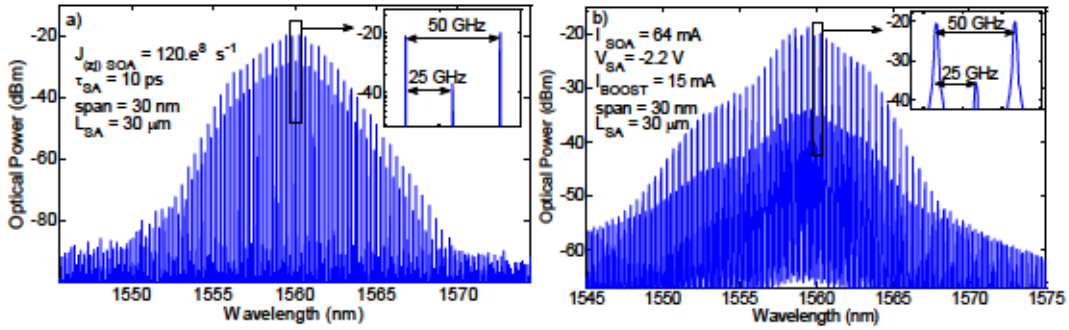

Figure 4.13. Optical Spectrum Dev_SA30. (a) Simulation. (b) Experimental, OSA trace.

The optical pulse train of the simulation and experimental results are depicted in Figure 4.14(a) and Figure 4.14(b), respectively. The results evidence the agreement of the stable optical pulse train and the time between pulses of 20 ps. We mainly observe in the experimental AC signal the background noise as in aforementioned on-chip colliding pulse mode-locked laser devices Dev_SA50 and Dev_SA40.

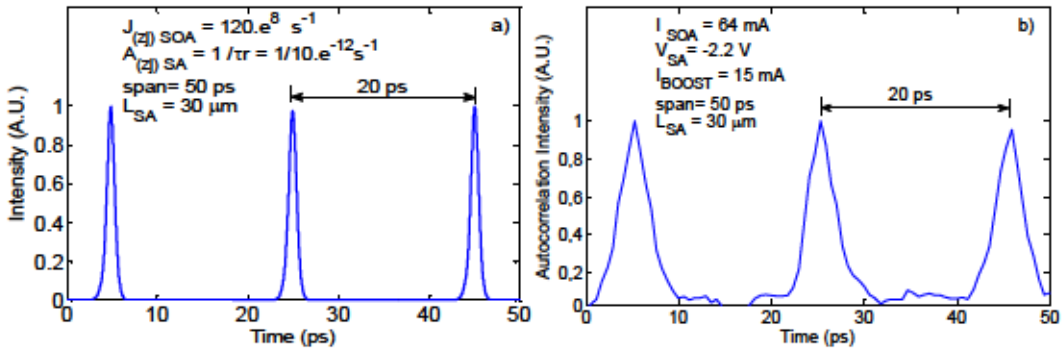

Figure 4.14. Optical pulse characterization Dev_SA30. (a) Simulated pulse train. (b) Experimental autocorrelation trace.

The agreement between simulation and experimental results is also visible in the optical pulse in a span of 15 ps, which is shown in Figure 4.15(a) and Figure 4.15(b), respectively. The pulse width of $\Delta\tau_s$ = 1.1 ps was estimated by a deconvolution of the Lorentzian pulse shape fitting and the time bandwidth product obtained was TBP_s = 0.40 for the simulation results, while a pulse width of $\Delta\tau_m$ = 0.95 ps and TBP_m = 0.39 for the experimental results were achieved. We would like to highlight that the TBP is close to the Fourier transform limit Lorentzian pulses for both cases.

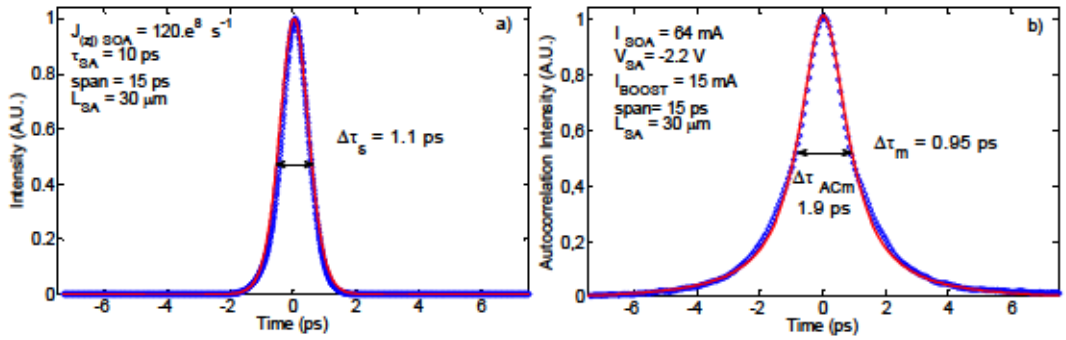

Figure 4.15. Pulse width Dev_SA30. (a) Simulation. (b) Experimental autocorrelation trace.

20 µm Saturable Absorber, CPM

The optical spectrum at the colliding pulse bias settings of the Dev_SA20 is depicted in Figure 4.16(a) and Figure 4.16(b), respectively. In both results, the agreement is identified in the Gaussian shape around peak. The inset in each picture shows the optical mode spacing of 25 GHz and double this frequency 50 GHz due to the colliding pulse mode locking condition. We observe a noticeable reduction of the side mode suppression in comparison with the aforementioned on-chip colliding pulse mode-locked laser devices Dev_SA50, Dev_SA40, and Dev_SA30. Also, the spectral bandwidth of the measured optical spectrum is wider than the experimental optical spectrum. The estimated spectral width of the simulated optical spectrum is $\Delta v_s = 375$ GHz while for the measured optical spectrum is $\Delta v_m = 450$ GHz obtained from the Gaussian fitting of both results of Dev_SA20.

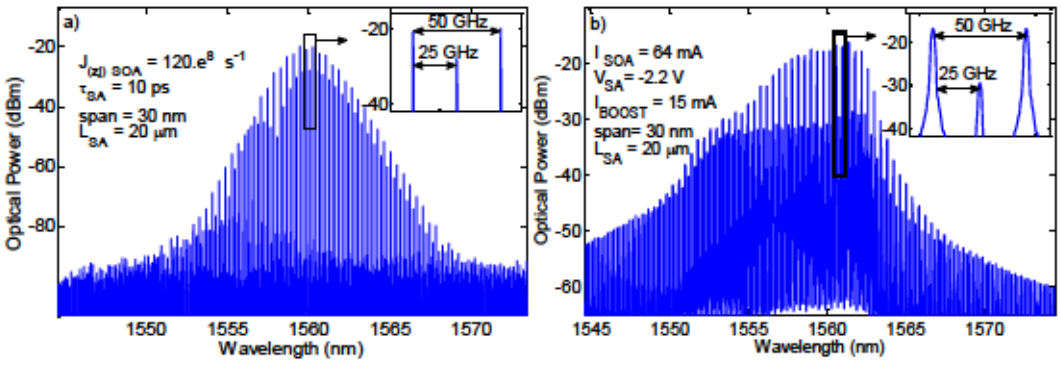

Figure 4.16. Optical Spectrum Dev_SA20. (a) Simulation. (b) Experimental, OSA trace.

The optical pulse train of Dev_SA20 from the simulation and experimental results are depicted in Figure 4.17(a) and Figure 4.17(b) respectively. The agreement between both results is in regards to the stable optical pulse train at 20 ps time between pulses. Also, the noise background is noticeable in the experimental AC signal while the simulation result does not provide noise background.

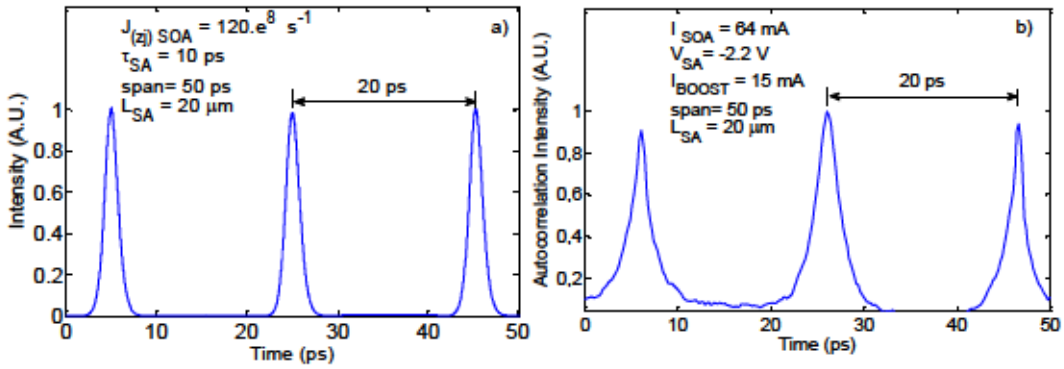

Figure 4.17. Optical pulse characterization Dev_SA20. (a) Simulated pulse train. (b) Experimental autocorrelation trace.

Figure 4.18(a) and Figure 4.18(b) sketch the optical pulse in a period of 15 ps of the simulation and experimental results, respectively. The pulse width was estimated using the Lorentzian pulse shape fitting. The pulse width of $\Delta\tau_s$ = 1 ps was estimated of the Lorentzian pulse shape fitting and the time bandwidth product obtained was TBP_s = 0.37 for the simulation results. For the experimental results, we achieved a pulse width of $\Delta\tau_m$ = 0.85 ps from a deconvolution of the autocorrelator measurement and TBP_m = 0.38. The TBP is close to the Fourier transform limit of Lorentzian pulse for both cases.

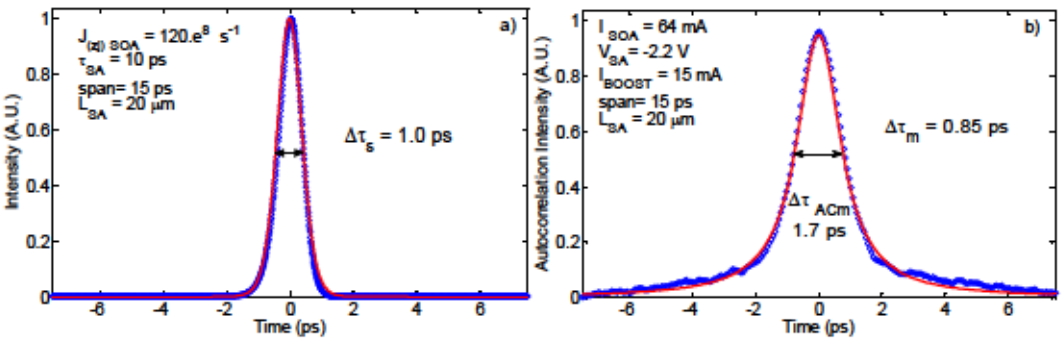

Figure 4.18. Pulse width Dev_SA20. (a) Simulation. (b) Experimental autocorrelation trace.

4.4 Analysis of the Saturable Absorber Length Influence

From the comparison of the simulation an experimental results of oc-CPM with different saturable length, we confirm the design rules provided by previous reports [1], [11], [13] for our colliding laser structures. The evaluation among all the samples with different saturable absorber length allows assessing the mode locking regimes and estimating the tendency of the pulse width, time bandwidth product, and side mode suppression ratio while the length of the SA changes from 20 um to 50 um in steps of 10 um.

For Dev_SA50, Dev_SA40 and Dev_SA30, which meet the design criteria, the relations of the absorber section length to cavity length are $L_{SA}/L_{cav} \approx 3\,\%$, $L_{SA}/L_{cav} \approx 2.45\,\%$, and $L_{SA}/L_{cav} \approx 1.84\,\%$, respectively. Regarding the gain to absorber, the ratios are $L_{SOA}/L_{SA} \approx 10$ times, $L_{SOA}/L_{SA} \approx 12$ times, and $L_{SOA}/L_{SA} \approx 16$ times. Finally, regarding the evaluation of the mode-locking regimes and considering Table 4.2, these devices Dev_SA50, Dev_SA40 and Dev_SA30 deliver stable pulse train.

Moreover, stable mode-locked regimes were achieved by Dev_SA20 in spite of both design rules are not met simultaneously. For Dev_SA20 the relations are $L_{SA}/L_{cav} \approx 1.23\,\%$ and $L_{SOA}/L_{SA} \approx 24$ times so the gain section is larger than the design rule recommendation. The Dev_SA20 works in mode locking regime, but we have to consider that the larger gain sections should be avoided due to the fact that an active waveguide is not the optimum medium in which to propagate short pulses because the pulses are broadened by the group velocity dispersion induced by the gain dispersion,

such that the broadening depends on the active section length. Table 4.4 summarizes the rules and the mode-locked regimes.

Design Criteria	Dev_SA50	Dev_SA40	Dev_SA30	Dev_SA20
Rule 1 : L_{SA}/L_{cav} 1% to 5 %	Yes	Yes	Yes	Yes
Rule 2 : L_{SOA}/L_{SA} 10 to 20	Yes (Close to the lower limit)	Yes (within the limits)	Yes (Close to the upper limit)	No (Outside the limits)
Mode-locked Regime	Stable	Stable	Stable	Stable, but long gain sections should be avoided

Table 4.4. Mode locking regimes and design rules.

From the comparison between simulation and experimental results, we conclude that the saturable absorber length variation affects the pulse width, time bandwidth product, and side mode suppression ratio. We confirm a direct relation among pulse width, time bandwidth product and side mode suppression ratio against saturable absorber length [1]. When reducing the length of the saturable absorber from 50 um to 20 um we observe the following behavior in the simulation and experimental results. First, the pulse width reduces from 1.3 ps to 1.0 ps in the simulation results while reduces from 1.5 to 0.85 ps in the experimental results. The pulse shape also changes while the pulse width reduces, starting with Gaussian pulse shape, passing through hyperbolic secant pulse shape, and finishing with Lorentzian pulse shape in the simulation and experimental results simultaneously. Second, time bandwidth product also reduces from 0.48 to 0.37 in the simulation or from 0.49 to 0.38 in the experimental results. And finally, the side mode suppression ratio reduces around 8 dBm for each 10 um length reduction of the saturable absorber, from 40 dBm to 8 dBm in the simulation or from 35 dBm to 10 dBm in the experimental results.

Figure 4.19(a), (b) and (c) show the simulation and experimental results of pulse width, time bandwidth product and side mode suppression ratio tendency while the saturable absorber length changes. In order to demonstrate that the variability of experimental results are within the tolerances of the results obtained from the FreeTWM software, 20 % error bars were included in the pulse width results while 10 % error bars were used in the time bandwidth product and side mode suppression ratio results in order to consider that the measurement is within the estimated tolerances.

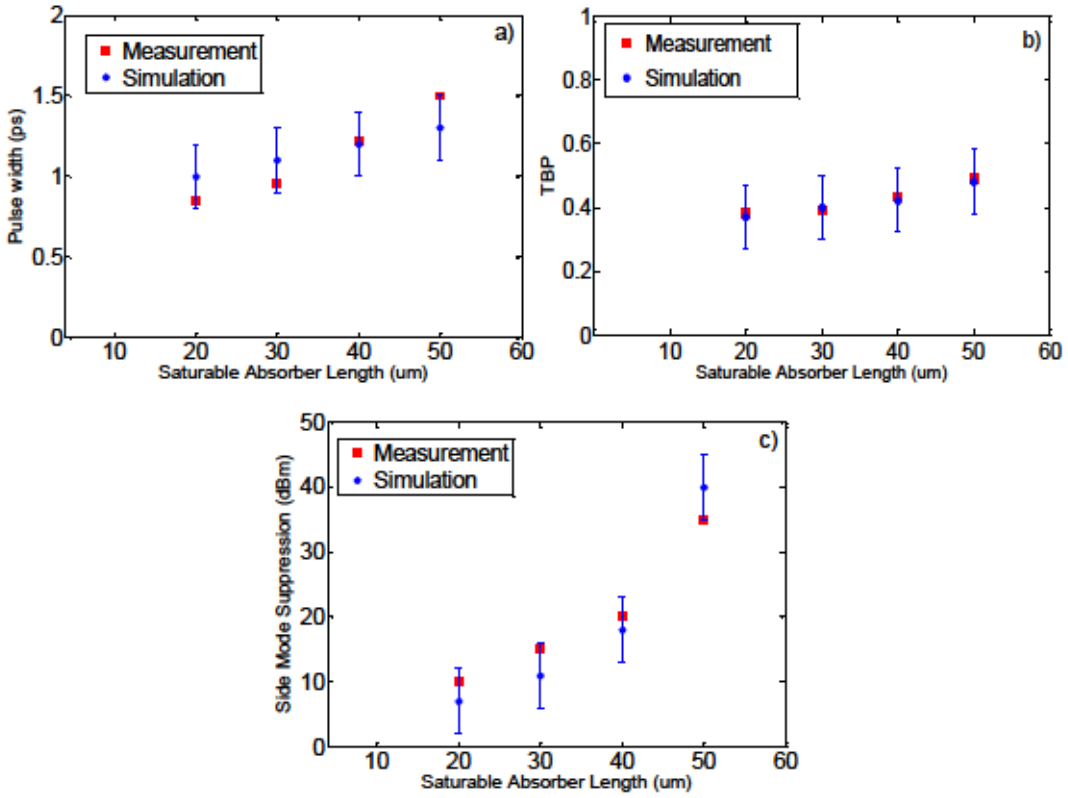

Figure 4.19. (a) Pulse width, (b) TBP, (c) SMSR vs. Saturable Absorber Length.

4.5 Conclusions

- We present, for the first time to the best of our knowledge, an on-chip colliding pulse mode-locked laser diode structure which uses multimode interference reflectors to define the cavity. These mirrors allow to precisely position the SA location in the cavity, achieving the colliding pulse mode-locked regime.
- The absorber length optimization was carried out in order to enhance the structure. The comparison between simulation results and experimental data reveals the agreement between both results.
- It was demonstrated with the simulation and experimental results that the absorber length reduction implies the pulse with reduction accompanied with the time bandwidth product and side mode suppression ratio reduction.
- The devices have been fabricated in a multi-project wafer service, using an active/passive technology generic foundry which allows accessing the generic technologies for integrated photonics (GTIP) and reduces costs.

4.6 References

[1] K. A. Williams, M. G. Thompson, and I. H. White, "Long-wavelength monolithic mode-locked diode lasers," *New J. Phys. A,* vol. 6, no. 179, pp. 1 – 31, 2004.

[2] S. Arahira, and Y. Ogawa, "480-GHz Subharmonic synchronous mode locking in a short-cavity colliding-pulse mode-locked laser diode," *IEEE Photonics Technol. Lett.*, vol. 14, no. 4, pp. 537-539, 2002.

[3] P. Vasil'ev P, "Ultrafast Diode Lasers: Fundamentals and Applications," London: Artech House, 1995.

[4] E. Bente, and M. Smit, "Ultrafast InP optical integrated circuits," *Proc. SPIE*, vol. 6124, pp. 612419, 2006.

[5] M. Smit, X. Leijtens, E. Bente, J. Van der Tol, H. Ambrosius, D. Robbins, M. Wale, N. Grote, and M. Schell, "Generic foundry model for InP-based photonics ICs," *IET Optoelectron.*, vol. 5, no. 5, pp. 187–194, 2011.

[6] C. R. Doerr and K. Okamoto, "Planar lightwave circuits in fiber optic communications," in Optical Fiber Telecommunications V A : Components and Subsystems, I. P. Kaminow, T. Li, and A. E. Willner, eds., 5th ed. Academic, 2008, pp. 269–342.

[7] L. Hou, M. Haji, B. Qiu, and A. C. Bryce, "Mode-locked laser array monolithically integrated with MMI combiner, SOA, and EA modulator," *IEEE Photonics Technol. Lett*, vol. 23, no. 15, pp. 1064-1066, 2011.

[8] J. Akbar, L. Hou, M. Haji, R. Dylewicz, M. J. Strain, J. H. Marsh, A. C. Bryce, and A. E. Kelly, "High average power (200 mW) 40 GHz mode-locked DBR lasers with integrated tapered optical amplifiers," *in Conference on Lasers and Electro-Optics (CLEO)*, CWIN.7, 2012, pp. 1-2.

[9] H. Fan, C. Wu, M. El-Aasser, N. K. Dutta, U. Koren, and A. B. Piccirilli, "Colliding pulse mode-locked laser," *IEEE Photonics Technol. Lett.*, vol. 12, no. 8, pp. 972-973, 2000.

[10] Y. K. Chen, M. C. Wu, T. Tanbun-Ek, R. A. Logan, and M. A. Chin, "Subpicosecond monolithic colliding-pulse mode-locked multiple quantum well lasers," *Appl. Phys. Lett.*, vol. 58, no. 12, pp. 1253-1255, 1991.

[11] J. Javaloyes and S. Balle, "Mode-locking in semiconductor Fabry-Perot lasers," *IEEE J. Quantum Electron.*, vol. 46, no. 7, pp. 1023–1030, Jul. 2010.

[12] The pure play InP Photonics foundry, "SMART Photonics", http://www.smartphotonics.nl/.

[13] R. G. Koumans, and R. Van Roijen, "Theory for passive mode-locking in semiconductor laser structures including the effects of self-phase modulation, dispersion, and pulse collisions," *IEEE Journal of Quantum Electronics*, vol. 32, no. 3, pp. 478-492, 1996.

[14] M. Kroh, "Semiconductor mode-locked laser for high-speed OTDM transmission," PhD thesis, Fakultät IV–Elektrotechnik und Informatik–der Technischen Universität Berlin, 2006.

[15] S. Latkowski, V. Moskalenko, S. Tahvili, L. Augustin, M. Smit, K. Williams, and E. Bente, "Monolithically integrated 2.5 GHz extended cavity mode-locked ring laser with intracavity phase modulators," *Optics letters*, vol. 40, no. 1, pp. 77-80, 2015.

[16] J. Javaloyes and S. Balle, "Freetwm: a simulation tool for multisection semiconductor lasers," available at http://www.uib.es/depart/dfs/onl/Softwares, 2012.

[17] V. Moskalenko, "Extended cavity passively mode-locked lasers in indium phosphide generic integration technology," Ph.D. thesis, Dept. Elect. Eng., Technical University of Eindhoven (TU/e), Eindhoven, The Netherlands, 2016.

Chapter 5

On-chip Colliding Pulse Mode-Locked Lasers for Millimeter Wave Generation

5.1 Introduction

Colliding pulse mode-locked semiconductor lasers (CPM) are promising candidates for the generation of ultrafast and ultrashort optical pulses with excellent characteristics [1]. The wide range of repetition rates which CPM structures can reach make them potential sources for the generation of carrier wave frequencies in the millimeter-wave range for broadband wireless communications systems [2]. All the advantages of CPM lasers are acquired from their structure due to the fact that a saturable absorber section located at the center of the resonator between two semiconductor optical amplifier sections within the Fabry-Perot cavity, allows the collision of two counter-propagating pulses which leads to a more effective pulse shortening [3], doubling the repetition rate [1], and increasing stability [4].

In this chapter, we present novel on chip colliding pulse mode-locked structures which are capable of generating mmW repetition rate frequencies, achieved by adjusting the length of the cavity, reducing the cavity length to increase the repetition rate frequency into the millimeter frequency range.

5.2 Novel On-chip Colliding Pulse Mode-Locked Lasers for Millimeter Wave Generation

The previous analysis on absorber length optimization and design rules allowed us to optimize on-chip colliding pulse mode-locked lasers (oc-CPM) which are capable to provide stable regimes. In order to increase the repetition rates, we started designing two devices with different cavity lengths.

The first one (Dev_A), shown at the top in Figure 5.1(a), was designed to have a fundamental repetition rate of 18.47 GHz, with colliding repetition rate frequency at 36.94 GHz. The advantage of this frequency is that both frequencies are within the range of our electrical spectrum analyzer, an Anritsu MS2668C, which covers from 9 KHz to 40 GHz. This enables us to avoid the need of external mixer heads, which introduce losses in excess of 30 dB, to characterize the signals.

An additional device (Dev_B), shown at the bottom of Figure 5.1(b), had a cavity length about half the cavity length of Dev_A, aiming to generate signals in the E-band range (60-90 GHz), currently being proposed for wireless communications.

Table 5.1 summarizes the features of both devices developed in the SMART Photonics multi-project wafer (MPW) run. Also the Table 5.1 shows that both devices meet the design criteria to develop optimized on-chip colliding pulse mode-locked lasers which are capable to provide stable regimes with very low jitter.

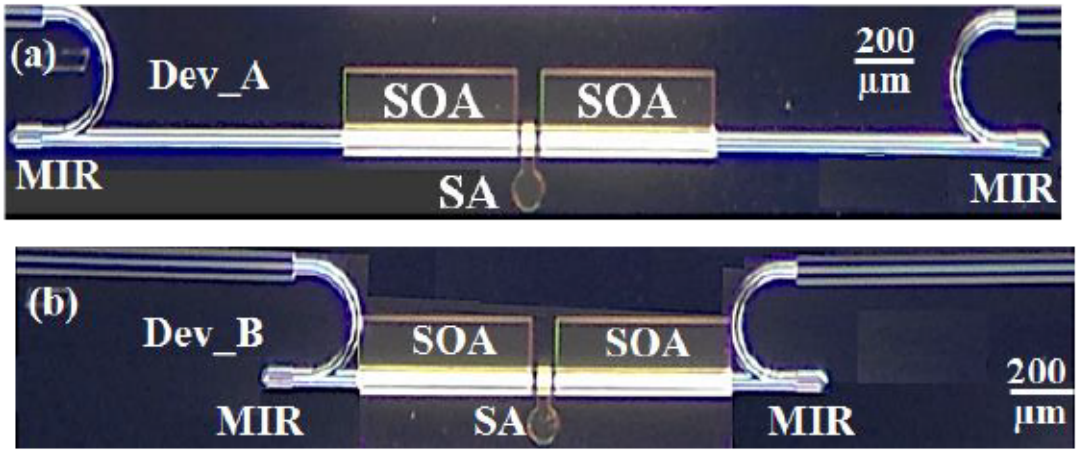

Figure 5.1. Microscope photograph of oc-CPM for millimeter wave generation. (a) Dev_A, SHF = 36.94 GHz. (b) Dev_A, SHF = 36.94 GHz.

	Components Length (um)					*Repetition Rate (GHz)*		*Design Criteria*		
Devices	*MIR*	*SOA*	*SA*	*PW*	L_{cav}	*FF*	*SHF*	*Rule 1* L_{SA}/L_{cav}	*Rule 2* L_{SOA}/L_{SA}	*Mode Locked Regime*
Dev_A	90.3	360	20	1229.4	2210	18.47	36.94	1 %	18 times	Stable
Dev_B	90.3	360	20	253.4	1234	34.88	69.76	1.6 %	18 times	Stable

Table 5.1. Devices fabricated in the SMART Photonics multi-project wafer (MPW) run.

5.3 Simulation Results of oc-CPM for Millimeter Wave Generation

The FreeTWM software was used to simulate the devices with the same material parameters used before in the study of the saturable absorber length optimization. The characterization in detail of the colliding pulse mode-locked regime was carried out at a bias setting exhibiting this behavior. For the simulation results the bias setting was at injected carrier rate $J_{(ZJ)SOA} = 120.e^8 s^{-1}$ (twice the simulated threshold current). This is in agreement to the fact that in the experimental results we forward bias the SOA with a current around double of the threshold current. The absorber section works in the regime of slow saturation so the absorber recovery time is $\tau_{SA} =$ 10 ps. The simulation

process allows estimating the performance of the oc-CPM in the frequency and time domains.

Performing the simulation for Dev_A, the FreeTWM delivers the profiles for the optical power, electrical fields intensity, and carriers concentration which are shown in Figure 5.2(a), Figure 5.2(b), and Figure 5.2(c), respectively. All the profiles are sketched against discretized length and the profiles are obtained after 500 single trips in the cavity. The discretized length is related to the cavity length in one point to two micrometers relation, so 1105 points in the discretization correspond to 2210 um in the cavity length. This relation was used in order to reduce the computation time in simulation stage. We observe all the features previously described in the absorber length optimization, presenting the intensities and fields of the two optical pulses that coexist within the cavity, shown in Figure 5.2(a) and Figure 5.2(b), respectively. Also, the amount of carriers concentrated in SOA sections is depicted in Figure 5.2(c).

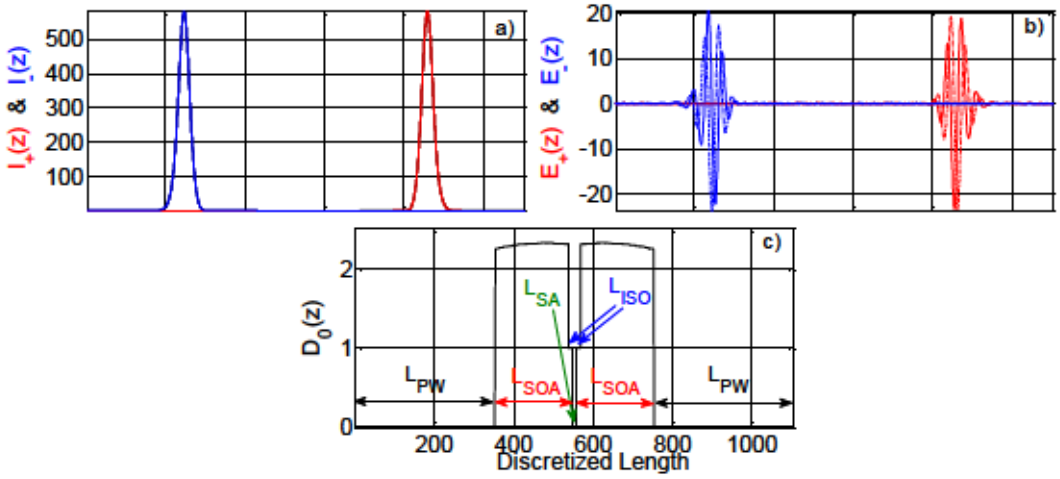

Figure 5.2. Profiles of Dev_A. (a) Optical power. (b) Electrical field intensity. And (c) Carriers concentration.

The simulation of Dev_B provides similar features as obtained in previous simulations, so we observe the intensities of the two coexisting pulses in Figure 5.3(a) while the fields of both pulses are sketched in Figure 5.3(b). Besides, the amount of carriers concentrated in SOA sections depicted in Figure 5.3(c). It is essential to highlight that as in previous simulations all profiles obtained after 500 single trips in the cavity are depicted versus discretized length. In the simulation of Dev_B the discretized length is 1234 points due to the discretization correspond to 1234 um in the cavity length.

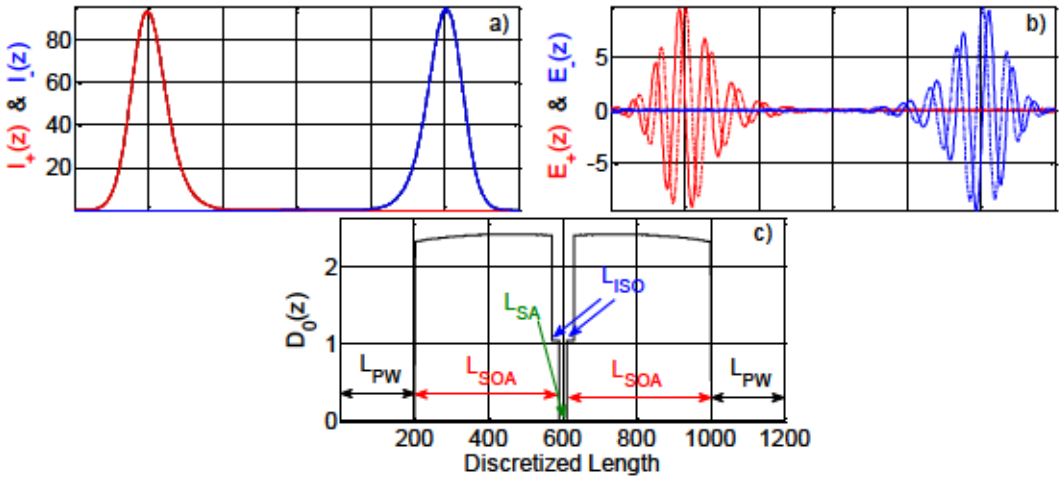

Figure 5.3. Profiles of Dev_B, delivered by FreeTWM. (a) Optical power. (b) Electrical field intensity. And (c) Carriers concentration.

5.3.1 Frequency Spectrum Simulation Results

Optical Spectrum Results

The simulated optical spectra of the Dev_A and Dev_B at colliding pulse mode-locked regime are depicted in Figure 5.4(a) and Figure 5.4(b) respectively. The simulation result of the optical spectrum is evaluated in terms of symmetry and side mode suppression ratio, so the symmetry and the side mode suppression more than 20

dBm in both designs reveals that the design meets the design criteria and therefore the designed on-chip mode locked lasers are able to generate stable mode locked regimes. Also, Figure 5.4(a) shows inset the fundamental frequency at FF_A = 18.47 GHz and twice this frequency SHF_A = 36.94 GHz due to the colliding pulse mode locking condition. While, Figure 5.4(b) depicts inset the fundamental frequency at FF_B = 34.88 GHz and twice this frequency SHF_B = 69.76 GHz due to the colliding pulse mode locking condition. The estimated spectral width from the optical spectrum through a Gaussian fitting of Dev_A is $\Delta\nu_{Dev\_A} = 410$ GHz and Dev_B is $\Delta\nu_{Dev\_B} = 385$ GHz.

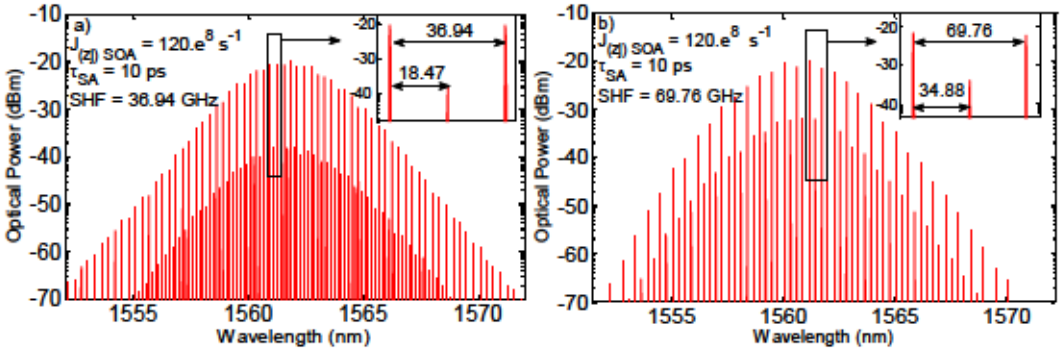

Figure 5.4. Optical Spectrum, span 30 nm. a) Dev_A, SHF_A = 36.94 GHz. b) Dev_B, SHF_B = 69.76 GHz.

Electrical Spectrum Results

Figure 5.5(a) and Figure 5.5(b) show the beating electrical spectrum span 50 = GHz at colliding pulse mode-locked regime of Dev_A and Dev_B, respectively. The only peak present in the beating electrical spectrum which appears at second harmonic frequency SHF_A = 36.94 GHz for the Dev_A and at SHF_B = 69.76 GHz for the Dev_B confirms that both designs are on colliding pulse mode locking regime. The estimated beating linewidth using a Lorentzian fitting of the simulation results is in order of MHz

due to the fact we are limited for the current noise, spontaneous noise, resolution of the software, and so on. The beating linewidth of the SHF_A = 36.94 GHz for the Dev_A is $\Delta v_{RF2\text{-}A}$ = 1.72MHz while the beating linewidth of the SHF_B = 69.76 GHz for the Dev_B is $\Delta v_{RF2\text{-}B}$ = 3.77 MHz.

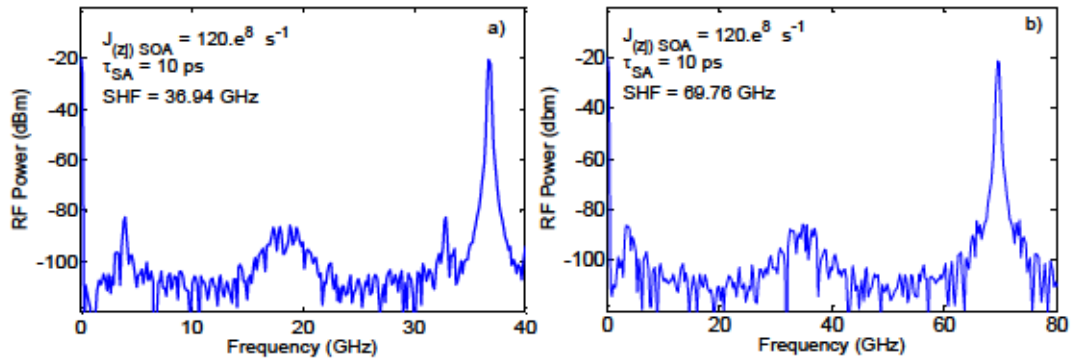

Figure 5.5. Electrical Spectrum. a) Dev_A, SHF_A = 36.94 GHz (span =40 GHz). b) Dev_B, SHF_B = 69.76 GHz (span =80 GHz).

5.3.2 Optical Pulse Results

The train of optical pulses obtained from the simulation at 7ns and 70 ps span are sketched in Figure 5.6(a), (b), (c), and (d) for the Dev_A and Dev_B, respectively. The train of pulses is evaluated in terms of stability, and repetition rate. For both devices, we observe stability due to we have a flat pulse train and there is not variation in the amplitude of the pulse train. The obtained repetition rate corresponds with the designed repetition rate for each device. Besides, the FreeTWM also allows estimating the pulse width of the designed oc-CPM samples. The hyperbolic secant pulse shape was used for the estimation of the pulse width for both devices. We expect to get the pulse width of $\Delta\tau_{\mathbf{Dev\_A}} = 0.8\,ps$ for Dev_A which is sketched in Figure 5.6(e) and $\Delta\tau_{\mathbf{Dev\_B}} = 0.9\,ps$ for Dev_B, which is shown in Figure 5.6 (f). Also, estimating the spectral width from the optical spectrum through a Gaussian fitting of Dev_A $\Delta v_{\mathbf{Dev\_A}}$ = 410 GHz and

Dev_B $\Delta\nu_{\text{Dev\_B}} = 385$ GHz, we expect to achieve time bandwidth products close to the transform limit hyperbolic secant pulse for Dev_A and Dev_B such as $TBP_{\text{Dev\_A}} = 0.33$ and $TBP_{\text{Dev\_B}} = 0.35$, respectively.

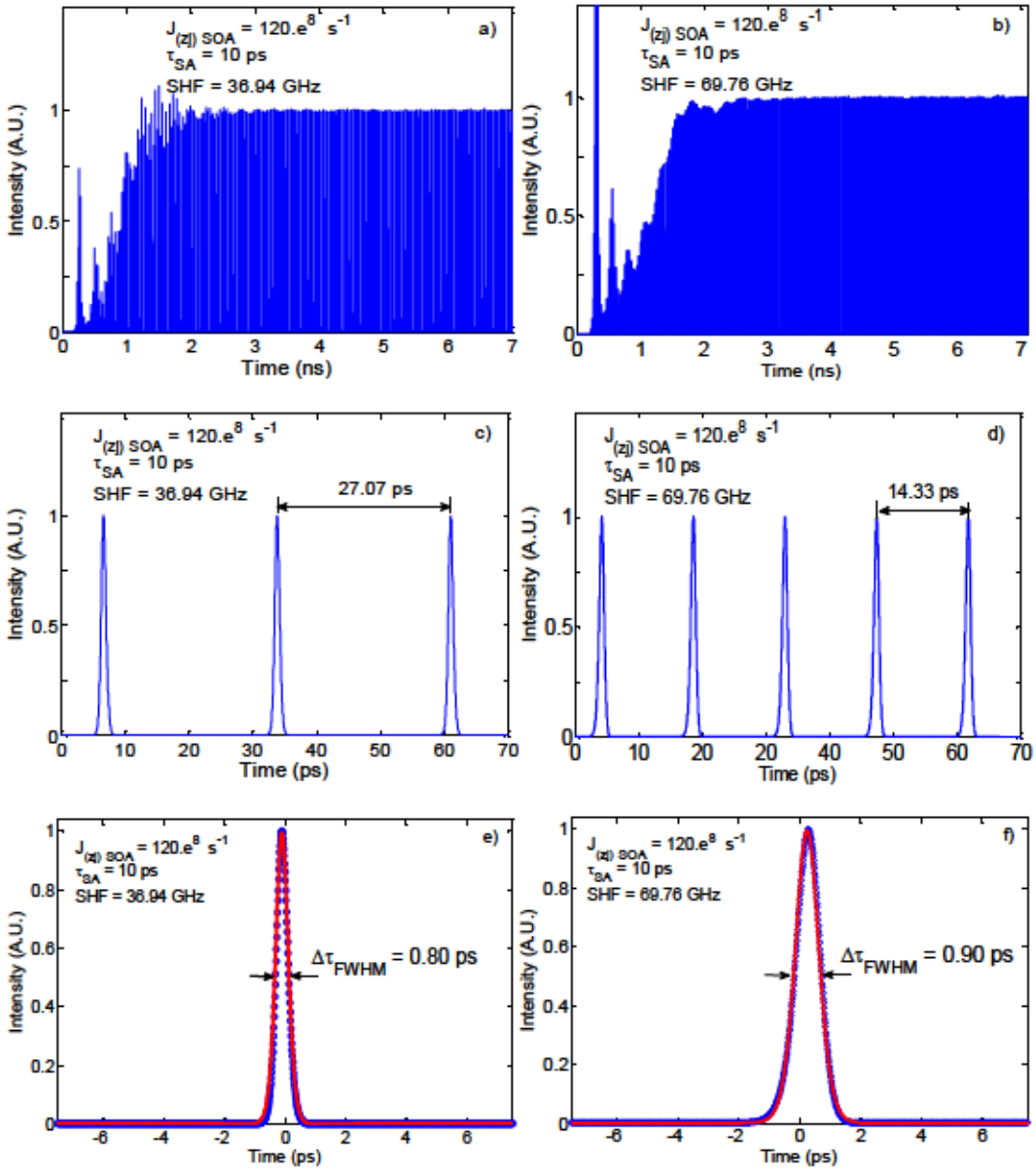

Figure 5.6. a) Pulse train Dev_A, 7 ns. b) Pulse train Dev_B, 7 ns. c) Pulse train Dev_A, 70 ps. d) Pulse train Dev_B, 70 ps. e) Pulse width Dev_A. f) Pulse width Dev_B.

5.4 Experimental Results of oc-CPM for Millimeter Wave Generation

The output light power versus current injection (P-I) curve of the two devices is shown in Figure 5.7. Where Figure 5.7(a) and Figure 5.7(b) show the P-I curve for Dev_A and Dev_B respectively when a fixed SA reverse voltage V_{SA} = -1.7 V is applied. We can clearly observe that the threshold current for Dev_A is 64 mA, while for Dev_B, we measured 35 mA. Due to the fact that both devices use the same building blocks, and that the only difference between them is the length of the passive waveguide, this difference must be attributed to passive waveguide propagation losses. Thanks to the 90/10 coupler, while measuring the optical power, we also measured the optical spectrum. The evolution of the optical spectrum with current injection for each of the two devices, under the same reverse bias condition V_{SA} = -1.7 V, are shown in Figure 5.7(c) for Dev_A and Figure 5.7(d) for Dev_B. We clearly identify on both devices an initial regime of operation, continuous wave (CW), in which different Fabry-Perot modes start lasing, followed by the onset of stable mode locking, in which the optical spectrum takes a Gaussian distribution. In Dev_A, the range of currents with mode locking (ML) goes from 72 mA to 100 mA (which is the maximum current injected into the device), while Dev_B from 52 mA to 100 mA, the device enters into a colliding pulse mode-locked state.

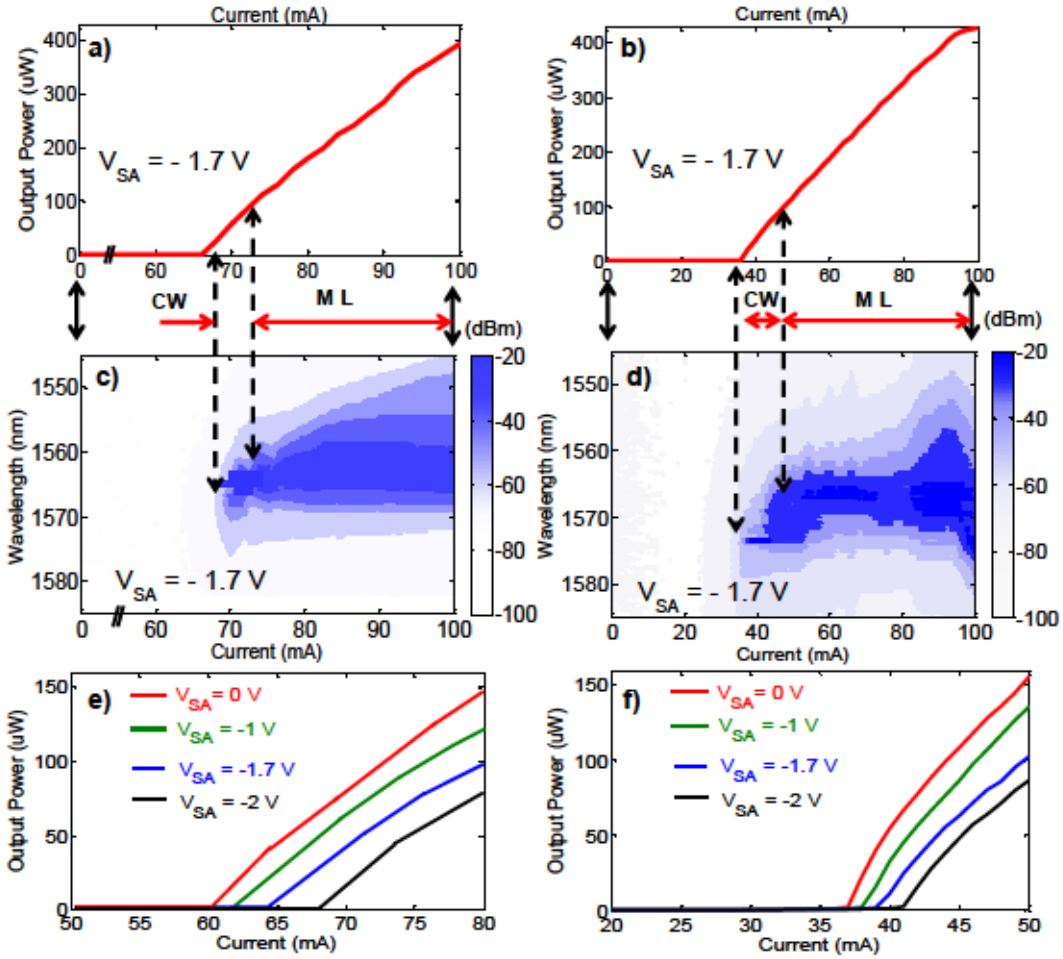

Figure 5.7. Optical power versus injection current (P-I curve) for: (a) Dev_A and (b) Dev_B. Identified regions are CW: continuous-wave, ML: mode-locked. Evolution of optical spectrum: (c) Dev_A and (d) Dev_B. Detailed P-I curve around threshold at different SA voltages for: (e) Dev_A and (f) Dev_B.

Focusing around the threshold current level, we performed detailed measurements of the P-I curve at different voltage levels on the SA (with V_{SA} = 0 V, -1 V, -1.7 V and -2 V). As shown in Figure 5.7(e) and Figure 5.7(f), we do not observe sharp jumps of the optical power nor have we measured any hysteresis on any of the devices. The appearance of hysteresis has been reported in quantum dot [5] and quantum well [6] gain material devices, usually linked to high reverse bias voltages on devices with large SA sections, with gain-to-absorber length ratios of 7:1 and 14:1 respectively, while in our case this ratio is 40:1. The short SA was designed following previous CPM

observations which showed a reduction in the pulse duration as the absorber width is reduced [1]. We can therefore conclude that hysteresis is not observed due to the relatively short SA (20 μm) to the gain section length (800 μm) and the low reverse bias voltages from 0 to -3.5 V. These levels were used to avoid generating a high photocurrent level at the absorber.

Optical Spectrum Characterization

To characterize in detail the colliding mode-locked regime, we have selected a bias point exhibiting this behavior, at a gain section current I_{SOA} = 80 mA and SA reverse biased V_{SA} = -1.7 V.

The optical spectrum for Dev_A is shown in log and linear scales in Figure 5.8(a) and Figure 5.8(b), respectively. The emission wavelength is 1562 nm, and the full-width half-maximum (FWHM) is Δv = 3.244 nm (404.8 GHz). The inset in Figure 5.8(a) shows a detail of the optical mode spectrum, side mode suppression ratio (SMSR) between the fundamental mode spacing (18.47 GHz) to the colliding mode spacing (36.94 GHz) is 22 dB.

For Dev_B, the log and linear scale optical spectrums are shown in Figure 5.8(c) and Figure 5.8(d) respectively in the same bias conditions (I_{SOA} = 80 mA, V_{SA} = -1.7 V). The device has the same emission wavelength range, around 1562 nm, with FWHM Δv = 2.771 nm (345.8 GHz), slightly narrower than the previous one. At the inset in Figure 5.8(c) we observe that the SMSR between the modes spaced at the fundamental frequency to those spaced at the colliding frequency spacing is similar, 24 dB, despite the higher repetition rate.

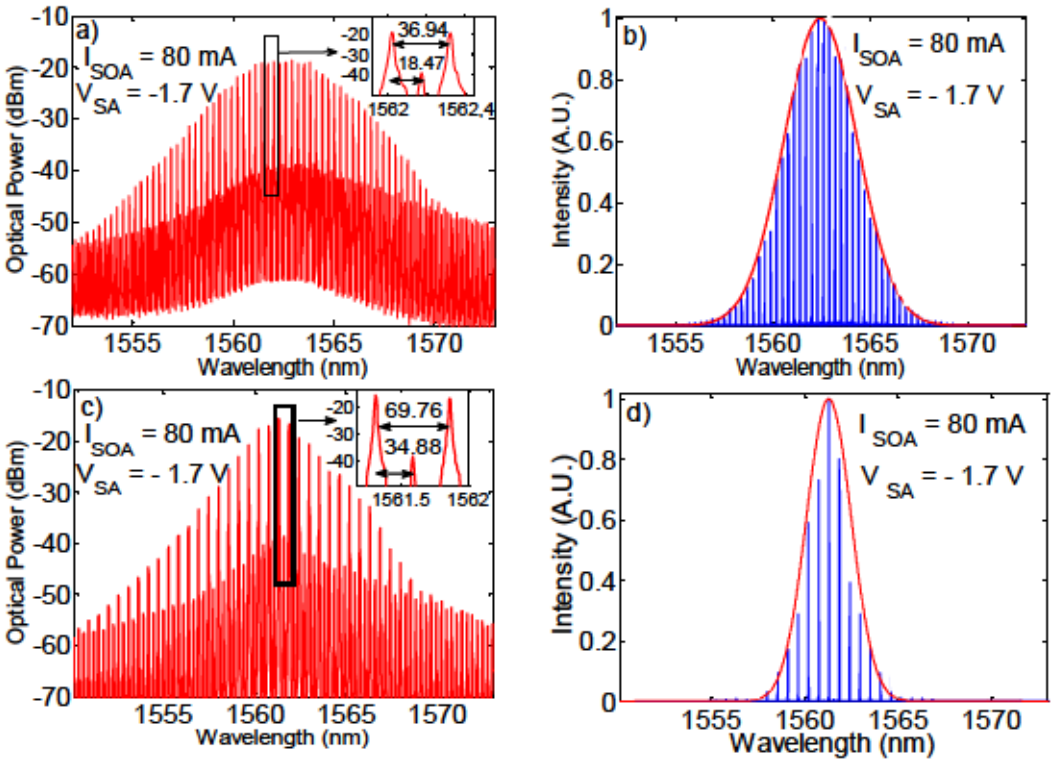

Figure 5.8. a) Optical spectrum log scale of the Dev_A. The inset shows the frequency mode spacing of 36.94 GHz, resolution 0.02 nm. (b) Optical spectrum linear scale of the Dev_A. (c) Optical spectrum log scale of the Dev_B. The inset shows the frequency mode spacing of 69.76 GHz, resolution 0.02 nm. (d) Optical spectrum linear scale of the Dev_B.

Electrical Spectrum Characterization

The electrical characterization of the generated RF beat note was performed using a 90 GHz bandwidth PIN photodiode connected to a 40 GHz electrical spectrum analyzer. For this reason, we focused the electrical analysis on Dev_A, which has a colliding repetition rate frequency within this range, comparing different operating conditions. First, we analyze the electrical spectrum at the same gain current level that we used for the optical spectrum, setting gain section at I_{SOA} = 80 mA. Figure 5.9 shows the results when the saturable absorber is not biased (V_{SA} = 0 V). Figure 5.9(a) shows the full span of the electrical mode beating spectrum. In this condition, peaks at the fundamental (FF

= 18.47 GHz) and second harmonic (SHF = 36.94 GHz) frequencies are visible. As shown in Figure 5.9(b) the two electrical frequencies are maintained as the current increases from 40 mA (close to the threshold) to 100 mA (the maximum injected current) exhibiting slight variations of the order of 240 MHz for the FF and 160 MHz for the SHF. It is worth noticing that the shift of the colliding frequency (SHF) is smaller than that of the fundamental. This is in agreement with the general observation that colliding pulse mode-locked structures are more stable than fundamental mode locking ones [1].

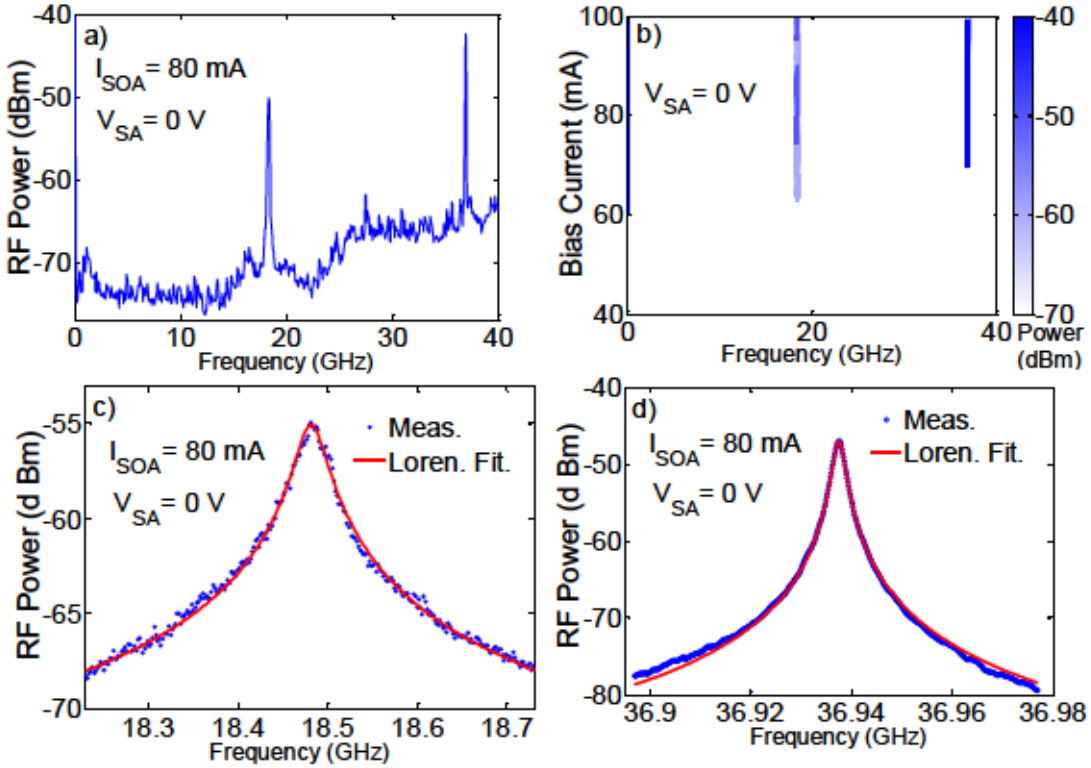

Figure 5.9. (a) Electrical spectrum of the Dev_A at free running condition, CF = 20 GHz, span = 40 GHz, RBW = 3 MHz, VBW = 3 MHz. (b) Electrical spectra map of the Dev_A at V_{SA} = 0 V. (c) Fundamental frequency linewidth of the Dev_A , CF = 18.473 GHz, span = 500 MHz, RBW = 1MHz, VBW = 1 MHz. (d) Second harmonic frequency linewidth of the Dev_A, CF = 36.946 GHz, span = 90 MHz, RBW = 1MHz, VBW = 1 MHz.

In Figure 5.9(c) and Figure 5.9(d) we show the electrical beat note linewidth (dotted blue line) and its fitting to a lorentzian line-shape (continuous red line) for the FF and SHF respectively. From Figure 5.9(c), the linewidth of the fundamental frequency is $\Delta\nu_{RF}$ = 15.41 MHz and from Figure 5.9(d), the linewidth of the second harmonic is $\Delta\nu_{RF2}$ = 1.17 MHz. We observe that the linewidth of the second harmonic frequency is smaller, and assume that is due to the colliding pulse mode-locked (CPM) structure of the device [1].

We now present the electrical mode beating spectrum in a colliding pulse mode locked condition, keeping the gain section at I_{SOA} = 80 mA, setting the SA at V_{SA} = -1.7 V. As shown in Figure 5.10(a), presenting the full span, the only peak present in the spectrum appears at the second harmonic (SHF = 36.94 GHz). Figure 5.10(b) shows that this is the case for the entire range of variation of the gain section current (from 40 mA to 100 mA), where the fundamental frequency appears over a small range from 70 to 79 mA, after which it disappears. In this regime, we also observe a reduction in the SHF shift with current, down to 80 MHz for a current change from 68 mA to 100 mA. The detailed trace of the colliding RF beat signal is shown in Figure 5.10(c), using blue circles for the experimental data, and a continuous red line for the lorentzian line-shape fit. The linewidth of this frequency tone is $\Delta\nu_{RF2}$ = 343 KHz, one order of magnitude smaller than the one achieved with no reverse bias voltage in the SA. We can therefore highlight the stability of the colliding regime of these novel devices.

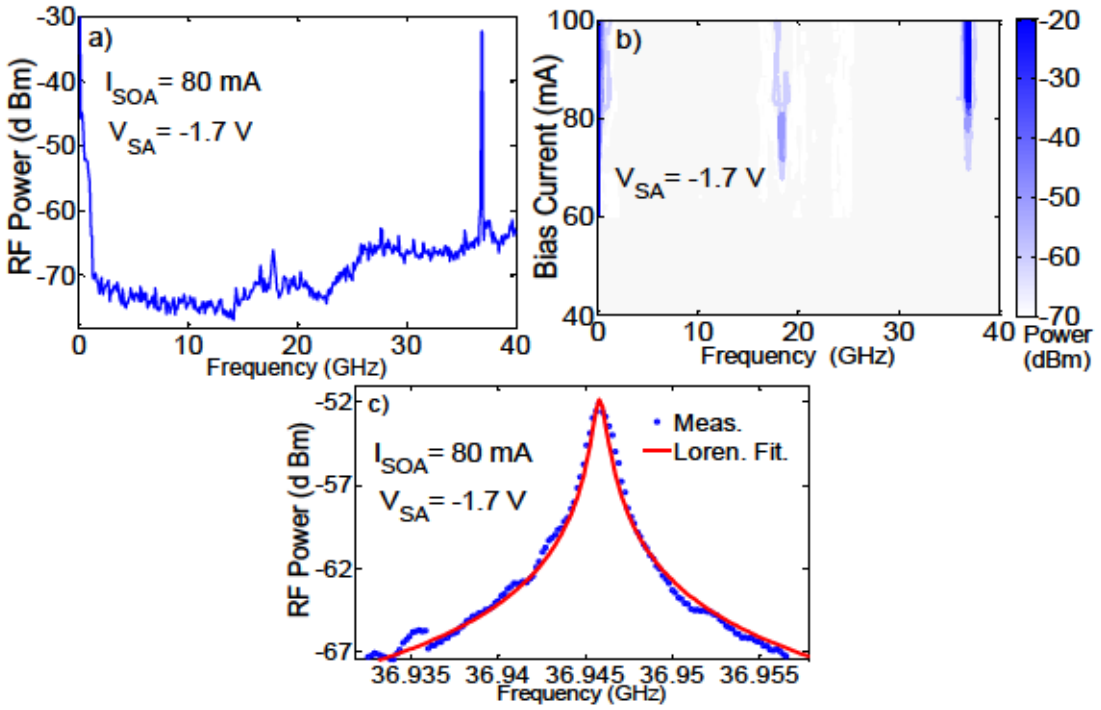

Figure 5.10. Electrical spectrum of the Dev_A at a colliding pulse mode locking regime: (a) full span, (b) Electrical spectrum evolution at V_{SA} = -1.7 V and (c) Colliding beat note linewidth.

For the sake of comparison we present in Figure 5.11(a) the electrical mode beating spectrum of Dev_B, when the device is biased in a colliding regime using the same conditions (I_{SOA} = 80 mA, V_{SA} = -1.7 V). This measurement required the use of external multiplication head Anritsu MA2744A (50 GHz - 75 GHz) to down-convert the repetition rate frequency of the signal (69.76 GHz) to the input range of the electrical spectrum analyzer. The linewidth of this tone is $\Delta\nu_{RF2}$ = 1.91 MHz and is shown in Figure 5.11(b).

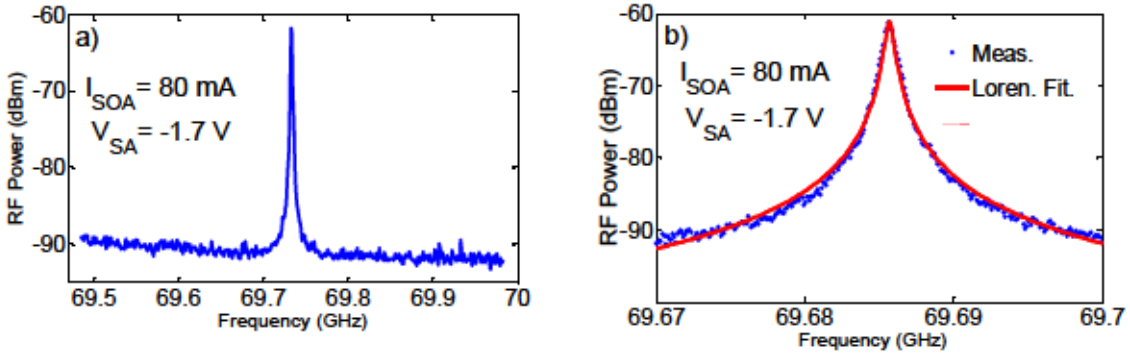

Figure 5.11. Electrical spectrum of the Dev_B at a colliding pulse mode locking regime: (a) Span = 500 MHz, (b) Colliding beat note linewidth.

Pulse Characterization

The pulse characterization is performed using a background-free APE Pulse-Check auto-correlator. The pulse widths for Dev_A were measured under various conditions in order to analyze the evolution of the pulse width with gain section current and SA reverse voltage. We have first measured the pulse width as the injection current (I_{SOA}) is varied from 60 mA to 120 mA while the reverse voltage at the saturable absorber SA (V_{SA}) remains fixed at V_{SA} = -1.7 V. The evolution of the pulse width versus gain section current level is shown in Figure 5.12(a), in which, the pulse width data is represented by blue circles and is fitted to a linear curve (red, continuous line). In the same figure, we introduce the results about the time bandwidth product (TBP), representing the measured data with blue squares, which are fitted to a linear trace (black, continuous line) is depicted simultaneously. We demonstrate the linear dependence between the pulse width (and TBP) with the current injection level into the gain section.

We have also analyzed in Dev_A the dependence of the pulse width with varying reverse voltage in the SA (V_{SA}) from -1.5 V to -3 V at a fixed injection current level at I_{SOA} = 80 mA. Figure 5.12(b) represents the measured pulse width data versus reverse voltage levels using blue dots, which are fitted to an exponential trace (red, continuous line). The time bandwidth product (TBP) data is also included with blue squares, fitted to a linear curve (black, continuous line). We observe the exponential dependence of the pulse width with the reverse SA voltage.

We would like to highlight that appreciate the same trends as reported in other mode-locked structures, showing pulse broadening with increasing injection current usually attributed to self-phase modulation (SPM) and shortening with increasing absorber reverse voltage due to absorber recovery time reduction [6]. The shortest pulse-width that we have achieved, assuming a hyperbolic secant pulse shape, is $\Delta\tau$ = 0.64 ps, when the absorber is biased at V_{SA} = -3.0 V and gain section to I_{SOA} = 80 mA. Figure 5.12(c) shows the autocorrelation trace of the shortest pulse. The time bandwidth product (TBP) obtained was TBP = 0.39, close to the Fourier transform limit 0.3148 [7].

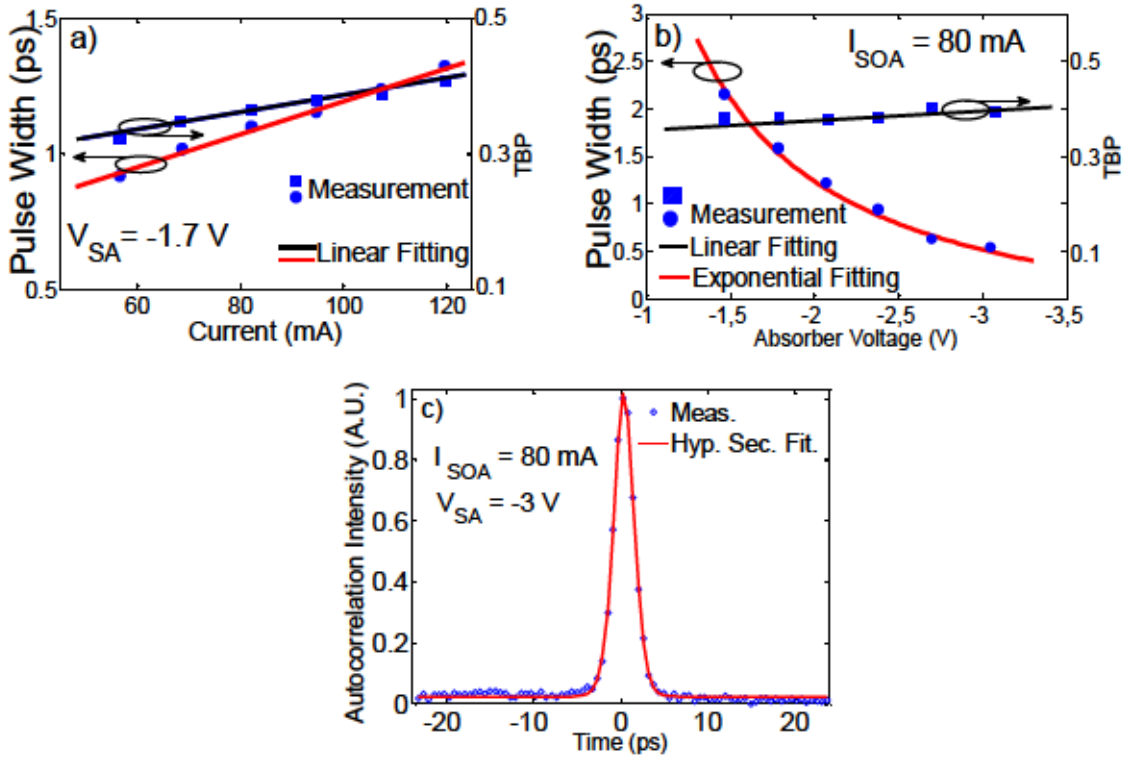

Figure 5.12. Optical pulse characterization: (a) Pulse width and TBP versus gain section current level. (b) Pulse width and TBP versus reverse absorber voltage and (c) Shortest pulse optical line shape.

Noise characterization

The noise performance of the Dev_A was evaluated in order to quantify the stability of the colliding pulse mode-locked regime, when the gain section is biased at I_{SOA} = 80 mA and the SA is biased at V_{SA} = -1.7 V. We measured the phase noise, which calculates the stability of the generated signal frequency and the amplitude noise which quantifies the variation of a pulse peak level from the average value. The phase noise allows defining the timing jitter which provides the stability in terms of femto seconds. Using the Von der Linde method, the timing jitter can be extracted from the integration of the single side band phase noise level over a frequency range [8] while the amplitude

noise is defined by the integration of the relative intensity noise [9]. It is common to use the ITU-recommended integration ranges defined by viable clock recovery techniques [10], in order to define the timing jitter and the amplitude noise. The noise evaluation was extracted from the integration range [4-80 MHz] which is used to define the amplitude noise and the phase noise [11]. Figure 5.13(a) depicts the single side-band phase noise (SSB - L(f)) of the Dev_A, the obtained timing jitter is σ_T = 2.2 ps, integration range [4–80 MHz] and Figure 5.13(b) shows the recording of the amplitude noise measurement of the Dev_A, where we were able to determine the amplitude noise N_{AM} = 0.012 dBc (< 0.036 %), integration range [4 – 80 MHz].

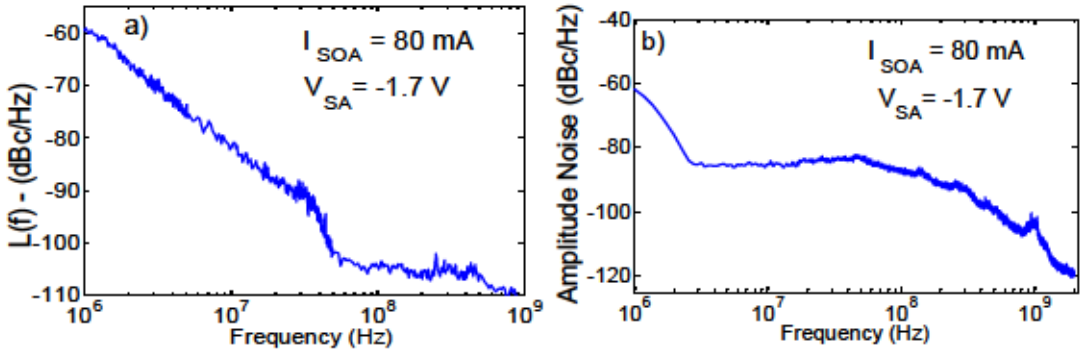

Figure 5.13. (a) Single side-band phase noise of the Dev_A at the pure colliding pulse mode locking condition. (b) Amplitude noise measured at the pure colliding pulse mode locking condition of the Dev_A.

Operating Regimes Characterization

Figure 5.14 sketches the map of the colliding pulse mode-locked regime of the Dev_A working at 36.94 GHz. The stable colliding pulse mode-locked operation was achieved for a wide range of bias settings when the forward bias current in the SOA sections are ranging from 72 mA to 100 mA and the reverse bias voltage in the absorber section varying within a – 1.4 V to – 3.0 V range, which is depicted by the red area in

Figure 5.14. Simultaneously, the degradable, deteriorated, poor, unstable and no existence of colliding pulse mode-locked regime at 36.94 GHz is denoted by the white areas. The no lasing regime lower than the threshold current at 64 mA is depicted by the yellow area and the continuous wave regime is denoted by the black area when the forward bias current in the SOA sections are ranging from threshold current to 71 mA and the reverse bias absorber section varying in the whole range within a 0 V to – 3 V.

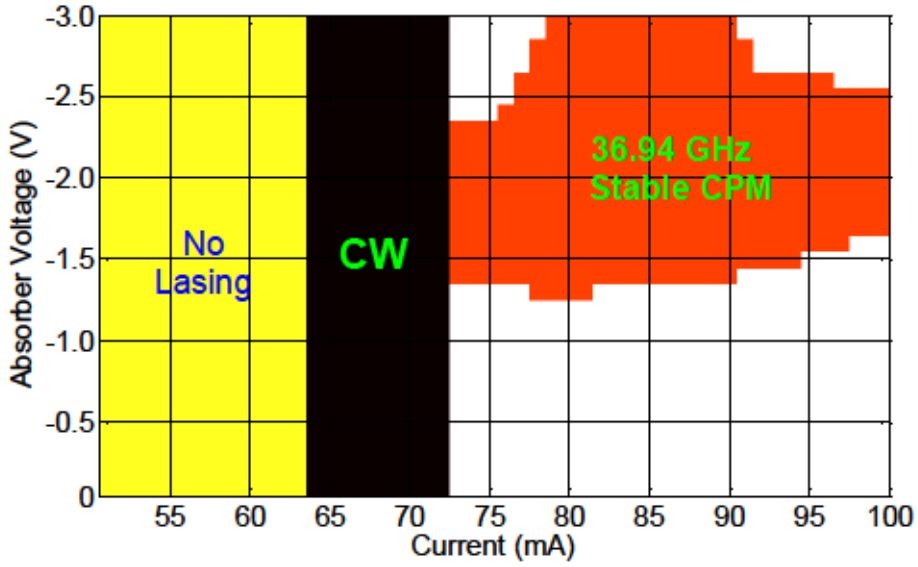

Figure 5.14. Measured map of the colliding pulse mode-locked regimes of Dev_A working at 36.94 GHz as a function of forward bias current and the reverse bias voltage.

Finally, the map of the colliding pulse mode-locked regime of the Dev_B working at 69.76 GHz is shown in Figure 5.15. The stable colliding pulse mode-locked operation regime was achieved for a wide range of bias settings when the forward bias varies from 44 mA to 100 mA and the reverse bias voltage is within a – 1.4 V to – 3.0 V range which is depicted by the red area in Figure 5.15. The no lasing regime lower than the threshold current at 35 mA is depicted by the yellow area and the continuous wave

regime is denoted by the black area when the forward bias current in the SOA sections are ranging from threshold current to 51 mA and the reverse bias absorber section varying in the whole range. Also, the degradable, deteriorated, poor, unstable and no existence of colliding pulse mode-locked regime at 69.76 GHz is denoted by the white areas in Figure 5.15.

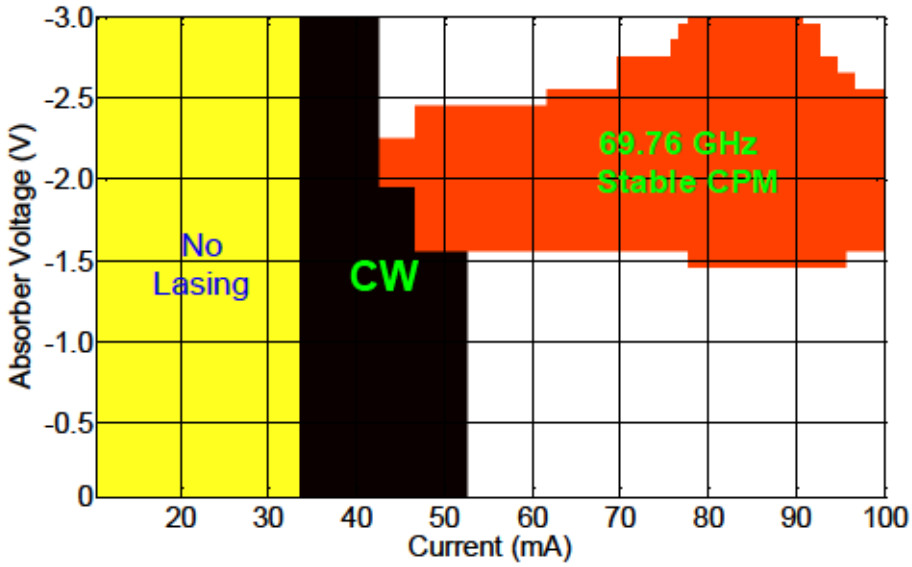

Figure 5.15. Measured map of the colliding pulse mode-locked regimes of Dev_B working at 69.76 GHz.

Table 5.2 summarizes all the measurements performed in the devices that were fabricated in the SMART Photonic multi-project wafer (MPW) run by using the same methodology of bias conditions (I_{SOA} and V_{SA}) for the characterization of the devices. For both devices, the gain section is biased at I_{SOA} = 80 mA, the saturable absorber is reverse biased at V_{SA} = -1.7 V and the temperature is stabilized at 16 °C by a thermoelectric cooler (TEC) and thermistor. The collected parameters provide the values of the fundamental frequency (FF), second harmonic frequency (SHF), spectral

width ($\Delta\nu$), second harmonic beating linewidth ($\Delta\nu_{RF2}$), shortest pulse width ($\Delta\tau$), time bandwidth product (TBP), lowest timing jitter (σ_T) and amplitude noise (N_{AM}). From the comparison of the parameters among the samples that were fabricated in the SMART Photonics multi-project wafer run, we have experimentally demonstrated the pulse width $\Delta\tau$ = 1.2 ps, timing jitter σ_T = 2.2 ps and amplitude noise N_{AM} = 0.012 dBc at 37 GHz (36.94 GHz) repetition rate frequency, while for the 70 GHz (69.76 GHz) we achieved a pulsed train with the pulse width $\Delta\tau$ = 1.27 ps, timing jitter σ_T = 1.2 ps and amplitude noise N_{AM} = 0.027 dBc.

	Measured Parameters							
Devices	*FF (GHz)*	*SHF (GHz)*	*$\Delta\nu$ (GHz)*	*$\Delta\nu_{RF2}$ (KHz)*	*$\Delta\tau$ (ps)*	*TBP*	*σ_T (ps)*	*N_{AM} (dBc)*
Dev_A	18.47	36.94	404.8	343	1.2	0.49	2.2	0.012
Dev_B	34.88	69.76	345.8	391	1.27	0.44	1.2	0.027

Table 5.2. Measurements performed in the devices fabricated in the SMART Photonics MPW run.

5.5 Conclusions

- We present novel on-chip colliding pulse mode-locked for mmW generation. These devices are versatile sources for high quality generation of ultra-short optical pulses at millimeter wave frequency repetition rates (30 to 300 GHz).
- The designs were contrasted through simulation and experimental processes. The agreement between the simulation and experimental results allow approving the design criteria obtained from previous reports which allows guiding the development of new devices.
- The simulation and experimental results have shown that colliding pulse mode locking are able to provide sub-picosecond pulses close to the Fourier transform limit as stated in previous reports. We have reached pulse widths as short as $\Delta\tau = 0.64$ ps with timing jitter, $\sigma T = 1.1$ ps, and amplitude noise $N_{AM} = 0.012$ dBc.
- The devices also have been fabricated in a multi-project wafer service provided by SMART Photonics, using an active/passive technology generic foundry which allows accessing the generic technologies for integrated photonics (GTIP) and reduces costs.

5.6 References

[1] K. A. Williams, M. G. Thompson, and I. H. White, "Long-wavelength monolithic mode-locked diode lasers," *New J. Phys. A*. vol. 6, no. 179, pp. 1 – 31, 2004.

[2] A. Stohr, S. Babiel, P. J. Cannard, B. Charbonnier, F. van Dijk, S. Fedderwitz, D. Moodie, L. Pavlovic, L. Ponnampalam, C. C. Renaud, D. Rogers, V. Rymanov, A. Seeds, A. G. Steffan, A. Umbach, and M. Weiss, "Millimeter-wave photonic components for broadband wireless systems," *IEEE Trans. Microwave Theory Tech.*, vol. 58, no. 11, pp. 3071–3082, 2010.

[3] Y. K. Chen, M. C. Wu, T. Tanbun-Ek, R. A. Logan, and M. A. Chin, "Subpicosecond monolithic colliding-pulse mode-locked multiple quantum well lasers," *Appl. Phys. Lett.*, vol. 58 no. 12, pp. 1253–1255, 1991.

[4] Chen, Y. K., & Wu, M. C, "Monolithic colliding-pulse mode-locked quantum-well lasers," *IEEE Journal of Quantum Electronics*, vol. 28, no. 10, pp. 2176-2185, 1992.

[5] M. G. Thompson, A. R. Rae, M. Xia, R. V. Penty, and I. H. White, "InGaAs quantum-dot mode-locked laser diodes," *IEEE J. Sel. Top. Quantum Electron.*., vol. 15, no. 3, pp. 661-672, 2009.

[6] K. Merghem, A. Akrout, A. Martinez, G. Moreau, J. P. Tourrenc, F. Lelarge, F. Van Dijk, G. H. Duan, G. Aubin, and A. Ramdane, "Short pulse generation using a passively mode-locked single InGaAsP/InP quantum well laser," *Opt. Express*, vol. 16, no. 14, pp. 10675-10683, 2008.

[7] K. Sala, G. Kenney-Wallace, and G. Hall, "CW autocorrelation measurements of picosecond laser pulses," *IEEE J. Quantum Electron*., vol. 16, no. 9, pp. 990-996, 1980.

[8] D. von der Linde, "Characterization of the noise in continuously operating mode-locked lasers," *Appl. Phys., A Mater. Sci. Process.*, vol. 39, no. 23, pp. 201–217, 1986.

[9] H. C. Bao, H. F. Liu, and Y. J. Wen, "Amplitude noise of 40-GHz pulses from a subharmonically synchronous mode-locked semiconductor laser," *IEEE Photonics Technol. Lett.*, vol. 14, no. 4, pp. 540- 542, 2002.

[10] K. Yvind, D. Larsson, L. J. Christiansen, J. Mørk, J. M. Hvam, and J. Hanberg, "High-performance 10GHz all-active monolithic mode locked semiconductor lasers," *Electron. Lett.*, vol. 40, no. 12, pp. 735–736, 2004.

[11] G. Carpintero, M. G. Thompson, R.V. Penty, and I.H. White, "Low noise performance of passively mode-locked 10-GHz quantum-dot laser diode," *IEEE Photonics Technol. Lett.*, vol. 21, no. 6, pp. 389–391, 2009.

Chapter 6

On-chip Multiple Colliding Pulse Mode-Locked Laser Structure

6.1 Introduction

The generation of increasingly higher frequencies, reaching the upper end of the Millimeter-wave range (MMW, 30 to 300 GHz) and into the Terahertz-wave (THz, 300 to 3000 GHz) has various applications, among them increasing the data bandwidth in wireless communications [1]. Recent experimental results reported data rates up to 48 Gbps on a 300 GHz carrier frequency [2]. As we previously discussed, various photonic techniques have been proposed which enable the generation of MMW and THz frequencies. It has been recently reported that pulsed techniques, usually based on mode locked laser structures [3], can increase the emitted power about 7 dBm above optical heterodyning schemes [4].

However, reaching the millimeter-wave range (100 GHz) means to reduce the cavity length down to 415 μm. Taking into account the size of the MIR integrated mirrors, 90.3 μm each, it becomes very challenging to push the repetition rate frequency beyond this value. Another challenge, as the repetition rate frequency increases, is to operate the device in a hybrid regimen, locking the repetition rate to an electronic reference to reduce the phase noise fluctuations of the passive mode-locking [5]. One of the problems is that the electrical modulation bandwidth is usually limited below 30 GHz [6].

In order to overcome the modulation frequency limit, and enable an electronic reference to lock a mode-locked device operating at MMW and THz repetition rate frequencies, harmonic mode-locked (HML) can be used. HML regime is achieved when the mode-locked device operates at higher repetition rate which is a multiple of the fundamental repetition rate [7]. In order to achieve HML, the mode locked laser

structure is composed of one or more saturable absorber sections (SAs) strategically located along the cavity length (Lcav), as well as semiconductor optical amplifier (SOA) sections [8],[9]. It is important to recall that in mode-locked laser structures, the key requirements are the location of the SA sections and the interplay between SOA and SA sections, which have been extensively studied [5].

From the previous discussion of the cavity configuration of monolithic mode-locked laser structures in chapter 2, we are able to consider the HML structures which are capable to provide higher harmonic from the fundamental repetition rate. Higher harmonic than the second one have been achieved through symmetric and asymmetric colliding pulse mode-locked geometries. On one hand, repetition rates at 192 GHz [10], 240 GHz [11] and 377 GHz [12] were obtained with the symmetric colliding geometry. These structures were realized with one or more SAs located at multiples of an integer fractional position L_{cav}/N of the cavity length, where N is the Nth harmonic of the round trip frequency. The structures which provide either the N = 3 or N = 4 harmonic are termed multiple colliding pulse mode-locked (mCPM). Figure 6.1(a) and Figure 6.1(b) depict the mCPM structures with just one SA and multiple SAs, respectively.

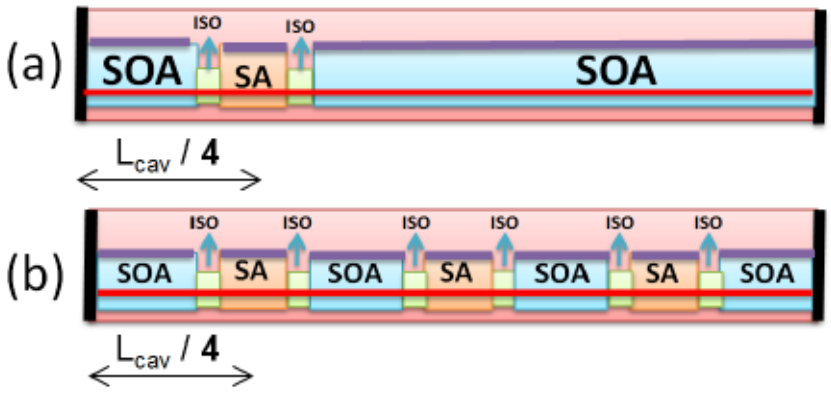

Figure 6.1. Multiple colliding pulse mode-locked structures, L_{cav}/N. (a) Single SA. (b) Multiple SA.

On the other hand, higher repetition rates up to 860 GHz [13] with the N = 12 harmonic has been reached with a single SA situated at the position $M \cdot L_{cav}/N$ of the cavity length, where M and N are relative prime (M<N). Figure 6.2 sketches the HML structure with SA located at $M \cdot L_{cav}/N$ position within the resonator cavity, which is named asymmetric colliding pulse mode-locked. In all of the reported structures [10], [11], [12], [13] cleaved facet mirrors were used to define the resonator cavity length so the transmitted light is no longer available on-chip avoiding any integration of additional functionalities. The cleaving process becomes a critical step, as the tolerances that it introduces on the location of the facet mirrors have an impact on the position of the SA sections along the cavity [14]. In order to elude cleaved facet mirrors, two main approaches have been proposed to integrate mode-locked laser diodes on-chip as explained in chapter 3 of the present thesis.

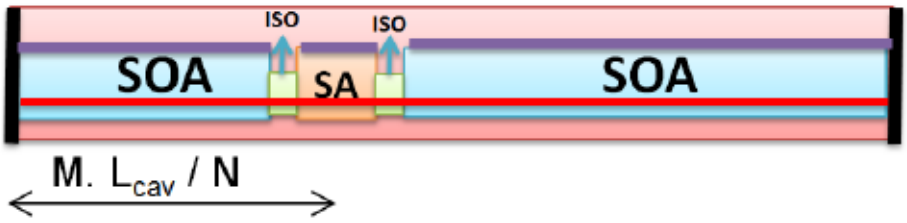

Figure 6.2. Asymmetric colliding pulse mode-locked structure, $M \cdot L_{cav}/N$, M and N are relative prime (M<N)

6.2 Novel On-Chip Multiple Colliding Pulse Mode-Locked Laser

In this section, we present the multiple colliding pulse mode-locked (oc-mCPM) laser diode structure, in which multiple SA sections are introduced within a cavity defined by multimode interference reflectors. To the best of our knowledge, this is the

first time such a structure is proposed to increase the repetition rate of the pulses within a photonic chip.

This approach presents the advantage that in multiple colliding structures the accurate positioning of the SA is critical. On-chip reflectors, which avoid the cavity length uncertainty drawback of monolithic structures using cleaved facets, allow to the accurate positioning the saturable absorber at a quarter of the resonator cavity (¼ L_{cav}) to increase the repetition rate four times over the fundamental. A second SA, at the center of the resonator (½ L_{cav}) is also introduced to enhance this operating regime [6]. With this combination of SAs, we demonstrate that the repetition rate can be increased without decreasing the cavity length, as there is an effective limit to the smallest cavity length in order to ensure lasing [15]. The fundamental repetition rate frequency (FF) is 25 GHz, and its fourth harmonic frequency (FHF) is 100 GHz which is already within the F-Band of millimeter-wave spectrum (90 – 140 GHz).

The oc-mCPM was realized as an extended cavity laser in a photonic integrated circuit with active-passive integration technology. The advantage of this approach is that allows including additional components in order to provide advanced functionality and/or performance [16]. The sample was developed with the current InP photonic generic integration technology and fabricated by the SMART Photonics through a commercial MPW run as the aforementioned devices in chapters 3, 4, and 5.

The structure of the on-chip multiple colliding pulse mode-locked laser diode is sketched in Figure 6.3(a). The oc-mCPM´s assembly includes three semiconductor opti1cal amplifiers (Lengths, $L_{SOA\ 1}$ = 182 um, $L_{SOA\ 2}$ = 348 um and $L_{SOA\ 3}$ = 350 um), two saturable absorbers (Lengths, $L_{SA\ 1/2} = L_{SA\ 1/4}$ = 20 um) with four electrical isolators (Lengths, L_{ISO} = 20 um each) located on each side of the SAs as well as passive

waveguides (L_{PW} = 451.4 um) and two multimode interference reflectors on each end in order to build the resonator cavity. The optical output was 7° angled with respect to the cleaved and AR-coated facet in order to minimize back reflections from the edges of the chip. The total length of the cavity is L_{cav} = 1632 um which offers a fundamental repetition rate frequency of FF = 25 GHz. With the intention of preserving the symmetry required for colliding operation [5], two ports MIR mirrors were used on both ends of the oc-mCPM. As an added value, a boost semiconductor optical amplifier (L_{Boost} = 400 um) was integrated on-chip at one optical output with the aim of increasing the amount of the optical power delivered by the oc-mCPM. Besides, the microscope photograph of the fabricated sample is shown in Figure 6.3(b).

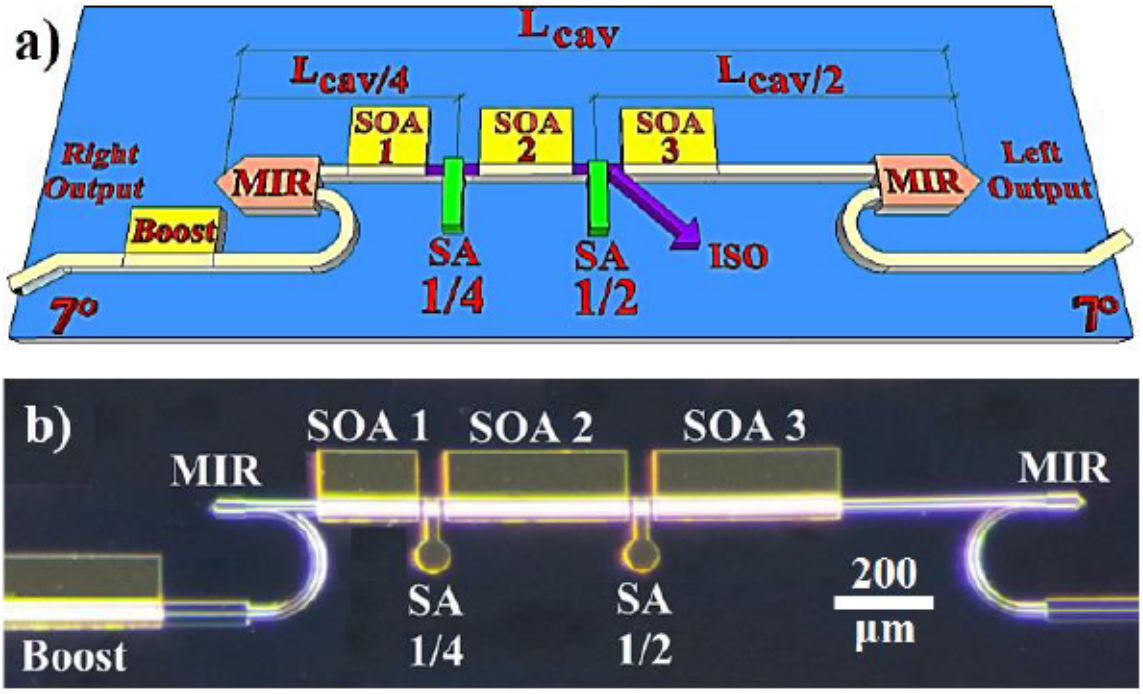

Figure 6.3. (a) Schematic of the oc-mCPM structure. (b) Microscope photograph of the oc-mCPM. Fourth harmonic, $L_{cav}/4$ (where L_{cav} is the Fabry-Perot cavity length).

The component lengths of the oc-mCPM are summarized in Table 6.1, which also includes the design criteria used in order to achieve stable multiple colliding pulse mode-locked regimes.

Component Lengths (um)							Repetition Rate (GHz)		Design Criteria		
MIR	SOA 1	SOA 2	SOA 3	SA	PW	L_{cav}	FF	FHF	Rule 1 L_{SA}/L_{cav}	Rule 2 L_{SOA}/L_{SA}	Mode-Locked Regime
90.3	182	348	350	20	1229.4	2210	25	100	≈ 1 %	$L_{SOA\,1}/L_{SA}$ ≈ 10 times $L_{SOA\,2}/L_{SA}$ ≈ 18 times $L_{SOA\,3}/L_{SA}$ ≈ 18 times	Stable

Table 6.1. Table Component lengths and design criteria of oc-mCPM

6.3 Simulation Stage of oc-mCPM

For the simulation of oc-mCPM using FreeTWM software, the material parameters were the same used before in the study of the saturable absorber length optimization of on-chip colliding pulse mode-locked laser in chapter 4. The structure of the oc-mCPM required for the simulation in FreeTWM software is shown in Figure 6.4. We have the three SOA sections, two SAs located at quarter and half of the cavity length, and passive sections. The reflectivity at both facets was set at 50 % which is the reflectivity provided by the two ports MIR. The bias setting in order to obtain multiple colliding pulse mode-locked regimes was at injected carrier rate $J_{(ZJ)SOA} = 200.e^{8}s^{-1}$ which is around three times the threshold current rate required in the FreeTWM software, we consider applying three times the threshold current due to the fact that in the experimental results we forward bias the all the SOAs with a total current around three

times the threshold current. Also, the absorber section works in the regime of slow saturation so the absorber recovery time is $\tau_{SA} =$ 10 ps. We would like to highlight that the oc-mCPM was designed considering the design rules aforementioned in chapter 4, so the lengths of the gain and absorber sections meet the design criteria in order to obtain stable multiple colliding pulse mode-locked regimes.

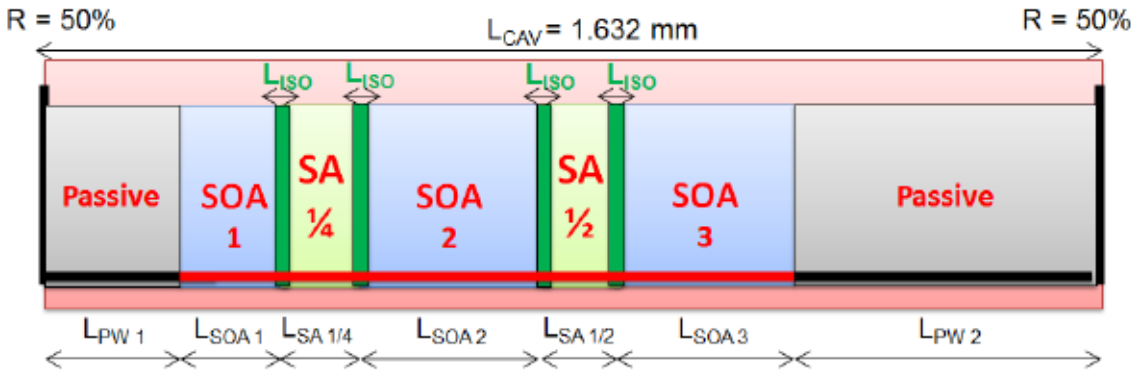

Figure 6.4. (a) Structure of the oc-mCPM for simulation with FreeTWM.

From the simulation of the oc-mCPM we obtain the profiles for the optical power, electrical field intensity, and carriers concentration against discretized length are shown in Figure 6.5(a), Figure 6.5(b), and Figure 6.5(c), respectively. All the profiles were obtained after 1500 single trips in the cavity and the discretized length is 1105 points. In Figure 6.5(a) we observe four pulses circulating within the cavity while in Figure 6.5(b) we appreciate the four electrical fields which coexist within the cavity. Besides, the amount of carriers concentrated in SOA sections is depicted in Figure 6.5 (c).

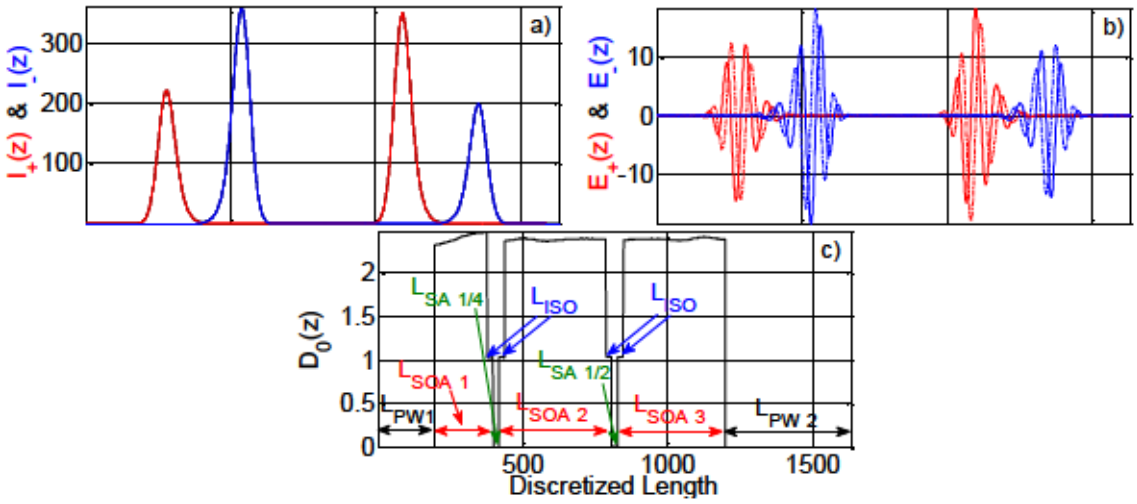

Figure 6.5. Profiles of the oc-mCPM, delivered by FreeTWM. (a) Optical power. (b) Electrical field intensity. And (c) Carriers concentration.

6.3.1 Frequency Spectrum Simulation Results

Optical Spectrum Results

The optical spectrum of the oc-mCPM bias at multiple colliding pulse mode-locked regime is depicted in Figure 6.6. The simulation result of the optical spectrum is evaluated in terms of symmetry, optical mode spacing and side mode suppression ratio. We observe the Gaussian shape around peak, the fundamental optical mode spacing at 25 GHz and the fourth harmonic optical mode spacing at 100 GHz while the side mode suppression ratio is around 30 dBm. The estimated spectral width of the oc-mCPM from the simulated optical spectrum through a Gaussian fitting is $\Delta v = 400$ GHz .It is important to highlight that the design of the oc-mCPM meets the design criteria of mode-locked lasers aforementioned in chapter 4. So the designed on-chip multiple colliding pulse mode locked laser is capable to generate stable mode-locked regimes.

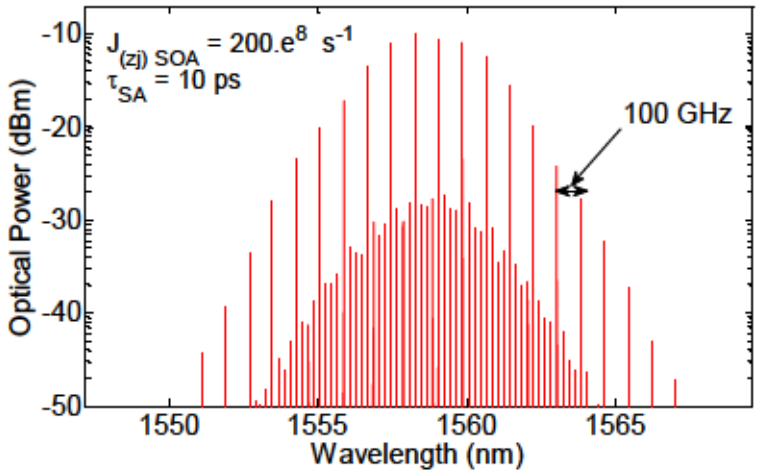

Figure 6.6. Optical spectrum of the oc-mCPM simulated in FreeTWM.

Electrical Spectrum Results

The electrical spectrum of the oc-mCPM at the multiple colliding pulse bias settings is sketched in Figure 6.7(a). The simulated result discloses that the oc-mCPM works on multiple colliding pulse-mode locking regime due to the fact that the we observe the fourth harmonic tone at 100 GHz while, the fundamental, second and third harmonic at 25 GHz, 50 GHz, and 75 GHz are attenuated more than 30 dBm from the fourth harmonic, respectively. From the literature a mode locking regime is observed in the electrical spectrum when electrical tone of the repetition rate frequency provided by the mode locked laser is over 25 dBm over any other tone in the spectrum [17]. The estimated beating linewidth using a Lorentzian fitting of the fourth harmonic frequency tone in the simulated electrical spectrum is $\Delta v_{RF} =$ 3.60 MHz.

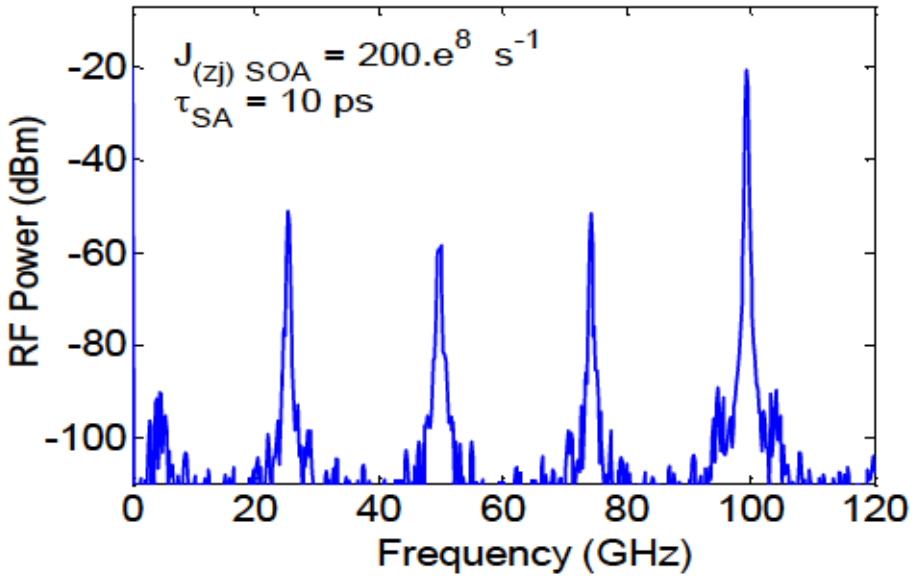

Figure 6.7. Electrical spectrum of the oc-mCPM simulated in FreeTWM.

6.3.2 Optical Pulse Results

The pulse train is evaluated in terms of stability, and the time between pulses. The stability is estimated in the pulse train obtained from the simulation of the oc-mCPM at 40 ns span which is shown in Figure 6.8(a). We observe stability due to we have a flat pulse train and there is not amplitude variation of the pulse train. The time between pulses is estimated and depicted in Figure 6.8 (b) which shows the pulse train of the oc-mCPM at 50 ps span. We estimate that the time between pulses is 10 ps, which corresponds to the repetition rate of 100 GHz.

Furthermore, Figure 6.8(c) sketched the pulse width of the simulated oc-mCPM. The pulse width was estimated using the hyperbolic secant pulse shape fitting. The pulse width obtained was $\Delta\tau_{\mathbf{Dev\_A}} = 1.5\,ps$ and considering the estimated spectral width of $\Delta v = 400\,GHz$ from the optical spectrum Gaussian fitting, the FreeTWM

allows predicting a time bandwidth product of TBP = 0.60 which is close to the transform limit hyperbolic secant pulses.

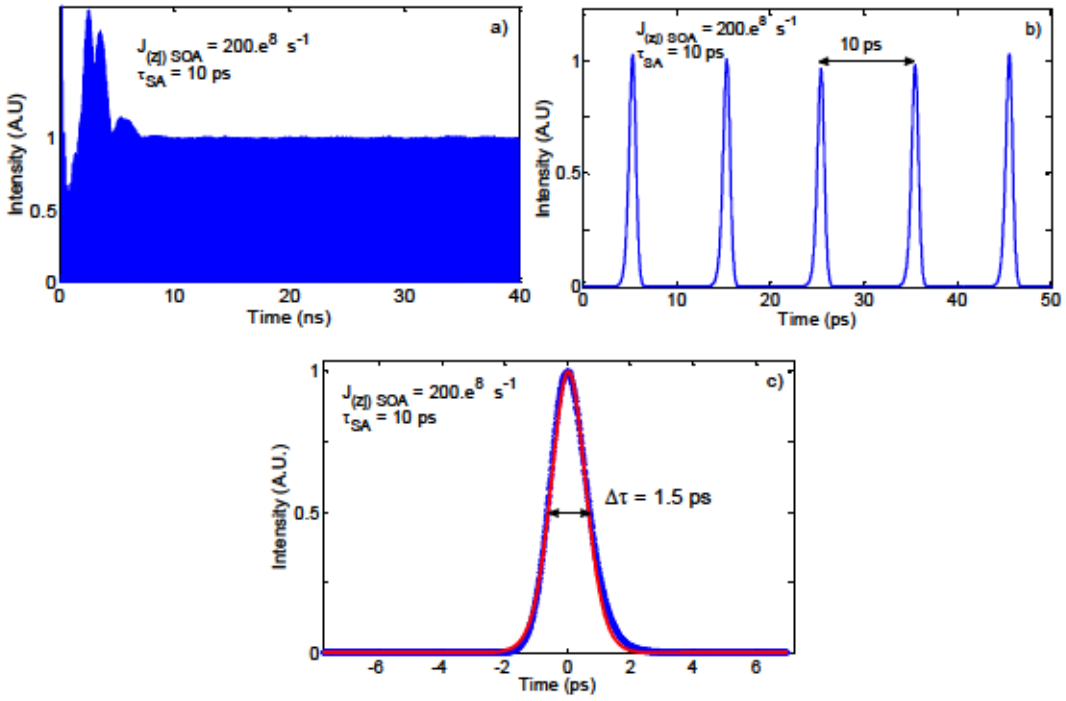

Figure 6.8. a) Pulse train, 40 ns span. b) Pulse train, 50 ps span. c) Pulse width.

6.4 Experimental Setup

The characterization of the oc-mCPM was carried out by using the set-up depicted in Figure 6.9, in which the oc-mCPM was mounted on a copper chuck that was temperature stabilized at 17 °C by a thermoelectric cooler (TEC) and thermistor. The chip was biased by the direct current needles available on a Wentworth Laboratories PML 8000 probe station, while the SOA sections were biased with a Thorlabs PRO 8000 laser diode controller and the SA sections were reverse biased by an Agilent E3631A voltage source.

The optical pulses emitted from the angled facet of the oc-mCPM were coupled into an anti-reflection coated lensed fiber (LF), and then passed through an optical isolator (OI) with the intention of preventing back-reflections to the chip from optical equipment connected to the fiber. A 90/10 splitter was connected in order to divide the optical pulses in two branches. The 10% branch allowed the optical power measurement all the time by a Newport 842-PE power meter (PM). The other 90% branch was used to perform an optical and electrical characterization of the signal.

The optical spectrum was recorded with a Yokogawa AQ6370B optical spectrum analyzer (OSA, resolution 0.02 nm). The optical pulses were previously amplified on a Nortel FA14UFAC telecom erbium doped fiber amplifier (EDFA).

The characterization of the RF beat signal was carried out with an Anritsu electrical spectrum analyzer (ESA) previously connected to a 90 GHz -3 dB bandwidth U2T XPDV4120R PIN-photodiode (PD) which offers the optoelectronic conversion, followed by an external mixer (MXR) Rohde & Schwarz FS-Z110 (RF range from 75 to 110 GHz), which down-convert the signal frequency because of the ESA's frequency range available is from 20 KHz to 40 GHz and it is out of the repetition rate of the oc-mCPM (100 GHz). Also, a Rohde & Schwarz FSV40 signal and spectrum analyzer with the FS-Z110 external mixer enabled the phase noise characterization.

An APE pulse-check auto-correlator (AC) allowed the pulse autocorrelation measurement previously connected to a 4.6 m dispersion compensating fiber (DCF) and a polarization controller (PC). The 4.6 m of DCF prevented the pulse broadening provided by the 10 m standard single mode patch fibers (dispersion coefficient = 17 ps/nm/km) used in the set-up.

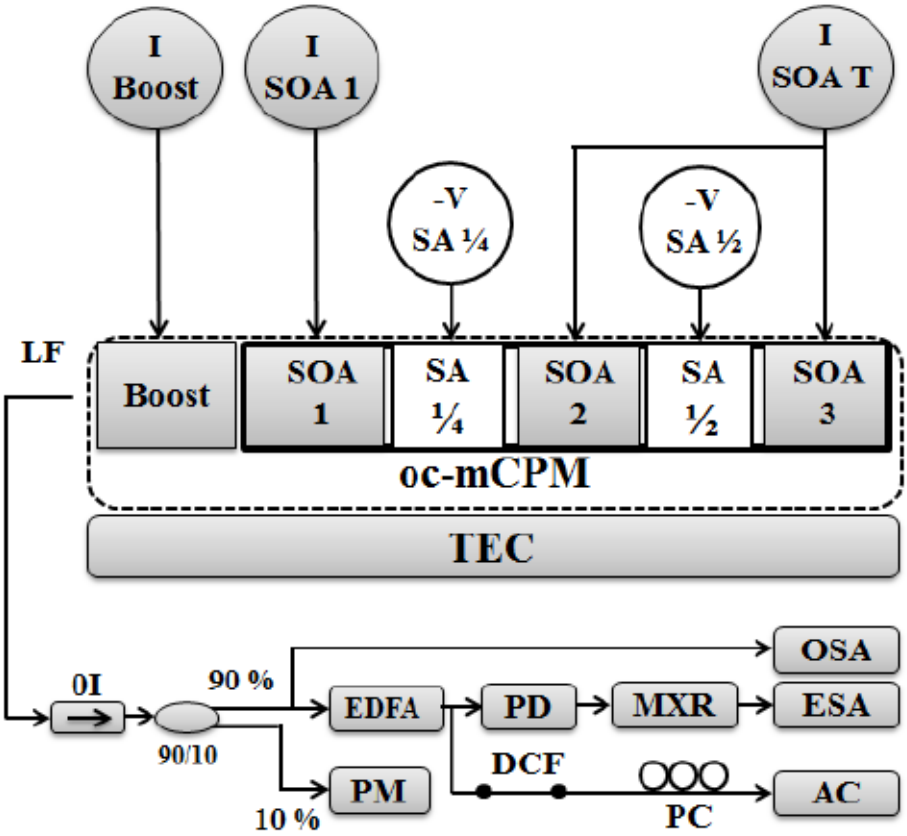

Figure 6.9. Experimental set-up. I: Current source, -V: reverse bias voltage, TEC: thermoelectric cooler.

6.5 Optical Power Characteristics

The optical power coupled onto the lensed fiber versus current intensity P-I curves of the oc-mCPM are depicted in Figure 6.10(a), recorded when the common current applied $I_{SOA\ T}$ (shared current between $I_{SOA\ 2} = I_{SOA\ 3}$) is swept from 0 to 80 mA, with a fixed current applied to the $I_{SOA\ 1}$ = 7 mA, a fixed saturable absorber reverse voltages $V_{SA\ 1/2}$ = -2.3 V and $V_{SA\ 1/4}$ = -2.0 V, at three different values of the SOA boost current (I_{Boost} = 15 mA, 25 mA and 35 mA) and without the use of the SOA boost taken from

the two optical outputs available on-chip. A threshold current of 22 mA is observed for each I_{Boost} value and it allows establishing that the SOA boost does not change the performance of the oc-mCPM. Also, Figure 6.10(a) shows the amount of optical power around 1.2 mW and 0.12 mW at 80 mA bias current with and without the SOA boost (I_{Boost} = 35 mA) respectively. The comparison of both optical powers reveals that the optical power has been increased around ten times thanks to the SOA boost. Considering a representative link budget calculation for a THz wireless transmission link [1], the expected output power needs to reach at least 0 dBm (1 mW). The boost SOA included in the PIC has been demonstrated to exceed this requirement.

Further, the optical signal being available on-chip will allow photonic signal processing operations (modulation, optical filtering, pulse rate multiplication, and so on) on-chip. Besides, Figure 6.10(b) depicts the evolution of the optical spectrum of the oc-mCPM at the same bias conditions that the P-I curve was recorded when setting the I_{Boost} = 25 mA. By relating, the two plots, we identify two different regimens of operation. From threshold to 33 mA, the oc-mCPM delivers continuous wave (CW), exhibiting lasing on few modes. From 34 mA to 80 mA the device reaches a multiple colliding pulse mode-locked (mCPM) regime. Likewise, the parallel horizontal lines in Figure 6.10(b) depict the optical modes which are detached at $\Delta v = 0.80$ nm = 100 GHz.

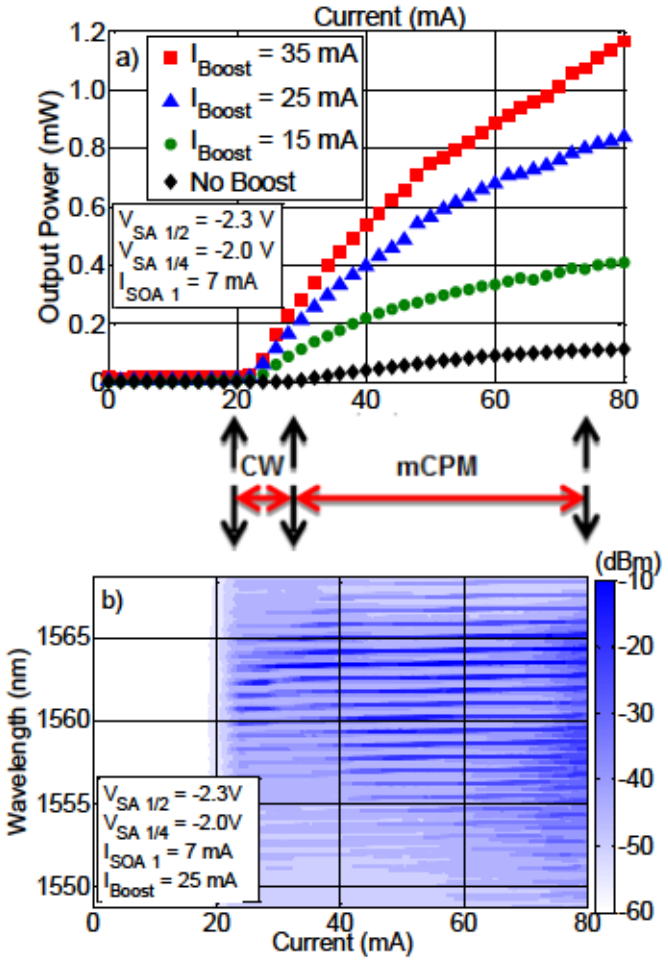

Figure 6.10. (a) Optical power versus injection current (P-I curve) of the oc-mCPM. (b) Evolution of the optical spectrum. Identified regions are CW: continuous-wave, mCPM: multiple colliding pulse mode-locked

6.6 Optical Spectrum Characterization

The mCPM regime of the oc-mCPM was characterized by choosing a bias condition, which exhibits this behavior, at a gain sections currents $I_{SOA\ 1}$ = 7 mA, $I_{SOA\ T}$ = 42 mA (shared current between $I_{SOA\ 2}$ = $I_{SOA\ 3}$), I_{Boost} = 25 mA, fixed saturable absorber reverse voltages $V_{SA\ 1/2}$ = -2.3 V and $V_{SA\ 1/4}$ = -2.0 V. We will refer to these bias settings as multiple colliding bias (MCB) settings. The recorded optical spectrum

for oc-mCPM is depicted in log and linear scales in Figure 6.11(a) and Figure 6.11(b) respectively. The inset double arrow in Figure 6.11(a) shows the 100 GHz optical mode spacing. The side mode suppression ratio (SMSR) between the fundamental optical mode spacing (25 GHz) to the multiple colliding mode spacing (100 GHz) is 35 dBm. The central emission wavelength is 1558.7 nm, and the estimated full-width half-maximum (FWHM) is Δv = 2.90 nm (364 GHz) obtained from the Gaussian fitting (continuous line) of the optical spectrum in the linear scale sketched in Figure 6.11(b).

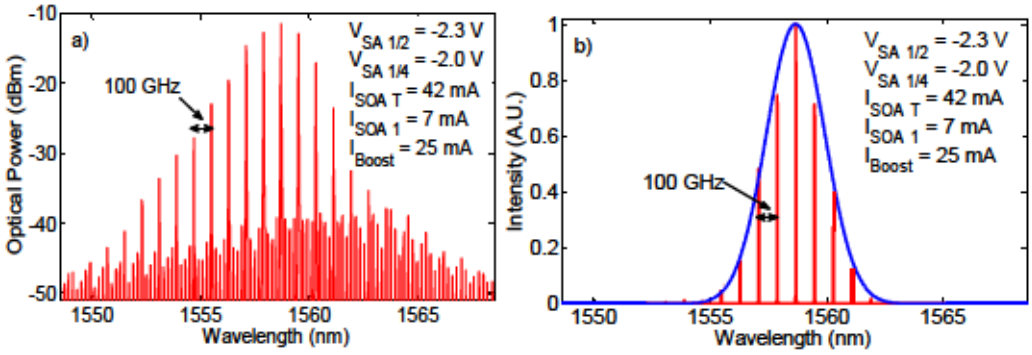

Figure 6.11. (a) Optical spectrum log scale of the oc-mCPM. The inset double arrow shows the frequency mode spacing at 100 GHz, resolution 0.02 nm, span 20 nm. (b) Optical spectrum linear scale of the oc-mCPM.

6.7 Electrical Spectrum Characterization

Moreover, the electrical characterization was carried out at the MCB settings. The electrical mode beating tone at 405 MHz is delivered by the Rohde & Schwarz FS-Z110 external mixer head working with the tenth harmonic which down converts the 100 GHz repetition rate of the oc-mCPM in order to measure in the available ESA. Figure 6.12(a) shows the recorded electrical spectrum of the mode beating provided by the oc-mCPM at the multiple colliding pulse mode-locked regime with span 100 MHz,

resolution bandwidth RBW = 100 KHz and video bandwidth VBW = 10 KHz. The electrical beating linewidth (dotted line) and its fit to a lorentzian line-shape (continuous line) for the down converted electrical signal provided by the oc-mCPM are depicted in Figure 6.12(b) with span 20 MHz, resolution bandwidth RBW = 100 KHz and video bandwidth VBW = 10 KHz . The estimated beating linewidth at -3 dB of the down converted 100 GHz repetition rate is Δv_{RF} = 1.1 MHz taken from the lorentzian fitting. The usefulness of a carrier signal is defined by the linewidth so it is necessary to take into account the linewidth requirements for THz data transmission systems. We can state that the linewidths around MHz are useful for direct envelop detection methods [18]. But, when we use coherent detection we have to consider the MHz linewidth limitation [19], due to the fact that lower linewidths are required for higher order modulation schemes. We are on further studies in order to decrease the linewidth of the oc-mCPM by using hybrid structures for higher order modulation coherent detection systems.

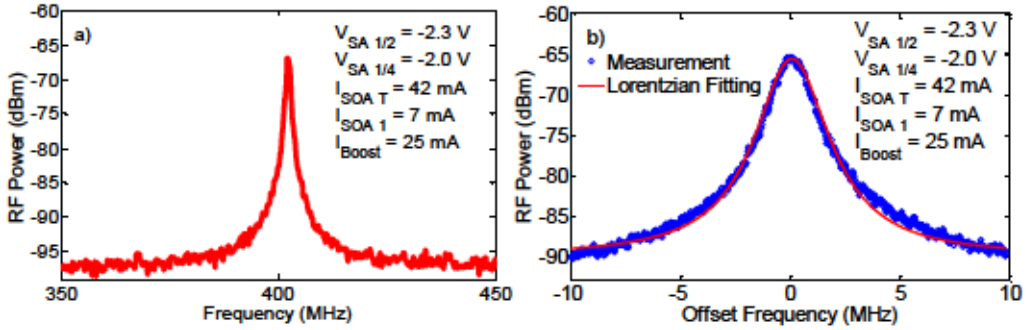

Figure 6.12. (a) Electrical spectrum of the oc-mCPM at multiple colliding pulse mode-locked regime, 100 MHz span, (b) Colliding beating linewidth, 20 MHz span.

6.8 Pulse Characterization

The APE Pulse-Check autocorrelator allowed performing the pulse autocorrelation of the optical pulses provided by the oc-mCPM. The measurement of the pulse width evolution reliant on the gain current and reverse absorber voltages was also carried out. On one hand, the pulse width evolution when $I_{SOA\ T}$ is varied from 40 mA to 80 mA, while the rest of the parameters remain at the MCB settings, is shown in Figure 6.13(a). The results disclose a linear dependence of the pulse width vs. gain current as theoretically demonstrated in a previous report [5] and the pulse width data depicted by squares is fitted to a linear continuous line. Also, in Figure 6.13(a), we introduce the results about the time bandwidth product (TBP), showing the measured data with circles, which is fitted to a linear trace (dashed line). On the other hand, the pulse width evolution when $V_{SA\ 1/4}$ is varied from -1.7 V to -2.9 V and $V_{SA\ 1/2}$ changes from -2.0 V to -3.2 V simultaneously, while the rest of the parameters remain at the MCB settings, is shown in Figure 6.13(b). In this case, the results reveal an exponential dependence of the pulse width vs. reverse absorber voltages as theoretically demonstrated in a previous report [5] and the pulse width data sketched by squares is fitted to an exponential continuous line. At the same time, the results about the TBP vs. the reverse absorber voltages are shown in Figure 6.13(b), the measured data is depicted with circles, which are fitted to a linear trace (dashed line). Besides, at the MCB settings, the optical pulse train of the oc-mCPM recorded by the APE Pulse-Check autocorrelator in a period of 50 ps is depicted in Figure 6.13(c). The repetition rate of 100 GHz was confirmed by measuring the time delay between pulses which is 10 ps. In the same way, the pulse width provided by the oc-mCPM at the MCB settings is shown in Figure 6.13(d). The

pulse width of $\Delta\tau$ = 1.8 ps at the FWHM was estimated by a deconvolution of the hyperbolic secant pulse shape fitting and the time bandwidth product obtained was TBP = 0.6, closed to the Fourier transform limit hyperbolic secant pulses [20].

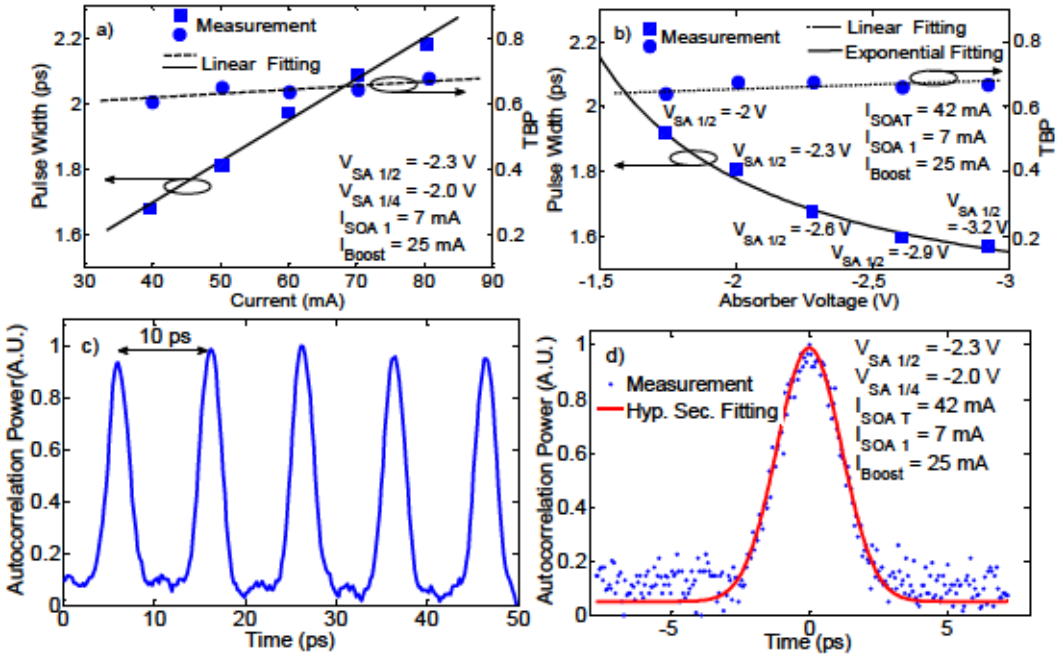

Figure 6.13. Optical pulse characterization: (a) Pulse width and TBP vs. gain section current level. (b) Pulse width and TBP vs. reverse absorber voltage. (c) Pulse train and (d) Optical pulse width.

6.9 Dependence of the Multiple Colliding Regime

As we already described, the device has two different SA sections, located at ½ and ¼ of the cavity length (L_{cav}). With the introduction of this SA at $L_{cav}/4$, the device now depends on five different variables, which are the currents on the three SOA and voltages of the two SA sections. As shown in Figure 6.9, we bias the device with two

currents and two voltages, on which the behavior depends.

In order to provide more detail on the dependence of the mCPM operating regime, we analyzed the optical spectrum and the electrical beat frequency varying the voltage of the SA section at $L_{cav}/4$. The bias conditions on the SOA sections and the voltage in the saturable absorber $L_{cav}/2$ are fixed to the MCB settings that we have just reported. We expect an enhancement of the electrical tone at 4x the fundamental repetition rate frequency as the voltage increases in negative value.

The results on Figure 6.14(a) to (n), show the optical and corresponding electrical spectrum, as the voltage on the SA section at $L_{cav}/4$ is swept from $V_{SA\ 1/4} = 0$ V to $V_{SA\ 1/4} = -3$ V. We observed from this data that the device always operates at the multiple colliding regime, as the optical modes are always spaced 0.80 nm (100 GHz), even at 0 V on the SA at $L_{cav}/4$. What we observed when the voltage of the SA section at $L_{cav}/4$ is varied, is a reduction of the electrical linewidth at -3 dB of the tone from $\Delta\nu_{RF} = 1.3$ MHz to $\Delta\nu_{RF} = 0.7$ MHz, decreasing as the voltages increases from $V_{SA\ 1/4} = 0$ V to $V_{SA\ 1/4} = -3$ V. This is in agreement with the trend reported for passive mode locking [21]. This linewidth reduction implies increasing the stability of the pulse train.

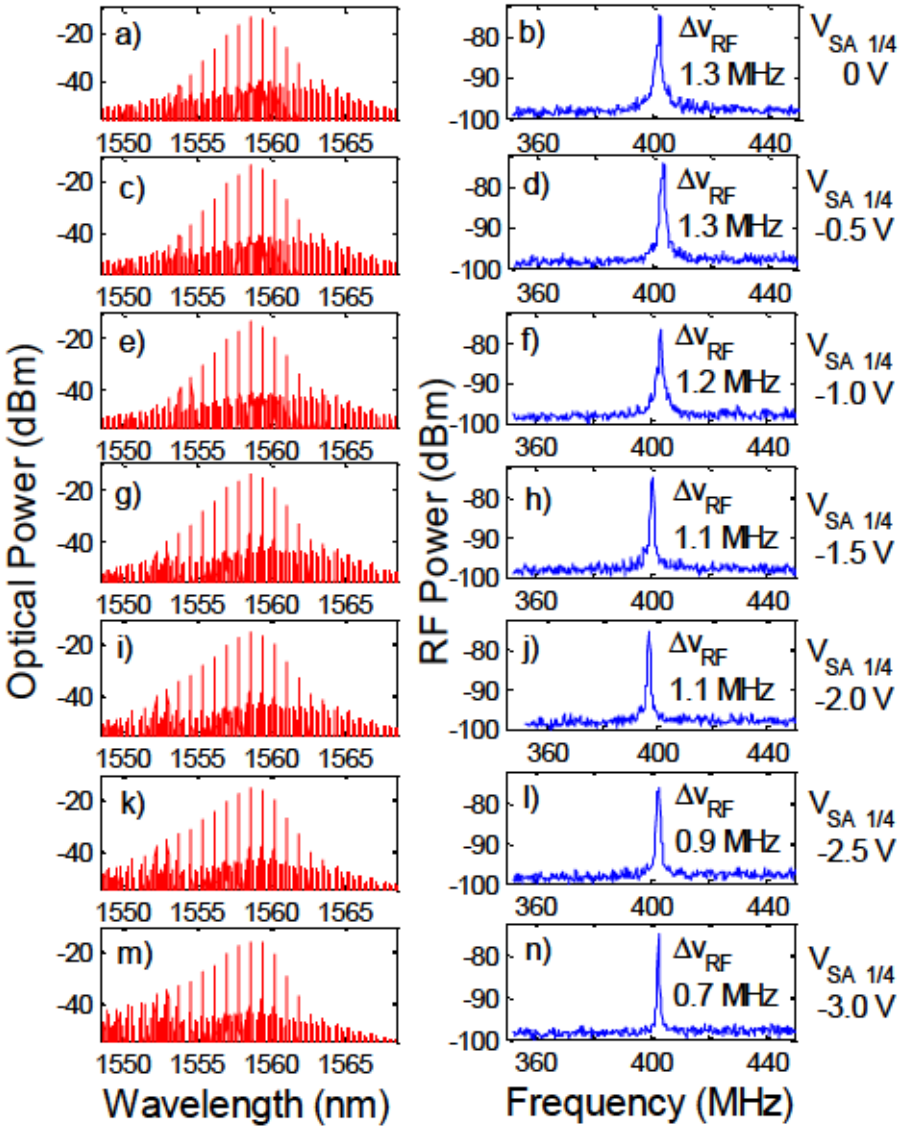

Figure 6.14. (a) - (n). Dependence of the multiple colliding pulse mode-locked regime while the voltage on the SA section at $L_{cav}/4$ is swept from $V_{SA\ 1/4} = 0$ V to $V_{SA\ 1/4} = -3$ V, and $V_{SA\ 1/2}$ is constant.

Besides, we examined the optical spectrum and the electrical beat frequency varying the voltage of the SA section at $L_{cav}/2$ while maintaining constant the voltage of the SA section at $L_{cav}/4$. The bias conditions on the SOA sections and the voltage in the saturable absorber $L_{cav}/4$ are fixed to the MCB settings that we have just reported. The results on Figure 6.15(a) to (n), show the optical and corresponding electrical spectrum, as the voltage on the SA section at $L_{cav}/2$ is swept from $V_{SA\ 1/2} = 0$ V to $V_{SA\ 1/2} = -2.8$ V.

We observe a few reduction of the electrical linewidth from $\Delta\nu_{RF}$ = 1.4 MHz to $\Delta\nu_{RF}$ = 1.1 MHz of the tone at 4x the fundamental repetition rate frequency as the voltage increases in negative value from $V_{SA\ 1/2}$ = 0 V to $V_{SA\ 1/2}$ = -2.3 V. The oc-mCPM always operates at the multiple colliding regime in this range, but when the $V_{SA\ 1/2}$ = -2.8 V, we detected a reduction of the RF power around 10 dBm and the beating linewidth increases to 2 MHz this effect is caused due to a small group of optical modes around 1552 nm are unlocked.

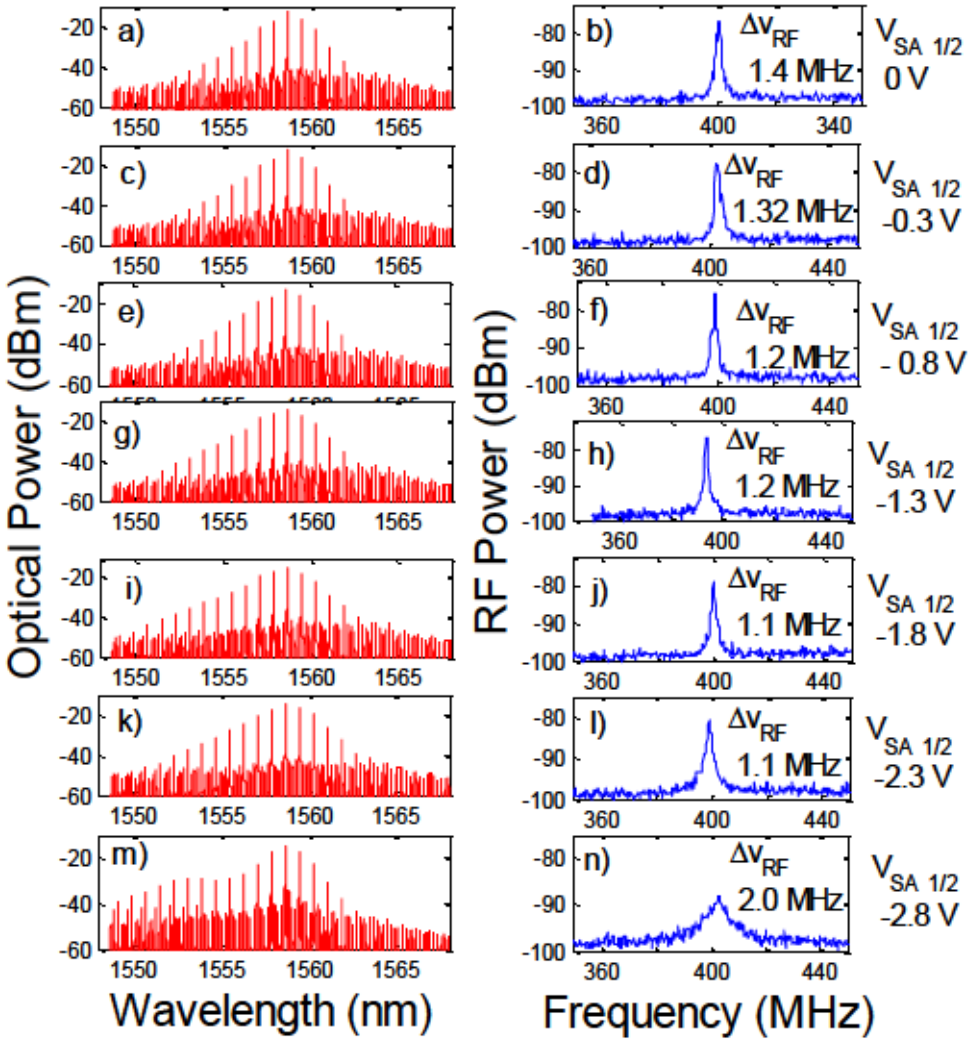

Figure 6.15. (a) - (n). Dependence of oc-mCPM while the voltage on the SA section at $L_{cav}/2$ is swept from $V_{SA\ 1/2}$ = 0 V to $V_{SA\ 1/2}$ = -2.8 V, and $V_{SA\ 1/4}$ is constant.

6.10 Operating Regimes Characterization

Figure 6.16 shows the map of the multiple colliding pulse mode- locked regime of the oc-mCPM working at 100 GHz. The stable multiple colliding pulse mode-locked regime depicted by the red area, was achieved for a wide range of bias settings when the forward bias current in the SOA sections are ranging from 34 mA to 80 mA and the reverse bias voltage on the SA section at $L_{cav}/4$ is swept from $V_{SA\ 1/4}$ = 1.5 V to $V_{SA\ 1/4}$ = -2.9 V while the reverse bias voltage on the SA section at $L_{cav}/2$ is swept from $V_{SA\ 1/2}$ = - 1.8 V to $V_{SA\ 1/2}$ = -3.2 V increasing in steps simultaneously. Besides, the degradable, deteriorated, poor, unstable and no existence of multiple colliding pulse mode-locked regime at 100 GHz is denoted by the white areas. The no lasing regime lower than the threshold current at 23 mA is depicted by the yellow area and the continuous wave regime is denoted by the black area when the forward bias current in the SOA sections are ranging from threshold current to 33 mA and the reverse bias absorber sections varying in the whole range within a 0 V to – 3.0 V.

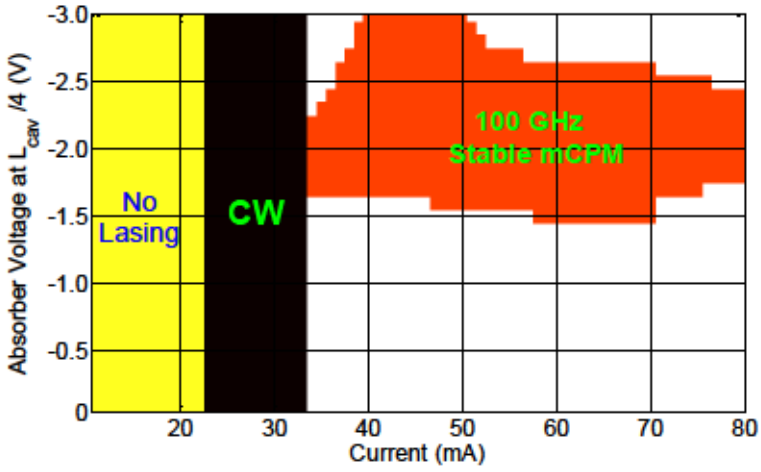

Figure 6.16. Measured map of the multiple colliding pulse mode-locked regime of the oc-mCPM working at 100 GHz as a function of forward bias current and the reverse bias voltage.

6.11 Stability Characterization

In order to provide further details on the stability, we measured the phase noise. Figure 6.17 depicts the single side-band phase noise (SSB - L(f)) of the oc-mCPM at the MCB settings. This measurement was achieved using a Rohde & Schwarz FSV40 Signal and Spectrum Analyzer with the FS-Z110 external mixer. The timing jitter, using the Von der Linde method [22] and using the International Telecommunications Union (ITU) recommended integration range [4-80 MHz] [23] results in σ_T = 1052 fs. We aim to reduce this value through a sub-harmonic hybrid mode-locked scheme.

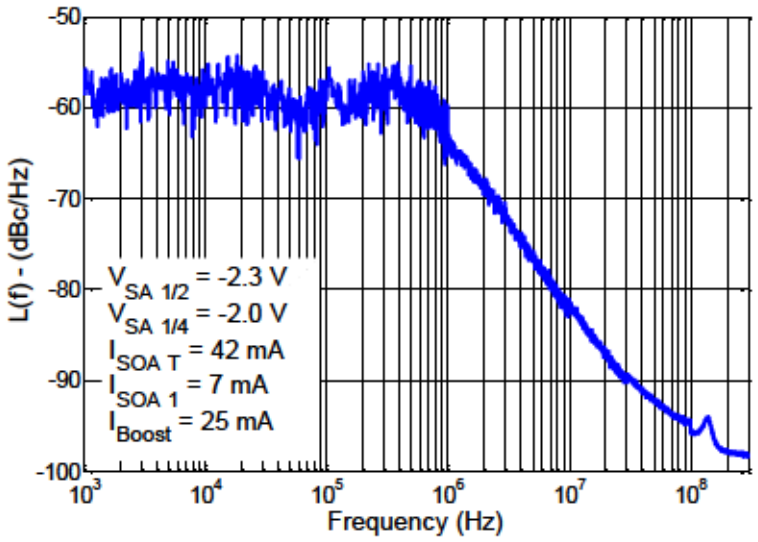

Figure 6.17. Phase Noise of the oc-mCPM, start frequency 1 KHz, stop frequency 300 MHz.

6.12 Conclusions

- We report an integrated multiple colliding pulse mode-locked semiconductor laser and we demonstrate that the structure operates at a repetition frequency of 100 GHz which is the fourth harmonic of the fundamental repetition rate at 25 GHz.
- This novel structure was fabricated by the SMART Photonics foundry service which uses a generic InP photonic integrated technology through a multi-project wafer (MPW) run.
- The oc-mCPM structure delivers the signal on the chip and we demonstrate that using additional components, such as a boost SOA, we can increase the available optical power at the chip output waveguide.

6.13 References

[1] A. J. Seeds, H. Shams, M. J. Fice, and C. C. Renaud, "TeraHertz Photonics for Wireless Communications," *J. Lightw. Technol.*, vol. 33, no.3, pp. 579–587, Feb. 1, 2015.

[2] T. Nagatsuma, S. Horiguchi, Y. Minamikata, Y. Yoshimizu, S. Hisatake, S. Kuwano, N. Yoshimoto, J. Terada, and H. Takahashi, "Terahertz wireless communications based on photonics technologies," *Opt. Exp.*, vol. 21, no. 20, pp. 23736–23747, 2013.

[3] T. Nagatsuma, N. Kukutsu, and Y. Kado, "Photonic Generation of Millimeter and Terahertz Waves and Its Applications," *Applied Electromagnetics and Communications ICECom*, Dubrovnik, 2007, pp. 1-4.

[4] L. Moeller, A. Shen, C. Caillaud, and M. Achouche, "Enhanced THz generation for wireless communications using short optical pulses, " *In Infrared, Millimeter, and Terahertz Waves (IRMMW-THz)*, 2013, pp. 1-3.

[5] K. A. Williams, M. G. Thompson, and I. H. White, "Long-wavelength mononolithic mode-locked diode lasers," *New. J. Phys.*, vol. 6, p. 179, 2004.

[6] G. Carpintero, M. G. Thompson, R. V. Penty, and I. H. White, "Low noise performance of passively mode-locked 10-GHz quantum-dot laser diode," *IEEE Photon. Technol. Lett.*, vol. 21, no. 6, pp. 389–391, March 2009.

[7] A. R. Rae, M. G. Thompson, R. V. Penty, I. H. White, A. R. Kovsh, S. S. Mikhrin, and I. L. Krestnikov, "Harmonic mode-locking of a quantum-dot laser diode," *LEOS 19th Annual Meeting of the IEEE Lasers and Electro-Optics Society.*, Montreal, Oct. 2006, pp. 874-875.

[8] E. A. Avrutin, J. H. Marsh, J. M. Arnold, T. F. Krauss, H. Pottinger, and R. M. De La Rue, "Analysis of harmonic (sub) THz passive mode-locking in monolithic compound cavity Fabry-Perot and ring laser diodes," *IEE Proc.-Optoelectron.*, vol. 146, no. 1, pp. 55–61, Feb. 1999.

[9] J. F. Martins-Filho, E. Avrutin, C. N. Ironside, and J. S. Roberts, "Monolithic multiple colliding pulse mode-locked quantum-well lasers, experiment and theory," *IEEE J. Sel.Top. Quantum Electron.*, vol. 1, no. 2, pp. 539-551, June 1995.

[10] Y. Katagiri, A. Takada, "A Harmonic Colliding-Pulse Mode-Locked Semiconductor Laser for Stable Subterahertz Pulse Generation," *IEEE Photon. Technol. Lett.*, vol. 9, no. 11, pp. 1442–1444, Nov. 1997.

[11] L. Hou, M. Haji, and J. H. Marsh, "240 GHz pedestal-free colliding-pulse mode-locked laser with a wide operation range," *Laser Phys. Lett.* , vol. 11, no. 11, pp. 115804, 2014.

[12] T. Shimizu, X. Wang, and H. Yokoyama, "Asymmetric colliding-pulse mode-locking in InGaAsP semiconductor lasers," *Optical Rev.*, vol. 2, no. 6, pp. 401-403, 1995.

[13] T. Shimizu, I. Ogura, H. Yokoyama, "860GHz rate asymmetric colliding pulse modelocked diode lasers," *Electron. Lett.*, vol. 33, no. 22, pp. 1868–1869, Oct. 1997.

[14] D. Larsson. "Fabrication and characterization of low-noise monolithic mode-locked lasers," Ph. D. thesis, Dept. Photon. Eng., Technical University of Denmark (DTU), Kongens Lyngby, Denmark, 2006. pp. 26.

[15] J. Zhao, E. Kleijn, P. J. Williams, M. K. Smit, and X. J. M. Leijtens, "On-chip laser with multimode interference reflectors realized in a generic integration platform," *Compound Semiconductor Week (CSW/IPRM), and 23rd International Conference on Indium Phosphide and Related Materials*, 2011, pp. 1–4.

[16] K. A. Williams, E. A. J. M. Bente, D. Heiss, Y. Jiao, K. Ławniczuk, X. J. M. Leijtens and M. K. Smit, "InP photonic circuits using generic integration", *Photon. Res.*, vol. 3, no. 5, pp. B60-B68, Oct. 2015.

[17] Y. Barbarin, "1.55 μm Integrated Mode locked Semiconductor Lasers", Ph. D. thesis, Dept. Elect. Eng., Technical University of Eindhoven (TU/e), Eindhoven, the Netherlands, 2007.

[18] I. Aldaya, G. Campuzano, C. Gosset, and G. Castañón. "Phase-insensitive RF envelope detection allows optical heterodyning of MHz-linewidth signals." *IEEE Photon. Technol. Lett.*, vol. 25, no. 22, pp. 2193-2196, 2013.

[19] T. Ishikawa, H. Tanaka, M. Shibata, M. Tajima, Y. Oka, and T. Kaneko, "Narrow Spectral Linewidth Full-Band Wavelength Tunable Lasers for Digital Coherent Communication Systems." *Sei Technical Review*, no. 77, pp. 54-58, 2013.

[20] K. Sala, G. Kenney-Wallace, and G. Hall, "CW autocorrelation measurements of picosecond laser pulses," *IEEE J. Quantum Electron.*, vol. 16, no. 9, pp. 990–996, 1980.

[21] F, Kéfélian, S. O'Donoghue, M. T. Todaro, J. G. McInerney, and G. Huyet, "RF linewidth in monolithic passively mode-locked semiconductor laser." *IEEE Photon. Technol. Lett.*, vol. 20, no. 16, pp. 1405-1407, 2008.

[22] D. von der Linde, "Characterization of the noise in continuously operating mode-locked lasers," *Appl. Phys., A Mater. Sci. Process.*, vol. 39, pp. 201–217, 1986.

[23] K. Yvind, D. Larsson, L. J. Christiansen, J. Mørk, J. M. Hvam, and J. Hanberg, "High-performance 10GHz all-active monolithic modelocked semiconductor lasers," *Electron. Lett.*, vol. 40, no. 12, pp. 735–736, 2004.

Chapter 7

Photonic Enabled Wireless Link using On-chip Mode-Locked Lasers

7.1 Introduction

As we discussed in the introduction, there is a trend for increasing the data rates to 100 Gbps in wireless communication systems to cope with the future needs based in current trends of the demand [1]. A cost effective solution is to increase the carrier wave frequency into the millimeter wave region, moving to the E-band (60 to 90 GHz) and beyond [2]. This work aimed to develop a Photonic Integrated Circuit device to generate the carrier frequencies within these ranges.

The difficulties to generate, amplify and modulate signals at these frequencies have been overcome by combining electronic with photonic techniques. Currently, most of the reported wireless communication links operating above 100 GHz employ photonic generation of the carrier frequency, using mainly two different techniques, either pulsed sources or optical heterodyne sources [3]. In the present work we developed pulsed sources using mode-locked laser diodes (MLLD).

MLLD have already been successfully used in previous photonic enabled wireless link demonstrations operating in the millimeter wave range to generate carrier frequencies at 60 GHz [4] and 120 GHz [5]. While the former employs a self-pulsating MLLD with a repetition rate equal to the desired carrier frequency, the latter uses a MLLD operating at 60 GHz to generate 120 GHz through optical signal processing of the pulsed output using two different approaches. The first approach is to employ optical time domain multiplexing to double the data rate with an optical clock multiplier scheme based on a Mach-Zehnder interferometer. The second is based on two-mode beating, by selecting two modes from the MLLD optical spectrum by an arrayed waveguide grating (AWG). On both approaches, fiber optic components were used to

process the MLLD output. Slight integration efforts demonstrated important noise reduction on the generated millimeter wave signal, highlighting the importance of monolithic integration to improve the signal quality [6].

Within this chapter we will present our results on wireless data transmission with carrier frequencies on the E-band (60 – 90 GHz) and F-band (90 – 140 GHz) generated from on-chip colliding [7] and multiple colliding [8] pulse passive MLLD.

7.2 Experimental Wireless Link Setup

The experimental wireless link setup is composed by the transmitter and receiver modules sketched in Figure 7.1. On the transmitter module, we have three building blocks, the photonic carrier generator, the data modulator and the photonic transmitter. On the receiver module, mainly we have the wireless receiver building block. The bit error rate tester (BERT) provides the pulse pattern generator to the data modulator and receives the data from the receiver module in order to measure the quality and performance of the wireless link system.

The photonic carrier generator was implemented by using either the on-chip colliding pulse passive mode-locked at 70 GHz or the on-chip multiple colliding pulse passive mode-locked lasers at 100 GHz. Then a 99/1 splitter was connected in order to divide the signal in two branches. The 1% branch allowed the optical power measurement all the time by a Newport 842-PE power meter. The other 99% branch is connected to the data modulator.

The data modulator comprises an erbium doped fiber amplifier with a power up to 0 dBm followed by a polarization controller in order to increase the modulation efficiency

and adjusts the polarization in the electro optical amplitude modulator (EOAM). The EOAM is biased at -6 V and driven by an optical modulator driver (OMD). The OMD improves the rise and fall times of the transmitted data provided by a Bit Error Rate Tester Anritsu BERTWave MP2100, using a 1Gbps non-return to zero on-off keying data signal. A pseudorandom bit sequence (PRBS) with a word length of 2^{23}-1 with a maximum output voltage of 2 Vpp is delivered by a pulse pattern generator (PPG) of the BERT tester.

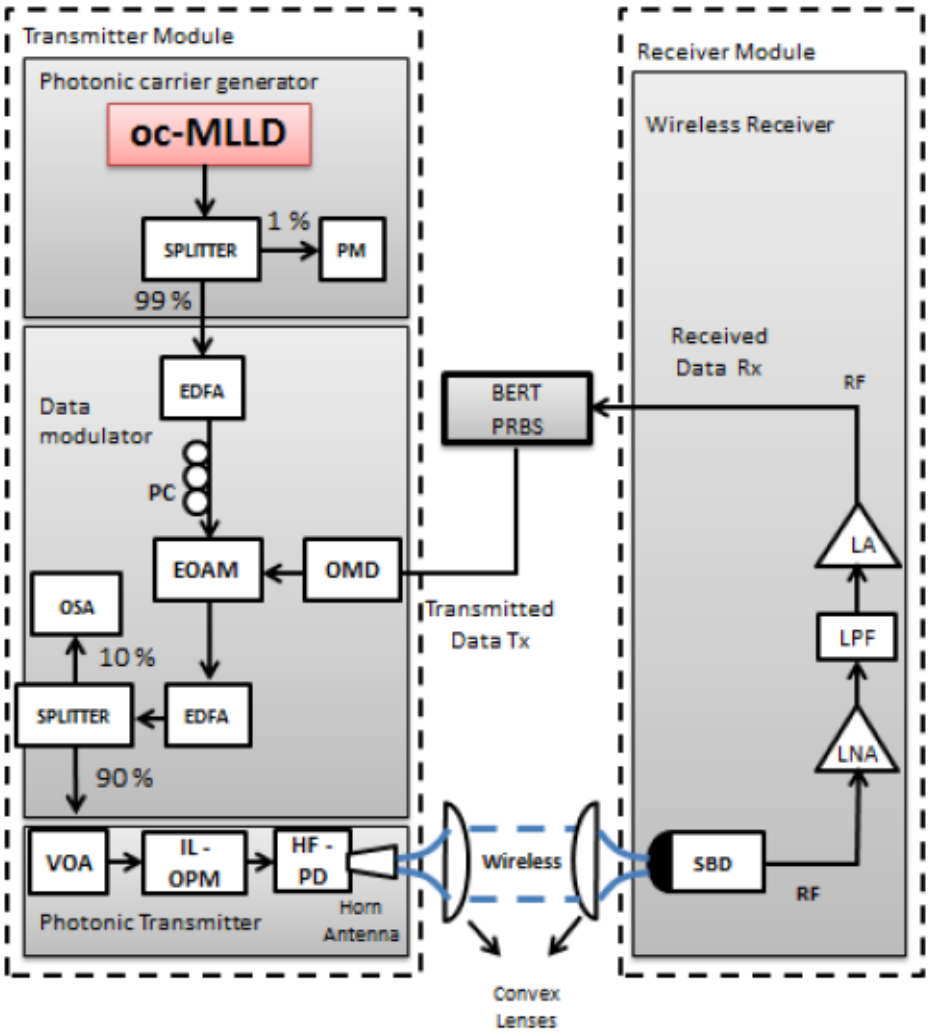

Figure 7.1. Block diagram of the experimental wireless link setup used based on OOK data modulation. EDFA: erbium doped fiber amplifier, PC: polarization controller, RF: radio frequency.

The modulated optical signal is lead to a second optical splitter, with 90/10 splitting ratio. The 10% output allow to measure the optical spectrum all the time in the optical spectrum analyzer. The other 90% is connected to a second EDFA to compensate the modulation losses of EOAM which are around 8 dB. Then a variable optical attenuator (VOA) and an in-line optical power meter (IL-OPM) allow controlling and measuring the optical signal before launching in the photonic transmitter.

In the photonic transmitter the launched optical signal is converted into electrical radio-frequency (RF) signal thanks to the high speed photodiode, and then the electrical radio-frequency signal is radiated to the free space using an antenna. The high speed photodiodes (HF-PD) available on the setup are a U2T XPDV4120 PIN photodiode (PIN-PD) with responsivity 0.62 A/W and the uni-travelling carrier photodiode (UTC-PD) provided by NTT with responsivity 0.4 A/W. Also, the antennas available are a Flann WR15 rectangular horn antenna with 22 dBi gain and WR8 conical horn antenna with 25.5 dBi gain.

The wireless receiver uses a direct envelope detector based on Zero-bias Schottky barrier diode (SBD detector) [9], followed by a chain of amplifiers. The wireless signal received is demodulated and down-converted to a base band data signal by the SBD detector. The responsivity of the antenna-integrated in the SBD detector module with the silicon lens is about 100 V/W and 500 V/W, for a 70 GHz and 100 GHz RF signal, respectively. The chain of amplifiers function is to increase the receiver sensitivity and it is composed by a low-noise amplifier (LNA) with 34 dB gain, is suitable to increase the receiver sensitivity followed by a low-pass filter (LPF) with the intention to smooth and eliminate the damping oscillations of the transient response yielded by the LNA.

Then, a limiting amplifier (LA) ends the chain of amplifiers with the aim of amplify and keep suitable voltage levels at the BERT input plug.

The bandwidth limitation on the wireless data link is determined mainly by the low-noise amplifier bandwidth and the Schottky-Barrier Diode detector in the receiver. The bandwidth of the LNA is and 9 KHz - 3GHz and the baseband signal bandwidth of the SBD detector module including the silicon lens is about 120 GHz (from 40 GHz to 160 GHz), having its peak responsivity (7129 V/W) at 75.7 GHz. Also, the previous characterization of the direct envelop detector allowed us to know the maximum data rate that can be transmitted by the communication system which is 1.5 Gbps [10].

The main improvement is the inclusion of plano-convex lenses ideally suited for THz applications with low insertion loss which allows increasing the distance between the transmitter and receiver modules. The separation distance in the wireless link demonstration is 50 cm. Figure 7.2 depicts the photograph of the experimental wireless link setup.

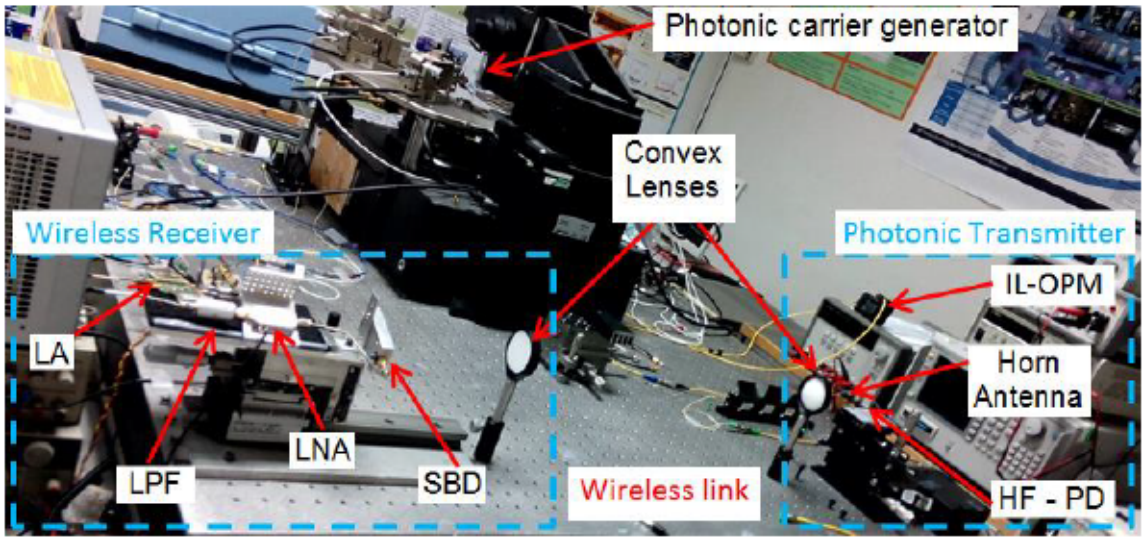

Figure 7.2. Photograph of the experimental wireless link data transmission system.

7.3 Experimental Results of the E-band Wireless Link

The on-chip colliding pulse passive mode-locked laser diode structure operating at 70 GHz (69.76 GHz) has been used as the photonic source in the E-band wireless link. In this case, the photonic transmitter holds the PIN-PD photodiode and the Flann WR15 pyramidal horn antenna.

The measured eye-patterns at bit rate BR= 1 Gbps with a pseudo random bit sequence PRBS = 2^{23}-1 recorded at different photocurrent values into the PIN-PD are depicted in Figure 7.3. The voltage level of the eye pattern is 50 mV/Div and the span 200 ps/Div.

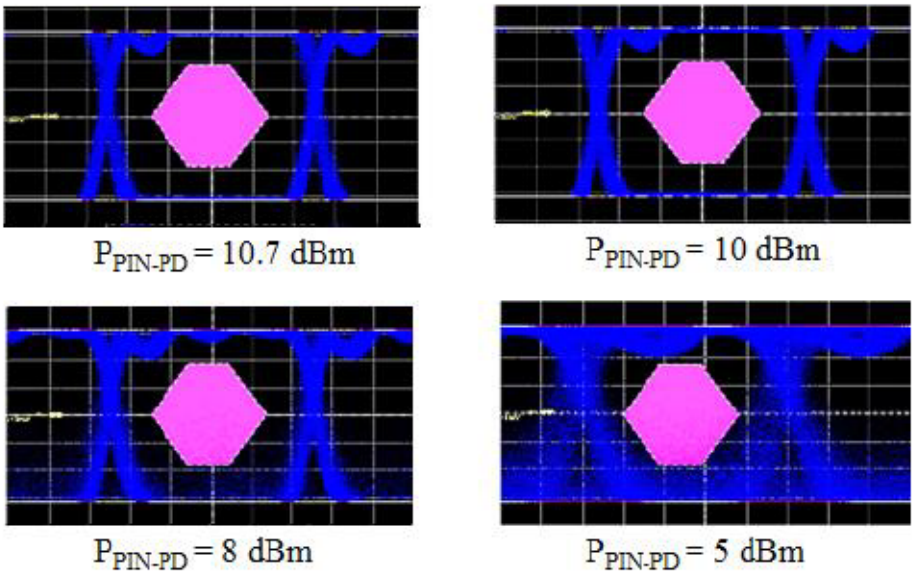

Figure 7.3. Eye-patterns of the received PRBS = 2^23-1 at bit rate BR = 1 Gbps in the E-band wireless link. Voltage level 200 mv/Div and span 200 ps/Div.

The eye-pattern of the received signal is clearly open at the power launched values above $P_{PIN\text{-}PD}$ = 10 dBm (photocurrent, $I_{PIN\text{-}PD}$ = 6 mA) with the time variation at zero crossing below 39 ps. For lower power launched values than $P_{PIN\text{-}PD}$ = 10 dBm, we

appreciate that the eye-patterns start to close and the time variation at zero crossing increases from 39 ps to 126 ps. So the BER is affected and increases drastically.

The bit error rate characteristics at BR = 1 Gbps are also presented. Figure 7.4 shows the measured BER against the optical power launched into the PIN-PD. BER reduces while the optical power launched into the PIN-PD increases. The higher power launched into the photodiode was $P_{PIN\text{-}PD}$ = 10.7 dBm limited by the EDFA and the insertion loss of the attenuator. So, we require increasing the power launched more than $P_{PIN\text{-}PD}$ = 10.7 dBm in order to reduce the BER lower than 10^{-9} and achieve error-free transmission. Finally, considering the BER slope vs. $P_{PIN\text{-}PD}$, we hope to achieve error-free transmission at power more than $P_{PIN\text{-}PD}$ = 14 dBm.

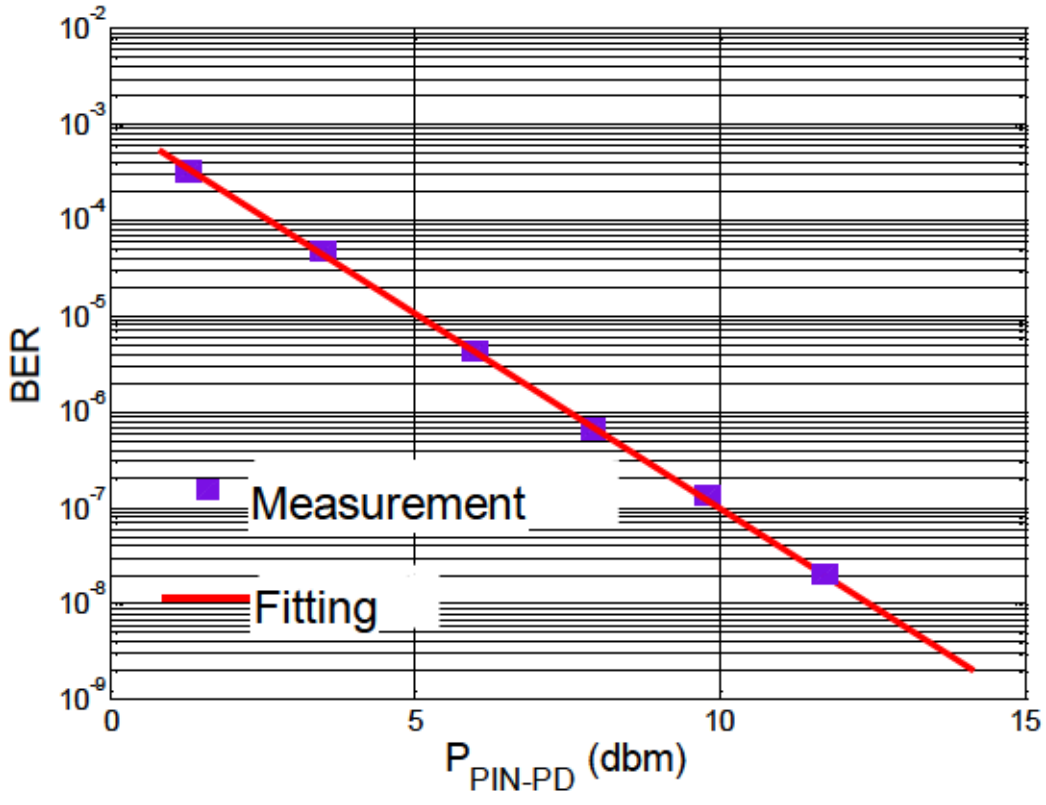

Figure 7.4. Bit error rate against optical power launched into the PIN-PD.

7.4 Experimental Results of the F-band Wireless Link

The F-band wireless link has been successfully demonstrated using the novel on-chip multiple colliding pulse passive mode-locked laser diode structure operating at 100 GHz. In this case, the photonic transmitter comprises the uni-travelling carrier photodiode and WR8 conical horn antenna to meet the frequency range of the F-band wireless link.

The bit rate BR= 1 Gbps with a pseudo random bit sequence PRBS = 2^{23}-1 allows recording the eye-patterns at different power values into the UTC-PD. The obtained eye patterns are shown in Figure 7.5 with voltage level 500 mv/Div and the span 200 ps/Div.

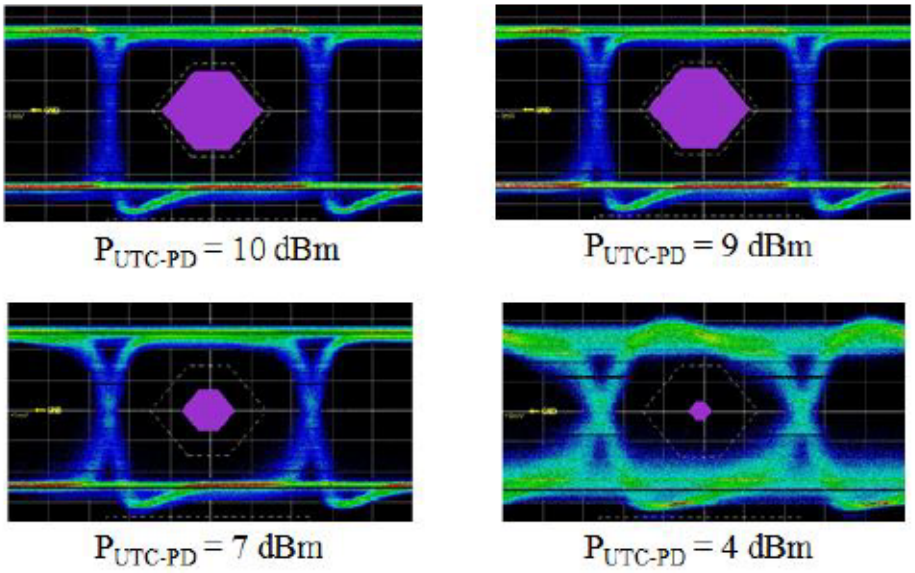

Figure 7.5. Eye-patterns of the received PRBS = 2^23-1 at bit rate BR = 1 Gbps in the F-band wireless link, voltage level 500 mv/Div and the span 200 ps/Div.

The received eye-patterns are clearly open at the power launched values above $P_{UTC-PD} = 7$ dBm (photocurrent, $I_{UTC-PD} = 2$ mA), in which the time variation at zero crossing is below 27 ps. The eye-patterns start to close at lower power launched values than $P_{UTC-PD} = 7$ dBm. The time variation at zero crossing increases from 27 ps to 81 ps and the BER increases severely.

Also, the BER behavior was evaluated versus the optical power launched into the UTC-PD. The bit error rate characteristics at BR = 1 Gbps of the F-band wireless link using the oc-mCPM is sketched in Figure 7.6. The higher power launched into the photodiode was $P_{UTC-PD} = 10.7$ dBm limited by the EDFA and the insertion loss of the attenuator. The BER lower than 10^{-9} was achieved at $I_{UTC-PD} = 2$ mA so the error-free transmission was obtained at the power launched into the UTC-PD $P_{UTC-PD} = 7$ dBm. Besides, at higher power than $P_{UTC-PD} = 7$ dBm we observe the saturation of the UTC-PD due to the fact that those power values are higher than the required power for error-free transmission at 50 cm distance.

Besides, The bit error rate characteristics at BR = 1 Gbps of the F-band wireless transmission link using the heterodyning method is depicted in Figure 7.6. In this case, a photonic integrated arrayed waveguide grating based laser (AWGL) which is capable to provide a carrier frequency at 113 GHz was used. From the comparison of the BER measurements between the pulsed source and heterodyning source, the main improvement of the pulsed source method using oc-mCPM is that lower power than the heterodyning source is required to be launched into the UTC-PD in order to obtain error-free transmission. The pulse source only requires 7 dBm power while the heterodyning source requires around 9 dBm for achieving error-free transmission.

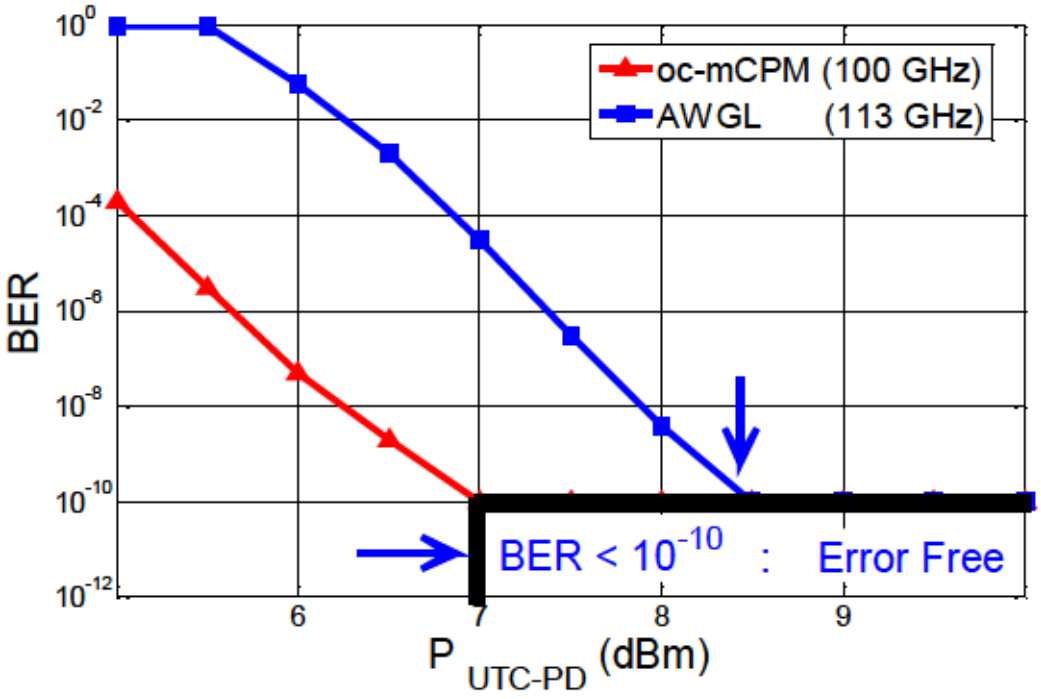

Figure 7.6. Bit error rate against optical power launched into the UTC-PD.

7.5 Conclusions

- We have demonstrated experimentally that the on-chip mode-locked structures developed in the frame of this work meet the pulsed source requirements for wireless link applications with direct envelope detection system.
- We perform the demonstration of a photonic enabled E-band wireless link at bit rate BR = 1 Gbps using a carrier frequency at 70 GHz provided by the on-chip colliding pulse passive mode-locked laser diode structure.
- Error free wireless link communication system at 50 cm separation distance between the transmitter and receiver modules was achieved using the optimized setup which includes plano-convex lenses ideally suited for THz applications with low insertion loss.
- From the comparison of the BER measurements between the pulsed source and heterodyning source, the main improvement of the pulsed source method using oc-mCPM is that lower power than the heterodyning source is required to be launched into the UTC-PD in order to obtain error-free transmission.
- The system contains photonic integrated sources and a zero-bias Schottky barrier diode receiver which provides a great potential to realize compact transmitter and receiver modules.
- By considering long distances in the meter or even kilometer range, additional RF amplifiers would be required as the system performance gets noise limited for such distances.

7.6 References

[1] S. Hisatake, G. Carpintero, Y. Yoshimizu, Y. Minamikata, K. Oogimoto, Y. Yasuda, and T. Nagatsuma, "W-band Coherent Wireless Link Using Injection Locked Laser Diodes,". *IEEE Photon. Technol. Lett.,* vol. 27, no. 14, pp. 1565–1568, July 2015.

[2] A. J. Seeds, H. Shams, M. J. Fice, and C. C. Renaud, "TeraHertz Photonics for Wireless Communications," *J. Lightw. Technol.,* vol. 33, no.3, pp. 579–587, Feb. 1, 2015.

[3] S. Koenig, D. Lopez-Diaz, J. Antes, F. Boes, R. Henneberger, A. Leuther, A. Tessmann, R. Schmogrow, D. Hillerkuss, R. Palmer, T. Zwick, C. Koos, W. Freude, J. Leuthold and I. Kallfass, "Wireless sub-THz communication system with high data rate," *Nature Photon.,* vol. 7, pp. 977–981, Oct. 2013.

[4] T. Nagatsuma, S. Horiguchi, Y. Minamikata, Y. Yoshimizu, S. Hisatake, S. Kuwano, N. Yoshimoto, J. Terada, and H. Takahashi, "Terahertz wireless communications based on photonics technologies," *Opt. Exp.,* vol. 21, no. 20, pp. 23736–23747, 2013.

[5] T. Nagatsuma, N. Kukutsu, and Y. Kado, "Photonic Generation of Millimeter and Terahertz Waves and Its Applications," *Applied Electromagnetics and Communications ICECom*, Dubrovnik, 2007, pp. 1-4.

[6] L. Moeller, A. Shen, C. Caillaud, and M. Achouche, "Enhanced THz generation for wireless communications using short optical pulses, " *In Infrared, Millimeter, and Terahertz Waves (IRMMW-THz)*, 2013, pp. 1-3.

[7] C. Gordón, R. Guzmán, V. Corral, X. Leijtens, and G. Carpintero, "On-Chip Colliding Pulse Mode-locked laser diode (OCCP-MLLD) using multimode interference reflectors," *Opt. Exp.,* vol. 23, no. 11, pp. 14666–14676, 2015.

[8] C. Gordón, R. Guzman, V. Corral, M. Lo, and G. Carpintero, "On-Chip Multiple Colliding Pulse Mode-Locked Semiconductor Laser". *Journal of Lightwave Technology*, 2016.

[9] Javier Montero de Paz, Matthias Hoefle, Ion Oprea, Oleg Cojocari, Luis Enrique García-Muñoz, Daniel Segovia-Vargas, Rolf Jakoby, Guillermo Carpintero. "Compact Schottky Barrier Diode Receiver for E-Band (60 – 90 GHz) Wireless Communications". *IEEE International Topical Meeting on Microwave Photonics (MWP)*, 2012, pp. 244-247.

[10] R. Guzman. "Millimeter-wave and terahertz optical heterodyne photonic integrated circuits for high data rate wireless communications," Ph. D. thesis, Dept. Elec. Tech., University Carlos III of Madrid (UC3M), Madrid, Spain, 2016.

Chapter 8

Final Conclusions and Future Work

8.1 Final Conclusions

We have designed and characterized novel on-chip mode-locked laser structures operating within the millimeter wave range. The on-chip colliding pulse mode-locked laser working at 70 GHz repetition (second harmonic of the fundamental repetition rate) and the on-chip multiple colliding pulse mode-locked laser operating at 100Ghz (fourth harmonic of the fundamental repetition rate). These on-chip mode-locked laser structures have the potential of allowing the integration of subsequent photonic signal processing operations within the chip (modulation, optical filtering, pulse rate multiplication and so on). Also, the merit of these novel structures are the passive mode-locked technique applied which allows avoiding the need of an electronic reference.

The qualitative agreement between the simulation and experimental results of on-chip mode-locked laser structures allow confirming the design criteria of such on-chip structures. The design criteria states that, the length of the saturable absorber related to the total cavity length (L_{SA}/L_{cav}) ranging from 1% to 5 % and the relation between the gain and absorber section lengths (L_{SOA}/L_{SA}) from 10 to 20 times are achieved simultaneously , the laser structure provides stable mode locked regimes with very low jitter.

Taking advantage of the potential of subsequent photonic integration, a boost semiconductor optical amplifier was integrated on-chip at one optical output of the on-chip multiple colliding pulse mode-locked laser operating at 100Ghz with the aim of increasing the amount of the optical power delivered on-chip. Considering a representative link budget calculation for a THz wireless transmission link , the

expected output power of the photonic source needs to reach at least 0 dBm (1 mW). Thanks to the boost SOA included in the oc-mCPM working at 100GHz, it has been demonstrated to exceed this requirement.

The performance parameters of the on-chip mode-locked laser structures are within the limits of the state of the art mode locked laser diodes described in the present thesis. We have obtained on-chip mode-locked laser structures for millimeter wave generation with beating linewidths around 1MHz, timing jitter around 1 ps and optical pulses close to the transform limit. Considering the 1MHz linewidth, we can state that these novel structures are useful for wireless link with direct envelop detection method. But, when using coherent detection method, we have to consider the MHz linewidth limitation, due to the fact that lower linewidths are required for higher order modulation schemes.

The Error free Wireless link demonstration using on-chip mode-locked laser structures reveals that the performance parameters of such structures meets the requirements for broadband wireless link using direct envelop detection method.

8.2 Future Work

Considering the linewidth around MHz of these novel on-chip structures using passive mode-locked technique, we plan for the future to decrease the linewidth of the on-chip mode-locked lasers by using sub-harmonic hybrid structures. This achievement also will allow demonstrate wireless link with any kind of detection method and also increase the actual data bit rate.

Actually we have achieved 100 GHz repetition rate using multiple colliding pulse mode-locked laser and we expect in the future to improve the design by trying asymmetric structures for higher repetition rates.

The main objective for the near future is to take advantage of the potentiality of these photonic integrated structures which is integration of subsequent photonic signal processing operations within the chip (modulation, optical filtering, pulse rate multiplication and so on) in order to obtain a fully integrated photonic transmitter for wireless link communication systems.

Publications Based on this Work

List of Publications

[1] C. Gordón, R. Guzman, V. Corral, M. Lo, and G. Carpintero, "On-Chip Multiple Colliding Pulse Mode-Locked Semiconductor Laser," *Journal of Lightwave Technology*, 2016.

[2] Carlos Gordón, Robinson Guzman, Vinicio Corral, Xaveer Leijtens, and Guillermo Carpintero, "On-chip Colliding Pulse Mode-Locked Laser Diode (OCCP-MLLD) Using Multimode Interference Reflectors," *Optics Express.*, vol. 23, no. 1, pp. 14666-14676, 2015.

[3] Carlos Gordón, Robinson Guzman, Guillermo Carpintero, and Xaveer Leijtens, "On-chip Mode-Locked Laser Diode Structure Using Multimode Interference Reflectors," *Photonics Research.*, vol. 3, no. 1, pp. 15-18, ID223478, 2015.

[4] Carlos Gordón, Robinson Guzmán, Guillermo Carpintero, Vinicio Corral , and Xaveer Leijtens, "On-Chip Photonic Integrated Circuits Structures for Millimeter and Terahertz Wave Signal Generation," *Proceedings of International Topical Meeting on Microwave Photonics (MWP). Paphos, Cyprus – European Union*. October 26th -29th, 2015.

[5] (YOUNG SCIENTIST AWARD) Carlos Gordón, Robinson Guzmán, Guillermo Carpintero, Vinicio Corral , and Xaveer Leijtens, "E-band Wireless Link Using an On-Chip Colliding Pulse Passive Mode-Locked Laser Diode Structure," *Proceedings of URSI 2015- XXX Simposium Nacional de la Unión Científica Internacional de Radio*, September 2nd – 4th, 2015.

[6] (KEYNOTE) Carlos Gordón, Robinson Guzman, Guillermo Carpintero, and Xaveer Leijtens, "Millimeter and Sub-terahertz Wave Colliding Pulse Mode-Locked Laser Diode," *Proceedings of 40th International Conference on Infrared, Millimeter, and Terahertz Waves (IRMMW-THz)*, Hong Kong, China. August 23th -28th, 2015.

[7] Carlos Gordón, Robinson Guzmán, Álvaro Jiménez, Guillermo Carpintero, and Xaveer Leijtens, "Fully Monolithic Colliding Pulse Mode-Locked Laser Diode using Multimode Interference Reflectors," *Proceedings of URSI 2014- XXIX Simposium Nacional de la Unión Científica Internacional de Radio. Escuela Técnica Superior de Ingenieros de Telecomunicación de la UPV de Valencia*, Valencia, Spain. September 3th – 5th, 2014.

[8] Carlos Gordón , Robinson Guzmán, Álvaro Jiménez, Guillermo Carpintero, and Xaveer Leijtens, "Colliding Pulse Mode-Locked Laser Diode using Multimode Interference Reflectors," *Proceedings of 17th ECIO 2014 – European Conference on Integrated Optics and Technical Exhibition, 19th Micro-optics Conference. Université Nice Sophia Antipolis*, Nice, France. June 24th – 27th, 2014.

[9] (INVITED) Guillermo Carpintero, Robinson Guzman, Carlos Gordon, Fréderic Van Djik, Gaël Kervella, and Mourad Chitoui, "Photonic Integrated Circuits for Radio-Frequency Signal Generation," *Journal of Lightwave Technology*, vol. 34, no. 2, pp. 508-515.2016.

[10] Guillermo Carpintero, Robinson Guzman, Carlos Gordon, Xaveer Leijtens, and Katarzyna Ławniczuk, "Photonic-Enabled Millimeter-Wave F-Band Wireless Link Using Photonic Integrated Circuits," *Proceedings of 20th European Conference on Network and Optical Communications (NOC)*. London, United Kingdom. June 30nd – July 2nd, 2015.

[11] Robinson C. Guzman, Guillermo Carpintero, Tadao Nagatsuma, Carlos Gordón, and Mu Chieh Lo, "Photonic Integrated Circuits Based Millimeter-Wave Generation," *Proceedings of International Conference on Transparent Optical Networks (ICTON).,* Trento, Italy. July 10th -14th, 2016.

[12] Mu-Chieh Lo, Robinson Guzmán, Carlos Diego Gordón, and Guillermo Carpintero, "Mode-locked Photonic Integrated Circuits for Millimeter and Terahertz Wave Wireless Communications," *PIERS: Progress In Electromagnetics Research Symposium*., Shanghai-China. August 2016, pp. 1-4.

[13] Robinson Guzman, Guillermo Carpintero, Carlos Gordon, Xaveer Leijtens, and Katarzyna Ławniczuk, "Wireless Link using On-Chip Photonic Integrated Millimeter-Wave Sources," *Proceedings of International Topical Meeting on Microwave Photonics (MWP)*., Paphos, Cyprus – European Union. October 26th - 29th, 2015.

[14] Vinicio Corral, Robinson Guzmán, Carlos Gordón, Guillermo Carpintero, and Xaveer Leijtens, "Optical Frequency Comb Generator based on a Monolithically Integrated Ring Laser," *Proceedings of European Semiconductor Laser Workshop.,* September 24nd – 25th, 2015.

[15] Vinicio Corral, Robinson Guzmán, Carlos Gordón, and Guillermo Carpintero. "Simulación y Caracterización del Laser DBR, Monolíticamente Integrado en un Circuito Fotónico," *Proceedings of URSI 2015- XXX Simposium Nacional de la Unión Científica Internacional de Radio.,* September 2nd – 4th, 2015.

[16] Robinson Guzman, Guillermo Carpintero, Carlos Gordón, Xaveer Leijtens, and Katarzyna Ławniczuk, "F-Band Millimeter-Wave Signal Generation for Wireless Link Data Transmission using On-Chip Photonic Integrated Dual-Wavelength

Sources," *Proceedings of the 38TH Progress In Electromagnetics Research Symposium*., Prague – Czech Republic – European Union. July 6th -9th, 2015, pp. 866-869.

[17] Guillermo Carpintero, Robinson Guzman, Carlos Gordón, Xaveer Leijtens, Fréderic Van Djik, Gaël Kervella, Martyn J. Fice, Katarzyna Balakier, and Cyril C. Renaud, "Comparison of Photonic Integrated Circuits for Millimeter-Wave Signal Generation Between Dual-Wavelength Sources for Optical Heterodyning and Pulsed Mode-Locked Lasers," *Proceedings of the SPIE Optics + Optoelectronics, Physics and Simulation of Optoelectronic Devices XXIII. San Francisco – California – United States*., February 7th -12th , vol. 9357, id. 935719. 2015.

[18] Guillermo Carpintero, Robinson Guzmán, Carlos Gordón, and Xaveer Leijtens, "Photonic Integrated Dual Wavelength Source Using an On-Chip Mode Locked Laser Diode and Arrayed Waveguide Grating Optical Filter," *5th International Symposium on Terahertz Nanoscience (TeraNano V).*, Martinica. December 1st – 5th, 2014.

[19] (Speaker, Carlos Gordón) Guillermo Carpintero, K. Balakier, Z. Yang, Robinson Guzmán, Antonio Corradi, Álvaro Jiménez, Gaël Kervella, Martyn Fice, Marco Lamponi, Mourad Chitoui, Frederic Van Dijk, Cyril Renaud, A. Wonfor, Erwin Bente, R.V. Penty, I.H. White and A. J. Seeds. "Fully Monolithic Photonic Integrated Circuits for Microwave and Millimeter Wave Signal Generation," *Progress In Electromagnetics Research Symposium Proceedings*, Guangzhou, China. August 25th – 28th, 2014, pp. 1711-1714.

[20] L. J. Orbe, C. Gordón, G. Carpintero, G. Maisons, and M. Carras, "InGaAs/InP-based Echelle mirror multiplexer using dual Rowland circle gratings for DFB QCL

arrays in the mid-long infrared range," *In SPIE OPTO, International Society for Optics and Photonics*, pp. 90021O-90021O, February 2014.

Person whom I admire